Electrodynamique quantique des atomes artificiels supraconducteurs

Igor Diniz

UNIVERSITÉ DE GRENOBLE

THÈSE

Pour obtenir le grade de

DOCTEUR DE L'UNIVERSITÉ DE GRENOBLE

Spécialité : **Physique**

Arrêté ministériel : 7 août 2006

Présentée par

Igor Diniz

Thèse dirigée par **Jean-Philippe Poizat**
et codirigée par **Alexia Auffèves**

préparée au sein **de l'Institut Néel, CNRS**
et de **l'École Doctorale de Physique**

Quantum Electrodynamics in Superconducting Artificial Atoms

Thèse soutenue publiquement le **22 Octobre 2012**,
devant le jury composé de :

Mr Olivier BUISSON
DR, Inst. Néel, Président
Mr Jean-Michel RAIMOND
Prof., LKB/ENS, Rapporteur
Mr Klaus MØLMER
Prof., Aarhus Univ. / Niels Bohr Inst., Rapporteur
Mr Patrice BERTET
Research Engineer, CEA/Saclay, Examinateur
Mr Marcelo SANTOS
Prof., UFMG, Examinateur
Ms Alexia AUFFÈVES
CR, Inst. Néel, Directeur de thèse
Mr Jean-Philippe POIZAT
DR, Inst. Néel, Co-Directeur de thèse

Acknowledgements

D'abord je remercie ma directrice de thèse Alexia Auffèves. L'énergie de cette femme courageuse semble pas avoir de fin; elle est la bonne personne à avoir à vos côtés face à un défi. Elle m'a appris beaucoup de choses et je pense que je peux dire que nous avons appris beaucoup de choses ensemble. Je remercie aussi a toute le personel du NPSC : Jean-Philippe, Gilles, Maxime parmi d'autres avec lesquels j'ai beaucoup appris. Au cours de ces 3 années de nombreux collègues de travail ont rendu la vie plus colorée: Aurelien, Claire, Samir, Mathieu, Inah, Emilien, Peter(Petruska?), Pierre-Louis, Daniel, Dudu et Quentin.

I thank the members of my jury for having read and evaluated my work. They have been very kind and our brief discussions meant a lot to me.

Meus amigos de graduação não sairam (nem sairão) da minha memória: Alexandre(Little), Wanessa, Dayanne, Raphael, Daniel Brod, dentre outros; é sempre um prazer reencontrá-los dentro e fora da Física.

Não posso esquecer do Alan ao qual só posso dizer: He tried to kill me but I love him.

A galera de Grenoble é uma segunda família sem a qual não haveria tese! Marcio e Bel, Pierre e Vivi e outros: Grenoble sem vocês é triste. O casal Daniel e Livia então nem se fala, eles ligam o Brasil grenoblois de ponta a ponta passando por Juiz-de-fora! Eles me abrigaram no chateau Valente/Bertges mais de uma vez e foram helps e inoxidáveis em incontáveis momentos. Isso sem falar nas discussões proibidas sobre a origem da vida e a Música brasileira (com M maiúsculo mesmo).

Àqueles quem me deram a vida agradeço por me deixarem quebrar a cara com o que eu inventasse: não existe aprendizado melhor!

Agradeço todo o carinho e amor incondicional que recebi deles e de todos os membros da minha família, e por sempre terem me dado a sensação de que faço parte de um todo. Agradeço em especial à minha tia madrinha Celeste, certamente a pessoa mais gentil e boa que eu conheço, e a minha Vó Lela que se foi cedo demais aos 91 anos. Peitola e Cabeça (e seus dois anjinhos) são sempre uma fonte de alegria imensa são irmãos no sentido mais amplo da palavra.

Para meu amor cito Machado 'A ausência diminui as paixões medíocres e aumenta as grandes, como o vento apaga as velas e atiça as fogueiras'. Esses anos foram difíceis pra nós; 'digam o que quiserem o mal do século é a solidão', mas nos estamos aí. Essa menina é minha Ace; expert em achar coisas perdidas, *chef*, grande cientista e escreve como poucos só para citar as coisas em que sou *nulle* e que ela tentou me iluminar (com sucessos modestos). Que sorte a minha ter te achado nesse espaço-tempo tão imenso.

Abstract

This thesis focus on two problems in circuit quantum electrodynamics. We first investigate theoretically the coupling of a resonator to a continuous distribution of inhomogeneous broadened emitters. Studying this formalism is strongly motivated by recent proposals to use collections of emitters as quantum memories for individual excitations to benefit from the collective enhancement of the interaction strength, while keeping the relaxation properties of a single emitter. We discuss the influence of the emitters inhomogeneous broadening on the existence and on the coherence properties of the polaritonic peaks. We find that their coherence depends crucially on the shape of the distribution and not only on its width. Taking into account the inhomogeneous broadening it is possible to simulate a number of pioneer experimental results on a ensemble of NV centers. The modeling is shown to be a powerful tool to obtain the properties of the spin ensembles coupled to a resonator.

We also propose an original Josephson qubit readout method based on a dc-SQUID with high loop inductance. This system supports a diamond-shape artificial atom where we define logical and ancilla qubits coupled through a cross-Kerr like term. Depending on the qubit state, the ancilla is in the resonant or dispersive regime leading to a large contrast in the transmitted microwave signal amplitude. Simulations show that this original method can be faster and have higher fidelity than currently used methods.

Résumé

Cette thèse porte sur deux problèmes dans l'électrodynamique quantique en circuit. Nous allons d'abord étudier théoriquement le couplage d'un résonateur à une distribution continue d'émetteurs élargie de façon inhomogène. L'étude de ce formalisme est fortement motivé par les récentes propositions d'utiliser des collections d'émetteurs pour les mémoires quantiques. Ces systèmes bénéficient de l'augmentation de la force d'interaction, tout en conservant les propriétés de relaxation d'un seul émetteur. Nous discutons l'influence de l'élargissement inhomogène sur l'existence et les propriétés de cohérence des pics polaritoniques. Nous constatons que leur cohérence dépend essentiellement de la forme de la distribution et pas seulement de sa largeur. En tenant compte de l'élargissement inhomogène on peut simuler avec une grande précision un certain nombre de résultats expérimentaux pionniers sur un ensemble de centres NV. La modélisation se révèle un outil puissant pour obtenir les propriétés des ensembles de spin couplés à un résonateur.

Nous proposons également une méthode originale de lecture de qubits Josephson basée sur un SQUID DC avec une inductance de boucle élevé. Ce système est décrit par un atome artificiel avec des niveaux d'énergie en forme de diamant où nous définissons des qubits logiques et ancilla couplés entre eux par un terme Kerr croisé. En fonction de l'état du qubit logique, lŠancilla est couplé de manière résonante ou dispersive au résonateur, ce qui provoque un contraste important dans l'amplitude du signal micro-onde émis. Les simulations montrent que cette méthode originale peut être plus rapide et peut aussi avoir une plus grande fidélité que les méthodes actuellement utilisées dans le circuit QED.

Contents

Contents v

1 Introduction 1

2 Exploring quantum phenomena with an electrical circuit 7

2.1 Superconducting circuits Hamiltonians 7

2.1.1 Isolated Josephson junction 8

2.1.2 Flux quantization 12

2.2 Qubits in superconducting circuits: artificial atoms 14

2.2.1 Cooper-pair box : Charge qubit 15

2.2.2 RF-SQUID : Flux qubit 18

2.2.3 Current-biased junction: Phase qubit 19

2.2.4 A word on decoherence 20

2.3 Superconducting cavities: coplanar waveguide resonators (CPW) . 21

2.3.1 Tunable coplanar waveguide resonator 23

2.3.2 Cavity-qubit coupling 25

2.3.3 Input-output theory on a transmission line 27

3 Strong coupling ensembles of emitters to a resonator 33

3.1 Modelling transmission 35

3.2 Properties of the transmission function 37

3.3 Origin of peak broadening 40

3.4 Open system approach 44

3.5 Application to quantum memories . . . 47
3.5.1 Quantum memory based on dispersive coupling . . . 47
3.5.2 Quantum memory based on two emitters distributions . . . 48
3.6 Summary . . . 50

4 Hybrid circuits **53**
4.1 General setup and experimental techniques . . . 56
4.1.1 NV centers . . . 56
4.1.2 Transmon qubit readout . . . 60
4.2 Storage and retrieval of a microwave field . . . 61
4.2.1 Transmission Spectroscopy . . . 62
4.2.2 Rabi oscillations . . . 65
4.2.3 Ramsey fringes . . . 68
4.3 Quantum memory implementation . . . 70
4.3.1 Single photon storage . . . 73
4.3.2 Ramsey-fringes . . . 75
4.4 Electron spin resonance spectroscopy . . . 76
4.4.1 Modeling . . . 79
4.4.2 Isotopic impurities in NV centers . . . 81
4.5 Summary . . . 86

5 Proposal for fast readout in a Josephson qubit **87**
5.1 Coupled qubits in the dc-SQUID . . . 88
5.2 QND readout on the dc-SQUID . . . 92
5.2.1 Amplification noise . . . 98
5.2.2 Expected Fidelity . . . 99

6 Conclusion and Perspectives **105**

A Appendix A **107**
A.1 Dynamics . . . 107
A.2 $W(\omega)$ for specific distributions . . . 110
A.3 Development with finite γ . . . 111
A.4 Two ways to obtain the temporal evolution . . . 113

References **115**

Chapter 1

Introduction

Purcell's note in 1946, where he predicted that the spontaneous emission rate of a spin should be considerably enhanced in a resonant structure, was followed by numerous papers dealing with the problem of how the spontaneous emission could be altered by changing the density of the modes surrounding an emitter. The first experiment showing a Purcell factor much larger than unit could only be carried out almost four decades later when Goy *et al* [1] showed a spontaneous emission rate increased with respect to the free-space rate by a factor 500 in sodium Rydberg atoms crossing a Fabry-Perot cavity. Collective Rabi oscillation was observed shortly after in [2], again using Rydberg atoms (see Fig. 1.1). These and other seminal experiments marked the birth of cavity quantum electrodynamics (CQED) initiating a long history of the engineering of the matter-field interaction (see [3] for an historical account). CQED relies on the physics of a spin and an oscillator that interact with each other. Although experiments can be highly sophisticated from the technical point of view, the physics explored can be strikingly simple and fundamental. One of the first ideas was to play with quantum vacuum-fluctuations by surrounding the atoms with a resonant high-Q Fabry-Perot cavity which supports only discrete modes of the electromagnetic field. By adjusting the frequencies and finesse of those resonant modes with respect to the transition frequency of the atoms, one can dramatically alter the coupling of the atoms to their environment. The atom-field coupling can reach such an extreme regime as to produce eigenstates which are a mix of photons and

atomic excitations. The so called strong coupling regime allowed a number of pioneer experiments evidencing atom-field entanglement, and a few examples are the generation of highly non-classical states of the light such as Fock or Schrodinger cat states (see [4] for a review on the subject) and the detection of quantum jumps evidencing directly the presence of an environment [5] or quantum feedback [6, 7]. This progress brought insights into the fundamentals of Quantum Mechanics (QM), allowing for the basic postulates of QM to be tested and understood in a much more direct way by, for instance, measuring a photon without destroying it [8] or exploring the collapse postulate with successive non-demolition measurements [9].

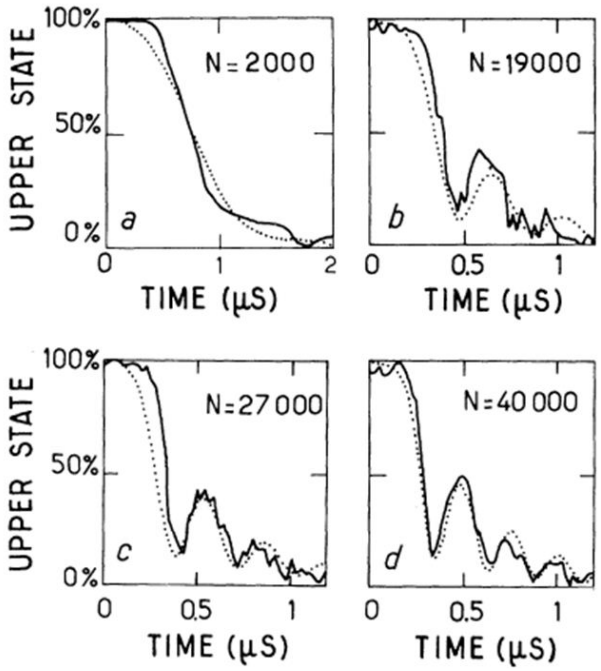

Figure 1.1: A stream of Rydberg atoms, each prepared in its excited state, cross a cavity and are measured after leaving the cavity. The atoms and cavity are in resonance for a controllable time after which they are Stark shifted out of resonance. The plots show the fraction of atoms measured in the excited state as a function of the interaction time, for increasing total atom number N. Experimental data in solid lines, theoretical calculation in dotted lines. Reproduced from [2].

Control over the coherent dynamics of quantum systems has become a fasci-

nating prospect of modern physics. One practical goal for the control of quantum systems is the processing of quantum information [10]. Quantum computers enable large improvements in computational power and communication security by exploiting the superposition principle and non-classical correlations of quantum mechanics. Although the collection of quantum algorithms is still rather limited, it includes strong examples like the factoring of large integers by Shor's [11] and Grover's algorithm for accelerating search on a unsorted database [12]. On the communication side, quantum cryptography and quantum key distribution for secure communication are now well established [13, 14]. Increasing effort is being devoted towards physically realizing quantum computers, and there are many proposals for implementing the necessary quantum devices. Superconducting qubit architectures emerge in this context because they benefit from the use of conventional microfabrication techniques, which allows straightforward scaling to a large numbers of qubits and the freedom to fabricate a variety of qubit types and interactions. On the other hand, scaling in architectures based only on microscopic degrees of freedom is a non-trivial task.

Different ideas to process quantum information also exist, from the standard circuit model [15], which bears analogy with the classical circuit model, to measurement-based quantum computation [16, 17]. A complete implementation of a quantum computer requires the means for state preparation, the ability to apply entangling quantum gates and a readout method; these and other requirements are compiled in the DiVincenzo criteria [18]. Linear circuit elements such as capacitors and inductors can form low-dissipation superconducting resonators, but are hard to use for quantum computation without additional resources because the energy-level spacings are degenerate. The nonlinearity of the Josephson inductance breaks the degeneracy of the energy level spacings, allowing the implementation of quantum gates, state preparation and readout using only classical microwave pulses. The Josephson junction is a remarkable nonlinear element because it combines negligible dissipation with extremely large nonlinearity: in fact, a single microwave photon has a large effect in the junction inductance.

Borrowing ideas from atomic cavity quantum electrodynamics (cQED), one can try to engineer the electromagnetic field in the surroundings of a Josephson qubit not only to obtain new means to manipulate the qubit but also to protect

it from environment noise that leads to decoherence [19]. In cQED, superconducting qubits are used as artificial atoms along with superconducting microwave resonators to explore this physics. In recent years many theoretical proposals for coupling superconducting qubits to resonators appeared accompanied by a fast growing number of experiments, some of each we will discuss in Chapter 2. The advantage of such resonators is that they are quasi-one-dimensional Fabry-Pérot cavities with mode volume orders of magnitude smaller than what can be achieved with ordinary three-dimensional resonators. Because the mode volume $\mathcal{V}$ of these quasi-one-dimensional resonators can be as small as 10^{-6} cubic wavelengths and the coupling constant scales like $\mathcal{V}^{-1/2}$ [3], the coupling strength g between the atom and a single photon in the resonator is greatly enhanced. Besides, artificial atoms have transition dipoles larger than even Rydberg atoms, which means that g becomes orders of magnitude larger than usual [19]. It took roughly a decade from the first experiments demonstrating strong coupling with single atoms until similar results were achieved in superconducting circuits. In 2004, two separate research groups [20, 21] exploited charge and flux qubits, coupled to a transmission-line resonator and a SQUID LC oscillator respectively, to achieve this regime. It did not take long until the control over the qubit was used to control the photonic state exploiting their interaction. In 2008, the authors of [22, 23] synthesized with high quality arbitrary photonic states (with less than 10 photons) (see Fig. 1.2). It is remarkable how superconducting qubits can now explore the fundamental physics of the interacting spin and oscillator even if they are not microscopical systems. With this system one can revisit the quantum optical protocols that were explored with atoms and pave the way to quantum information on a chip.

The counterpart of being macroscopical is that such circuits usually couple with the environment and the coherence times are typically small (even if they improved at a fast rate in the last decade). By coupling the circuits with microscopical degrees of freedom one could use them as bearers of quantum information to alleviate the short coherence of the Josephson qubits, and form a hybrid circuit which we discuss in Chapter 4. The work presented in this manuscript belongs to the framework of quantum optics in cQED, so we use Chapter 2 to bridge the gap between CQED and cQED, introducing the physics behind the Josephson qubits.

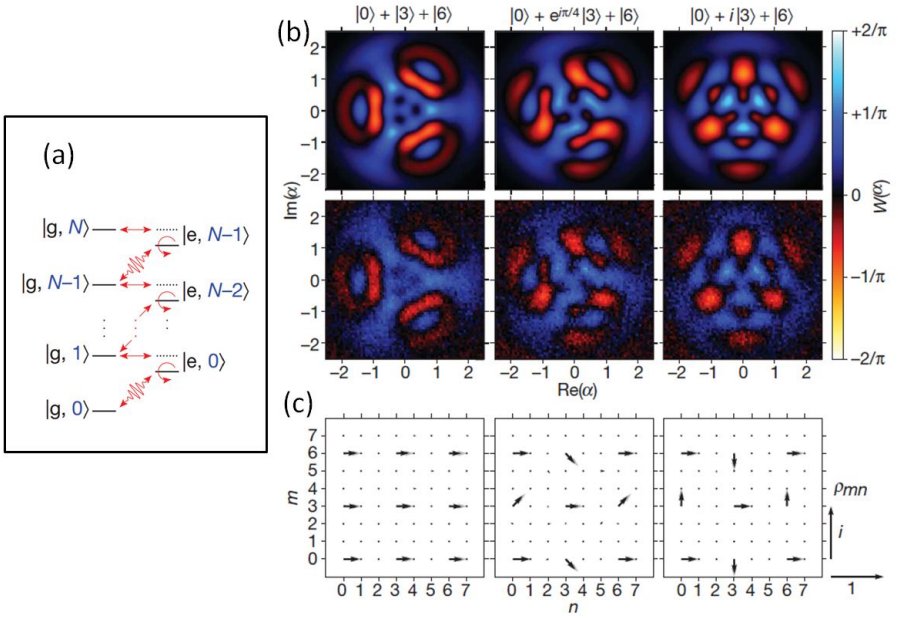

Figure 1.2: (a) The $n-th$ Fock state is produced by repeating n times a sequence where the qubit is prepared in the excited state by a classical pulse while being kept off-resonance and then its resonance is adjusted to match the resonator's and the excitation is transferred resonantly. A slightly more sophisticated sequence where the qubit population and phase is manipulated before it interacts resonantly with the cavity is used to generate an arbitrary state on the resonator. (b) Theoretical form of the Wigner function as a function of the complex resonator amplitude in photon number units (top row). Measured Wigner function. Negative quasi probabilities are clearly measured (bottom row). (c) Calculated (grey) and measured (black) values for the resonator density matrix, projected onto the number states. The magnitude and phase are represented by the length and direction of an arrow in the complex plane. The fidelities between target states and the measured density matrices are 90%. Adapted from [23].

In Chapter 3 we address one difficulty that emerges when one tries to couple a solid-state spin ensemble to a circuit by studying a model that takes into account inhomogeneous broadening. The results on this Chapter have been used to model experiments performed by the Quantronics group of CEA Saclay, one of the first to achieve strong coupling between a superconducting resonator and a Nitrogen-Vacancy spin ensemble in a diamond matrix. In Chapter 4 the simulation of this system is explored in a variety of experimental sequences. Besides coherence times, there is also room for improvement in the readout performance of Josephson qubits. That is precisely our goal in Chapter 5, where we explore a new qubit readout scheme based on a high-inductance dc-SQUID that can potentially reach high fidelity at very short integration time.

Chapter 2

Exploring quantum phenomena with an electrical circuit

In this chapter we develop the basic theory of superconducting (artificial) atoms and their coupling with resonators. The artificial atoms are based on the dissipationless non-linearity provided by the Josephson junction. A basis for the quantum description of the Josephson circuits is the Hamilton formalism. The dynamical equations are the quantum analogs to the standard Kirchhoff rules. A phenomenological approach taking into account the basic properties of superconductors is discussed in Section 2.1 allowing us to to obtain the Hamiltonian of a given circuit. An analog to the atomic Fabry-Perot cavities in described in 2.3 as well as the analog to the cavity-atom coupling. We end up presenting input-output theory, a tool that will be used throughout this thesis in 2.3.3.

2.1 Superconducting circuits Hamiltonians

Standard superconducting circuits used for the qubit applications are combinations of the three basic elements: capacitive elements, linear inductive elements of superconducting leads and nonlinear inductances of Josephson tunnel junctions. Before going into the full circuits we shall explore simpler circuits to introduce the building blocks for constructing the circuit Hamiltonian, i.e. the kinetic energy associated with the charging energy of the capacitive elements, the potential

energy associated with the Josephson inductance and the inductance of the superconducting loops.

In an ordinary superconductor, the main physical effect is that the effective interaction between electrons, resulting from virtual phonon-exchange, leads to pairing of electrons of opposite spin into so-called Cooper pairs [24]. These pairs are the carriers of the charge in the superconductor. Due to the anti-parallel combination of the spins in each pair, these particles are bosons that can form condensate at low temperatures. To create an excitation from the ground state one has to break a pair to created single electrons, thus the energy gap Δ between the two first levels corresponds to the binding energy of a Cooper pair. The scale of this gap is typically several Kelvin. We will consider the limit of low temperature attained in typical experiments where $k_B T \ll \Delta$. As long as this condition is fulfilled an isolated superconductor has effectively no degrees of freedom. When two relatively bulky superconducting electrodes are weakly coupled to one another, i.e. separate by a thin oxide layer, they form a Josephson junction. For the junction description we will adopt a phenomenological approach due to Girvin [25]. The idea is to lean on the BCS theory of superconductivity and the fact that the carriers of charges are Cooper pairs and to describe the coherent tunneling of these pairs.

2.1.1 Isolated Josephson junction

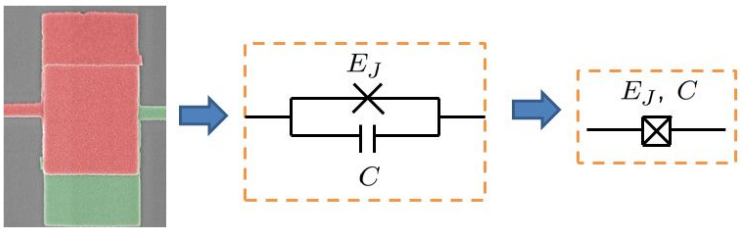

Figure 2.1: On the left MBE image of a Josephson junction formed by the deposition of two layers of aluminium separated by an oxide layer insulating the superconducting electrodes (Courtesy of Olivier Buisson). Symbol on the right encloses the junction capacitance.

As soon as we couple the first electrode to a second one with a tunnel junction (see Fig. 2.1), Cooper pairs can tunnel through the barrier and the state of the whole junction can be specified by the net number of pairs that went from the left to the right electrode. So if m pairs have tunneled we say the system is in the state $|m\rangle$. Neglecting the capacitance of the junction, we get that all the low-energy $|m\rangle$ states are degenerate in energy. To account for the tunneling of pairs we consider a phenomenological Hamiltonian:

$$H_J = -\frac{E_J}{2}\sum_m (|m\rangle\langle m+1| + h.c.)\,, \tag{2.1}$$

where the parameter E_J, which measures the tunneling strength, is called the Josephson coupling energy.

To include the Coulomb charging energy to transfer Cooper pairs we have neglected so far, we recall the simple result from electrostatics that says that the energy stored in a capacitor of capacitance C and charge Q is $E = Q^2/2C$. It is convenient to define as a basic unit the Coulomb charging energy $E_C = (2e)^2/2C$, associated with the transfer of a single Cooper pair. Defining $\hat{N}$ as the number operator of pairs transferred across the junction

$$\hat{N} = \sum_m m\,|m\rangle\langle m|\,, \tag{2.2}$$

we can write the Coulomb charging energy $H_C = E_C\hat{N}^2$ to form the total Hamiltonian of a Josephson junction (see Fig. 2.1)

$$H = -\frac{E_J}{2}\sum_m (|m\rangle\langle m+1| + h.c.) + E_C\hat{N}^2\,. \tag{2.3}$$

The Coulomb part of the Hamiltonian is commonly written $H_C = E_C(N - n_g)^2$, where n_g is called the 'gate charge' or 'offset charge' and represents the effect of external electric field or some asymmetry in the junction. For the moment we set $n_g = 0$. Borrowing from the tight-binding model we define the plane-wave like

states

$$|\phi\rangle = \sum_m e^{im\phi} |m\rangle \ , \tag{2.4}$$

labeled by the angle $\phi \epsilon [-\pi, \pi]$. We see readily that

$$H_J |\phi\rangle = -E_J \cos(\phi) |\phi\rangle \ , \tag{2.5}$$

i.e H_J is diagonal in the $\{|\phi\rangle\}$ basis. As the Cooper pairs have charge $2e$, there is a current associated with the pairs motion. The operator for the current flowing through the electrodes is simply $\hat{I} = 2e\frac{d\hat{N}}{dt}$. Heisenberg equation of motion writes

$$\begin{aligned} \hat{I} &= 2e\frac{i}{\hbar}[H, \hat{N}] \\ &= -\frac{ieE_J}{\hbar}\sum_m (|m\rangle \langle m+1| - |m+1\rangle \langle m|) \, . \end{aligned} \tag{2.6}$$

So then the current operator is also diagonal in the $\{|\phi\rangle\}$ basis:

$$\hat{I} |\phi\rangle = \frac{2eE_j}{\hbar} \sin(\phi) |\phi\rangle \ , \tag{2.7}$$

We can identify this equation with the first Josephson relation [26, 27]. The critical current I_c is defined as $I_c = \frac{2eE_j}{\hbar}$. We can use this identification to interpret the states $|\phi\rangle$ as the states of persistent current. The first Josephson relation states that when a junction is crossed by a persistent current $I_C \sin(\theta)$ the phase across the junction is precisely θ. Thus we can interpret the angle ϕ defined in Eq. (2.4) as the phase change across the junction. This interpretation will be particularly important in the light of the Meissner effect discussed in the next Section. Now we can rewrite the Hamiltonian in a more conventional way:

$$H = -E_J cos(\phi) + 4E_C \hat{N}^2 \, , \tag{2.8}$$

where $cos(\phi)$ is short for $\sum |\phi\rangle \langle\phi| cos(\phi)$. With Eq. (2.4) and Eq. (2.2), in the $\{|\phi\rangle\}$ representation we see that the operators $\hat{\phi} = \sum_\phi \phi |\phi\rangle \langle\phi|$ and N are

reminiscent of canonically conjugated operators. Indeed

$$\begin{aligned}\langle m|\,[N,\hat{\phi}]\,|\phi\rangle =& \phi\,\langle m|\,N\,|\phi\rangle + i\frac{\partial}{\partial\phi}\,\langle m|\,\hat{\phi}\,|\phi\rangle \\ =& i\left(\frac{\partial}{\partial\phi}\phi - \phi\frac{\partial}{\partial\phi}\right)\langle m|\phi\rangle \\ =& i\,\langle m|\phi\rangle\ ,\end{aligned} \tag{2.9}$$

is valid for any $|m\rangle$ and $|\phi\rangle$, thus one finds $[N,\hat{\phi}] = i$. As $\{|\phi\rangle\}$ is compact, the structure formed by N and $\hat{\phi}$ is completely analogous to the angular momentum and the angle of a body that rotates around a fixed axis. In this analogy the Hamiltonian Eq. (2.3) corresponds to placing the rotor in a gravitational field with strength proportional to E_J. The sinusoidal potential is clearly non-linear and will be the heart of any superconducting qubit.

This allow to obtain the second Josephson relation [27] lets consider the situation where an external electric field is applied and maintained in such a way that there is a fixed voltage drop V across the tunnel junction. This additional potential corresponds to a term in the Hamiltonian $-(2e)VN$. It can be incorporated in the Coulomb charge term as $E_C(\hat{N} - n_V)$, generating the offset $n_V = V/E_c$. The second Josephson relation can be obtained using the commutation relation we have just obtained, with Heisenberg's equation we get

$$\hbar\dot{\phi} = i[H,\phi] = 2eV\,. \tag{2.10}$$

By solving the dynamics of the current operator I for a DC voltage bias V we see that an AC current appears:

$$\left\langle \hat{I}(t)\right\rangle = I_c sin(\phi_0 + \frac{2eV}{\hbar}t)\,. \tag{2.11}$$

The Josephson junction finds than a direct technological application, we can use it to maintain a voltage standard with a frequency measurement (since frequency is a physical quantity that can be measured with very high accuracy).

2.1.2 Flux quantization

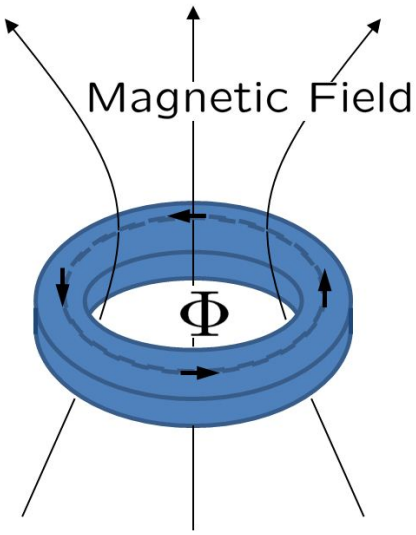

Figure 2.2: A superconducting loop is pierced by a magnetic Flux Φ. A particle with charge $2e$ traveling by the indicated by a dashed line would acquire a phase term $\exp(i2e\Phi/\hbar)$

Although the simple model described in the last Section was enough to describe some important properties of a Josephson junction we are still lacking an important ingredient that appears in superconducting circuits. The flux quantization is related to the Meissner effect [28], where any magnetic field present inside a sample will be actively excluded when this material enters a superconducting phase.Non-zero magnetic flux may be obtained in a ring of superconducting material, as there are no supercurrents present at the center of the ring the magnetic fields can pass through. However, the supercurrents at the boundary will arrange themselves so that the total magnetic flux through the ring is quantized in units of $\Phi_0 = 2\pi\hbar/2e$ [29]. Flux quantization occurs because when a charged particle travels in a field-free region that surrounds a region in which there is a magnetic flux. In this situation, upon completing a closed loop the particleŠs wave function will acquire an additional phase factor. The wave function must be single valued at any point in space. This can only be accomplished if the magnetic flux is quantized. But when there are other elements in the loop the total phase that

the particle's wave function will acquire is the sum of the phase related to the trapped magnetic flux and the phase it gets when crossing each element. If ϕ_i is the phase associated with crossing element i on the loop and the external field flux applied is Φ_e and $\phi_e = (2e/\hbar)\Phi_e$ is the associated phase, the flux quantization equation imposes the constraint $\sum_i \phi_i + \phi_e = 2\pi n$ (for integer n). This is the last phenomenological input we need to describe our circuits.

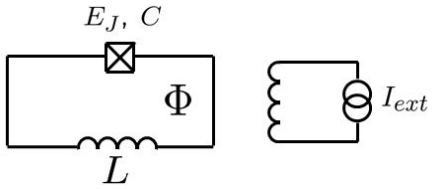

Figure 2.3: Electrical circuit for the RF SQUID. Current I_{ext} flows in the the loop on the right generating a magnetic flux on the SQUID.

As an example to this rule we can consider the inductively-shunted junction, also known as the RF SQUID (Superconducting Quantum Interference Device), of Fig. 2.3. The energy stored in an inductor of inductance L is usually written $H_L = LI^2/2$. It can also be written as a function of the magnetic flux through the inductor $\Phi_L = LI$, yielding $H_L = \Phi_L^2/2L$. The flux quantization translates into the constraint $(2e/\hbar)\Phi_L = 2\pi n - (\phi - \phi_e)$ (the signals are just a typical convention). The factor $2\pi n$ can be absorbed by the phase ϕ as this leaves the sinusoidal part of the Hamiltonian changed, this gives the conventional Hamiltonian of the inductively-shunted junction

$$H = E_C\hat{N}^2 - E_J cos(\phi) + \frac{E_L}{2}(\phi - \phi_e)^2\,, \tag{2.12}$$

where $E_L = (\hbar/2e)^2/L$. The change in the Hamiltonian is accompanied by a change in the domain of the *phase* which now takes values in the line instead of the circle. This happens because as charge can move onto the junction plates continuously through the inductor so the charge variable is no longer integer-valued but rather continuous, as expected from the fact that the Hamiltonian is no longer periodic and periodic boundary conditions are no longer satisfied. The ability to control the three parameters E_J,E_C and E_L allows the fabrication of a

rich variety of level structures in the inductance-shunted family of qubits. One such qubit is the current-biased junction, the simplest phase qubit, depicted in Fig. 2.4.

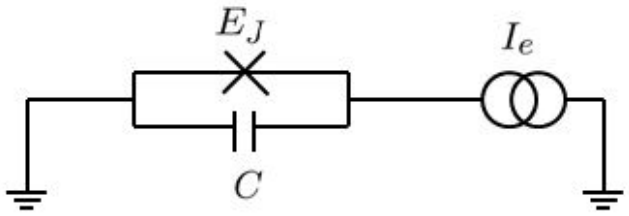

Figure 2.4: Electrical circuit current-biased Josephson junction.

If a constant current is forced through the junction an its capacitance, the current bias source can be understood as arising from a loop inductance with $L \to \infty$ biased by a flux $\Phi \to \infty$ such that $I_e = \Phi/L$. Thus the Hamiltonian is readily obtained from Eq. (2.12) as

$$H = E_C \hat{N}^2 - E_J cos(\phi) - \frac{\hbar}{2e} I_e \phi \,. \tag{2.13}$$

The potential in the ϕ representation is shown in Fig. 2.8. It has the shape of a tilted washboard, with the tilt given by the ratio I_e/I_C.

Now we have all the tools to describe a superconducting circuit. Here we have taken a more direct approach trying to interpret the Hamiltonians rather than focusing on the rules to write them. A more systematical approach in which 'quantum Kirchoff's ' laws are used to impose relations among branch variables leading to the Hamiltonian is available, such techniques can be found in [30, 31].

2.2 Qubits in superconducting circuits: artificial atoms

We devote this Section to explore the Josephson non-linearity in three basic superconducting circuits that form simple qubits. An important problem in realizing a Josephson qubit is to suppress as much as possible the detrimental effect of the

fluctuations that will lead to decoherence. The three basic circuits offer strategies to both retain the non-linearity necessary to generate a qubit and alleviate the decoherence. These qubits are called charge, flux and phase qubits. A word of caution is needed to avoid confusion arising from these historical names. One should not think, for instance, that in charge qubits, quantum information is encoded in charge. Both the charge and phase are quantum variables and they are both uncertain for a generic eigenstate of a charge qubit. The term 'charge qubit' should be understood as referring to the control parameter, i.e. the qubit variable that we use to manipulate the qubit, applying gates and reading the qubit state for example.

2.2.1 Cooper-pair box : Charge qubit

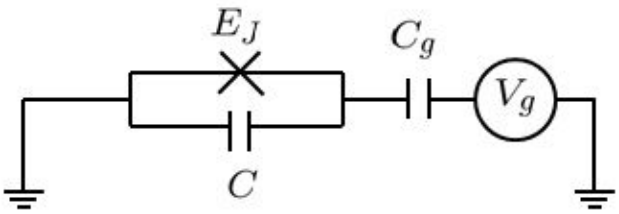

Figure 2.5: Electrical circuit equivalent for the Cooper-pair box.

In this circuit, first demonstrated in 1998 [32, 33], a Josephson junction is biased by a voltage source through a gate capacitance (see Fig. 2.6). Using the results of the two previous Sections we can easily show that the Hamiltonian

$$H = E_C(\hat{N} - n_g)^2 - E_J cos(\phi)\,, \tag{2.14}$$

describes the CPB if $E_C = (2e)^2/(2C_J + 2C_g)$ and $n_g = C_g V_g/2e$. Note that it has the same form of an isolated junction. The presence of stray fields will lead to perturbation in n_g, this design however can be operated in a point where this noise has no first order effect on the energy levels of the qubit. The qubit is composed of two states which are generally a mixture of many charge states, in particular the qubit is formed only by two charge states $|m = 0, 1\rangle$ in the limit

$E_C \gg E_J$. Let us limit ourselves to the two lowest levels of the CPB. Near the degeneracy point $n_g = 1/2$, we get the reduced Hamiltonian

$$H_{qubit} = \Omega_z \sigma_Z + \Omega_x \sigma_X \,, \tag{2.15}$$

where $\sigma_{X,Y,Z}$ are the Pauli matrices. The first charge qubits experimentally realized were in the regime $E_C \simeq E_J$ [34]. The energy levels in this regime, calculated numerically, are shown in Fig. 2.6. We see a 'sweet spot' obtained when $n_g = 1/2$, i.e. at this point the qubit transition frequency is to first order insensitive to the offset charge noise.

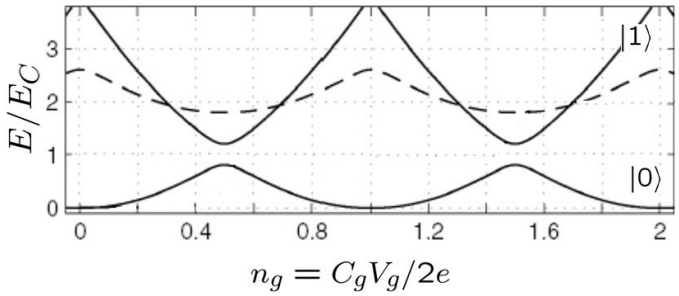

Figure 2.6: Solid lines are the energies of ground and first excited levels of the Cooper-pair box as a charge qubit. Note the 'sweet spot' at $n_g = 1/2$. In this plot $E_J/E_C = 0.4$. Adapted from [35]

There are many successful circuits based on the CPB. One successful strategy to protect the qubit from stray electric field noise is to operate the CPB in the so called 'transmon' regime [36] . In the 'transmon' regime the Josephson tunneling energy dominates over the Coulomb charging energy and the phase described by Eq. (2.14) is restricted to small deviations around the lowest level. This allows us to approximate the Hamiltonian by expanding the cosine to forth order:

$$H \approx E_J \left(\frac{1}{2}\phi^2 - \frac{1}{24}\phi^4 \right) + E_C N^2 \,, \tag{2.16}$$

up to an irrelevant constant in the energy. For small oscillations it resembles an anharmonic oscillator. However, ϕ is compact here and obeys periodic boundary conditions at $\phi = \pm\pi$, in this sense a more complete analogy can be made with

the quantum rotor. As usual in this cases, creation-annihilation operators provide a convenient way to obtain the energy levels. We define the annihilation operator as

$$a = \frac{1}{\sqrt{2}} \frac{(\sqrt{E_J}\hat{\phi} + i\sqrt{E_C}N)}{(E_C E_J/2)^{\frac{1}{4}}}\,, \tag{2.17}$$

which can be inverted to give $\hat{\phi} = \phi_{ZPF}(a + a^\dagger) = \left(\frac{E_C}{2E_J}\right)^{\frac{1}{4}}(a + a^\dagger)$. To second order in ϕ we have an harmonic oscillator of natural frequency $\Omega_J = \sqrt{2E_C E_J}/\hbar$, known as the Josephson plasma frequency. The forth order term is responsible for the anharmonicity as we can readily see using the creation-annihilation operators:

$$V = -\frac{E_J}{24}\phi^4 \approx -\frac{E_C}{16}[2a^\dagger a + (a^\dagger)^2 a^2]\,. \tag{2.18}$$

The first term simply decreases slightly the plasma frequency. The second is the one that makes the oscillator anharmonic, i.e. the frequency ω_{12} is smaller than ω_{01} and the difference is precisely $A \equiv E_C$. Note that in the limit $E_J \gg E_C$ the corrections are small and the expansion is self-consistent. Although some anharmonicity is essential to obtain a qubit we do not need it to be extremely large, in fact the anharmonicity just has to be large compared to the width of the pulses used on the qubit manipulation. Finally, pushing E_C/E_J to less than 1 can lead to an important protection against decoherence. The offset n_g can be removed from the Hamiltonian with the unitary transformation $U = e^{-in_g\phi}$ but this transformation changes the boundary conditions so that they are no longer periodic. Nevertheless the low-lying levels have a negligible probability amplitude in the boundary region and this amplitude decays exponentially with the ratio E_J/E_C. This is simply a consequence of the fact that the zero-point-fluctuation in the phase gets smaller as we increase E_J/E_C and thus the system is barely affected by the changes in the boundary. In fact it can be show [37] that the energy shifts due to external field is approximately proportional to $\exp(-\sqrt{2E_J/EC})$.

2.2.2 RF-SQUID : Flux qubit

The flux qubit is the magnetic analogue of the electrostatic CPB. In this design a current driven magnetic field pierces the box with a strength given by a mutual inductance M.

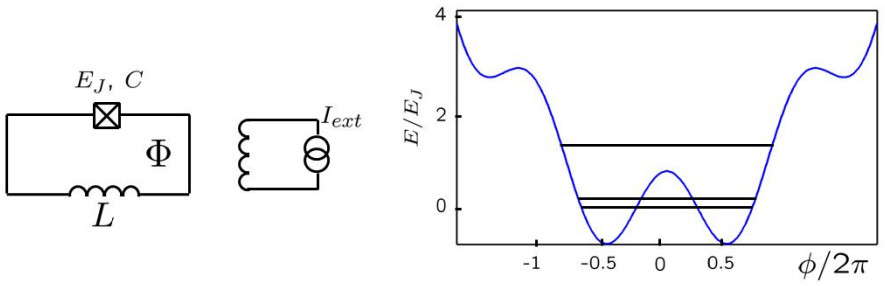

Figure 2.7: Circuit and potential of the flux qubit. We took $\phi_e = \pi$. Levels are only illustrative.

An elementary flux qubit can be constructed with an rf SQUID operating in the phase regime, $EJ \gg EC$. Let us consider the Hamiltonian 2.12 at $\phi_e = \pi$, i.e. at half-integer bias magnetic flux. The potential depicted in Fig. 2.7 has two identical wells with equal energy levels when the tunneling between the wells is neglected. These levels correspond to clockwise and counterclockwise persistent currents circulating in the loop and are connected via tunneling. At $\Phi_e = \Phi_0/2\pi$, the two lowest energy levels are then the symmetric and antisymmetric combinations of the two wavefunctions localized in each well, and the energy splitting between the two states can be seen as the tunnel splitting associated with the quantum tunneling through the potential barrier between the two wells. If the tunneling barrier is much smaller than the Josephson energy, the potential 2.12 can be approximated as

$$\begin{aligned} H &\approx -E_J cos(\phi) + \frac{E_L}{2}(\phi - \phi_e)^2 \\ &\approx E_L \left(-\varepsilon \frac{\delta^2}{2} - (\phi_e - \pi)\delta + \frac{1+\varepsilon}{24}\phi^4 \right) , \end{aligned} \tag{2.19}$$

where $\delta = \phi - \pi$ and $\varepsilon = E_J/E_L - 1 \ll 1$ determines the height of the barrier. The qubit Hamiltonian derived by projecting the Hamiltonian above in the subspace

of the first two levels can only be obtained numerically. Nevertheless we can expect that going from the case of a high barrier in the middle where there are eigenstates localized on each well, if we start to decrease the barrier the tunneling will hybridize the levels and the energy levels will repel each other lifting the degeneracy. We end up with a qubit of the same form of the CPB Eq. (2.15) where Ω_z depend exponentially on the height of the barrier ε (and that can be controlled externally) and a Ω_x that goes through a sweet spot of first order insensitivity at half magnetic flux quantum $\phi_e = \pi$ (in analogy to the half quantized charge we found for the CPB).

2.2.3 Current-biased junction: Phase qubit

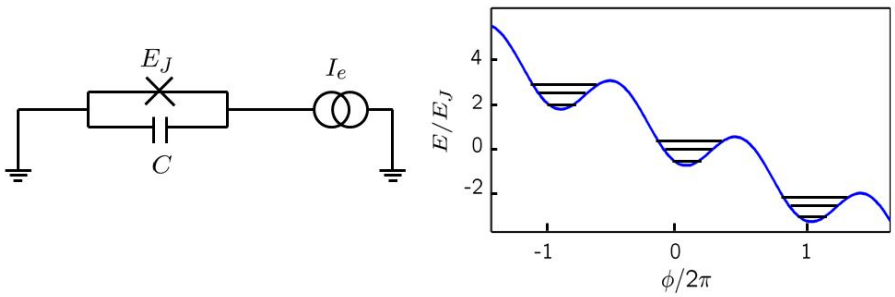

Figure 2.8: Circuit and tilted washboard potential of the current-biased Josephson junction. We took $I_e = E_J e/\hbar$. Levels are only illustrative.

We have already obtained the Hamiltonian of this circuit in Eq. (2.13). A qubit is obtained from this tilted washboard when the bias current I_e approaches the critical current I_C. In this case the phase approaches $\pi/2$ and the potential is well approximated [38] by

$$H \approx \frac{E_J}{I_C}(I_C - I_e)\delta - \frac{E_J}{6}\delta^3\,, \tag{2.20}$$

where $\delta = \phi - \pi/2$. Again we write a qubit Hamiltonian of the form Eq. (2.15) but the coefficients have to be obtained numerically. The current-biased junction, unlike the charge and flux qubits, cannot be operated in point in the parameters space where the qubit energy levels are insensitive to fluctuation to first order. In

addition there can be tunneling out of the local minima leading to decoherence. This tunneling can, to some extent, be turned into an advantage. The tunneling can work as a built-in readout as the states in the cubic potential tunnel through the cubic potential barrier into the continuum outside the barrier with different rates. Varying the current I_e, the authors of [39] where able to engineer tunneling rates from states $|0\rangle$ and $|1\rangle$ different by approximately a factor of a thousand. After tunneling, the particle representing the phase accelerates down the washboard, a convenient amplification process leading to a voltage across the junction. When a finite voltage suddenly appearing across the junction just after tilting the potential we can infer that the qubit was in state $|1\rangle$, whereas $V = 0$ implies that the qubit was in state $|0\rangle$. This process clearly destroys the qubit and nowadays other non-destructive methods are used with success. We discuss such a non-destructive readout proposal in Chapter 5.

We said earlier that a low temperature is needed to keep the Cooper pair from breaking, another constraint in the temperature is to keep the qubit from being thermally flipped. Typical Josephson qubits fall into the $5 - 20GHz$ range, as a temperature of 1K corresponds to a frequency of approximately 21 GHz, if T is in the milikelvin range we can avoid thermal excitations.

Many different designs exploiting Josephson junctions have been proposed and studied, each with its particular advantages ranging from interesting non-linearities to intrinsic qubit protection from decoherence. The subject has been reviewed more than once, see for instance [40, 41].

2.2.4 A word on decoherence

Superconducting qubits are sensitive to environmental noise, which leads to short coherence times because of extrinsic and intrinsic decohering elements. Decoherence caused by extrinsic elements, such as the local electromagnetic environment, has been reduced using better design of the qubits and the surrounding circuitry improving from the basic designs we presented in this Section. But the main intrinsic element that influences the coherence results is the $1/f$ noise. The microscopic mechanisms of $1/f$ noise are still, to a large extent, unknown. With the development of microscopic theories beyond phenomenological models one

could envisage novel methods to actively suppress the effects of the noise. Such understanding is important not only for quantum computing but also for revealing the underlying physics. This problem, however, has proven to be difficult. Nevertheless, the circuit QED community has gone a long way from the first superconducting qubit with coherence times on the order of about 1 ns [33] up to 20 μs [42], i.e. an improvement of 4 orders of magnitude. This was only possible due to the effort of various research groups to reduce the impact of numerous decoherence mechanisms, see for instance [43, 44]. At the same time gates and non-destructive readout schemes have been implemented, much of these tasks were accomplished by the careful manipulation of the artificial atom - cavity field interaction. On the next Section we describe one of the most common cavities fabricated in a circuit.

2.3 Superconducting cavities: coplanar waveguide resonators (CPW)

A CPW of length D can be modeled as a perfectly conducting wire where each unit length element has an inductance l and a capacitance c [30, 45]. The equivalent of Newton's equation on this system is given by

$$l\partial_t I(x,t) + \partial_x V(x,t) = 0\,, \tag{2.21}$$

while charge conservation implies

$$\partial_t q(x,t) + \partial_x I(x,t) = 0\,. \tag{2.22}$$

Before we write a Lagrangian for this system it is convenient to introduce the flux variable

$$\phi(x,t) \equiv \int_{-\infty}^{t} d\tau\; V(x,\tau)\,, \tag{2.23}$$

and we can clearly see that $\partial_t \phi(x,t) = V(x,t)$, moreover from Eq. (2.21) we see that $\partial_x \phi(x,t)$ is proportional to $I(x,t)$. With this the Lagrangian density takes

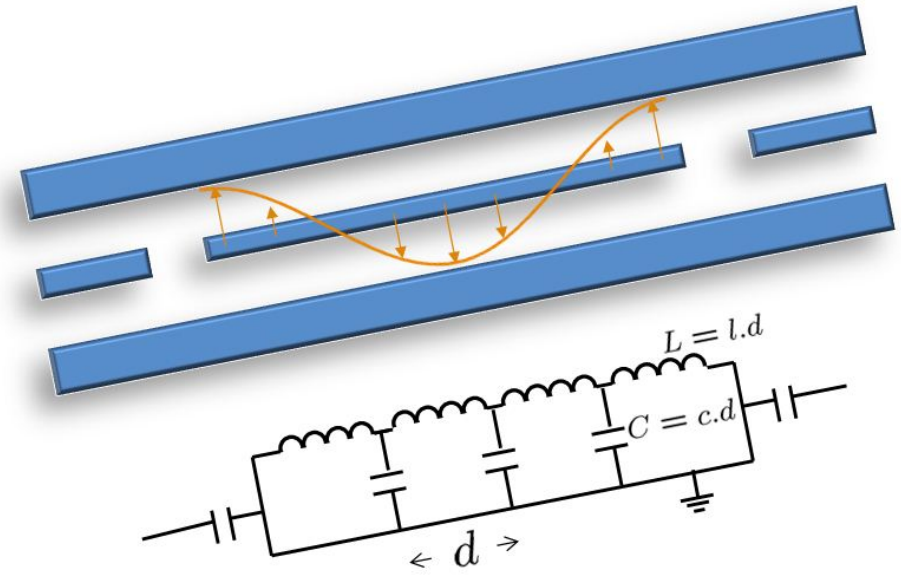

Figure 2.9: Schematic layout and equivalent circuit representation of the coplanar waveguide transmission line. Input and output signals are coupled to the resonator signals are coupled to the resonator, via the capacitance on the extremes.

the form

$$\mathfrak{L} = \frac{c}{2}(\partial_t \phi)^2 - \frac{1}{2l}(\partial_x \phi)^2 \,. \tag{2.24}$$

The Euler-Lagrange equation for this Lagrangian is the wave equation with $v = 1/\sqrt{lc}$ as the wave phase velocity.

The momentum associated with ϕ

$$\frac{\partial}{\partial \dot{\phi}} \int_0^\infty \mathfrak{L}\, dx = cV(x,t) \,. \tag{2.25}$$

is nothing but the charge density $q(x,t)$. And so the Hamiltonian can be written

$$H = \int dx \left[\frac{1}{2c} q^2 + \frac{1}{2l} (\partial_x \phi)^2 \right] . \tag{2.26}$$

The quantization of the Hamiltonian above is achieved by replacing $\phi(x,t)$ and $q(x,t)$ by the operators $\hat{\phi}(x,t)$ and $\hat{q}(x,t)$ which obey canonical commutation relations:

$$[\hat{\phi}(x), \hat{q}(x')] = i\hbar\delta(x-x')\,. \tag{2.27}$$

The Hamiltonian Eq. (2.26) is simply a sum of harmonic oscillators and as such we can define annihilation operators

$$b_k = \frac{1}{\sqrt{L\hbar\omega_k}} \int dx\; e^{-ikx} \left[\frac{1}{\sqrt{2C}} \hat{q}(x) - i\sqrt{\frac{k^2}{2l}}\hat{\phi}(x) \right] , \tag{2.28}$$

where we used for convenience a 'quantization box' of periodic boundary conditions on a length D. As usual the Hamiltonian takes the form

$$H = \sum_k \hbar\omega_k \left(b_k^\dagger b_k + \frac{1}{2} \right) . \tag{2.29}$$

and the commutator $[\hat{\phi}(x), \hat{q}(x')]$ yields the commutation relation

$$[b_{k'}, b_k^\dagger] = \delta_{kk'}\,, \tag{2.30}$$

for the annihilation and creation operators.

2.3.1 Tunable coplanar waveguide resonator

The first resonance mode of a transmission-line resonator has a wavelength $\lambda = 2D$, we have seen on the previous Section that the wave velocity is $v = 1/\sqrt{lc}$ so frequency of this mode will be $\omega_{res} = \pi/D\sqrt{lc}$ where l and c are the inductance and capacitance per unit length of the resonator. Clearly it suffices to control the inductance or capacitance with an external field to have a frequency-tunable resonator. That is precisely what Palacios-Laloy *et al* accomplish in [46] by inserting an array of a few SQUIDs in series in the waveguide central strip.

The SQUID behaves as a lumped non-linear inductance that depends on the magnetic flux Φ across the SQUID. We will wait until Chapter 5 to analyze the

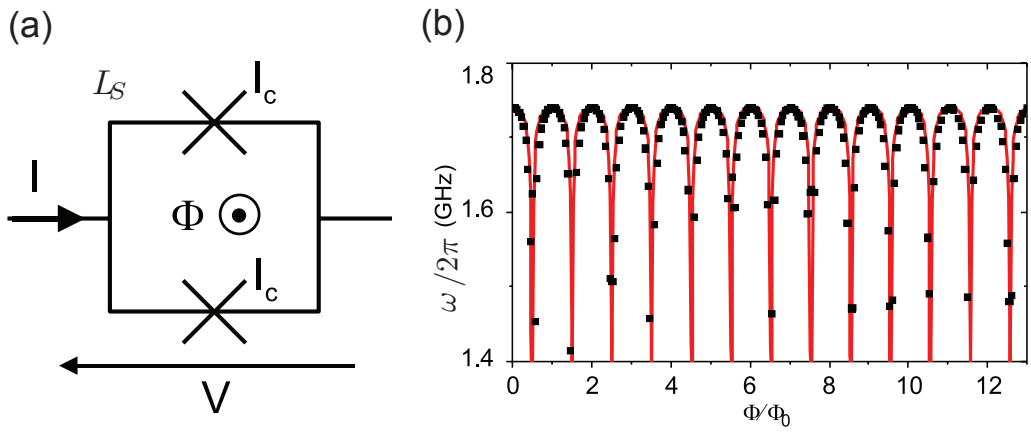

Figure 2.10: (a) Electrical circuit of the dc-SQUID. (b) Measured frequency as a function of the applied magnetic flux for a sample with a single SQUID. The frequency range extends from 1.3 to 1.75 GHz, yielding a tunability range of 30%. Adapted from [46].

Hamiltonian of this SQUID, for the moment we shall assume that the voltage across a SQUID, see Fig. 2.10, can be written as

$$V = L(\Phi, I)\frac{dI}{dt}\,. \tag{2.31}$$

The term $L(\Phi, I)$ is then a flux tunable non-linear inductance. The SQUID self inductance is L_S and the critical current of both Josephson junctions is I_C, if we introduce reduced superconducting flux quantum $\phi_0 = \hbar/2e$. Following [46] we can use the results techniques of Section 2.1 to write the resonator frequency in the linear regime

$$\omega(\Phi) = \frac{\omega_{res}}{1 + N\varepsilon(\Phi)}\,, \tag{2.32}$$

where

$$\varepsilon(\Phi) = \frac{\phi_0/2I_C L_{res}}{|cos(\Phi/2\phi_0)|}\left[1 + \frac{L_S I_C}{\phi_0}\frac{cos(\Phi/\phi_0)}{cos(\Phi/2\phi_0)}\right]\,, \tag{2.33}$$

and N is the number of SQUIDs in series. It is important to note that this scheme does not degrade the quality factor which was measure to be $Q = 3.510^3$ in the data show in Fig. 2.10 (b).

As shown in [46] if the current is comparable to $2I_C|cos(\Phi/2\phi_0)|$ the resonator gets a small additional shift. This additional shift is avoided with the use of an array of SQUIDs which allows one to stay in the linear regime with larger currents.

2.3.2 Cavity-qubit coupling

Analogous to an atom that has a dipole which couples to electromagnetic fields, a circuit can also exchange energy with its electromagnetical environment. The flux qubit can couple to a CPW resonator via the induced magnetic field, as shown in Fig. 2.11. A flux qubit placed at or near the center of the CPW resonator, where there is an antinode of the current standing wave, can strongly couple to the resonator via the mutual inductance. In such a circuit, the vacuum Rabi splitting in the transmission spectrum was observed (Niemczyk 2010; Yang et al., 2003). By employing the magnetic field produced by the current, the flux qubit can also strongly couple to an LC oscillator via a large mutual inductance. Vacuum Rabi oscillations in this system have been observed in (Chiorescu 2004 Johansson 2006).

For charge qubits, electric fields are naturally well suited for coupling to qubits. A circuit involving a CPW resonator and a charge qubit capacitively coupled was theoretically proposed in [19] and experimentally demonstrated in [20], where strong coupling between a single photon and a charge qubit was achieved. In this setup, depicted in Fig. 2.12, the charge qubit is integrated into the ground planes of the transmission line near the antinode of the voltage standing wave for maximum coupling.

To give a concrete example of how a Jaynes-Cummings Hamiltonian can be constructed let us consider the circuit depicted in Fig. 2.12. In this circuit the gate voltage(V_g in Section 2.2.1) has a quantum part that can be written in terms of the annihilation operators defined in 2.28. Here we shall assume the qubit to be fabricated at the center of the resonator. As a result,the qubit is coupled to the mode $k = 2$ of the resonator, which has an antinode of the voltage in its

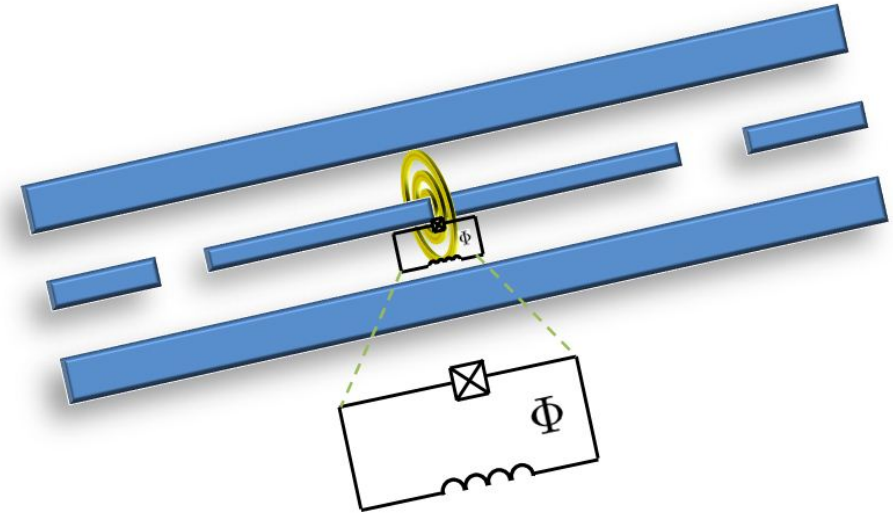

Figure 2.11: Schematic layout of coplanar waveguide resonator coupled to a flux qubit via mutual inductance.

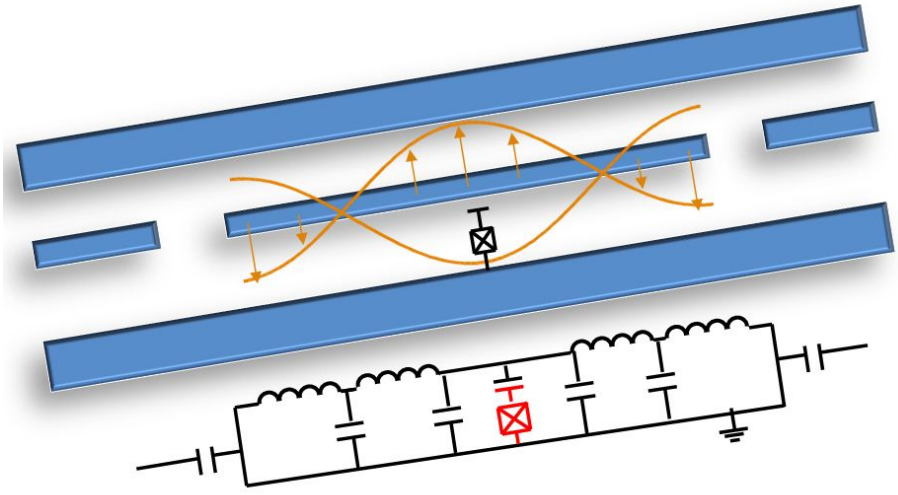

Figure 2.12: Schematic layout of coplanar waveguide resonator coupled through a capacitance with a charge qubit.

center, and we will drop the index k. This way the total Hamiltonian for the qubit operated at $n_g = 1/2$ and resonator is

$$H = \hbar\omega_{res}\left(b^\dagger b + \frac{1}{2}\right) + \hbar\Omega_z\sigma_z - \frac{eC_g}{\hbar(C_J + C_g)}\sqrt{\frac{\hbar\omega_{res}}{C}}(b^\dagger + b)\sigma_x\,, \tag{2.34}$$

where we identify the standard Jaynes-Cummings term with coupling strength $g \equiv \frac{eC_g}{\hbar(C_J+C_g)}\sqrt{\frac{\hbar\omega_{res}}{C}}$. If the natural frequencies of qubit and resonator are much larger than g we can consider the interaction in the so-called 'rotating-wave-approximation'. The coupling term is then written $g(b^\dagger\sigma_- + b\sigma_+)$ as we neglect the counter-rotating terms. In circuit QED, extremely strong coupling is easy to obtain by tuning the circuit parameters, so this approximation is not always valid. Also note that it might actually be harder to obtain weak coupling in such a resonator and the main reason that the cavity is useful is to protect the qubit from the environment by screening the vacuum noise which causes spontaneous emission by Purcell effect [25].

2.3.3 Input-output theory on a transmission line

Input and output signals are coupled to the resonator signals, usually via the capacitive-coupling, allowing measurements of the amplitude and phase of the field radiated and the introduction of qubit-manipulation pulses. The theory relating the field that drives the resonator with the output waves is known as input-output theory. Our discussion will follow the standard references [47, 48], and we will focus on the case we commonly find on circuit QED: the input and output modes will be the modes of a transmission line.

In the situation we aim to describe a single mode resonator couples to the transmission line. The system in the resonator does not however need to be an harmonic oscillator, it suffices that a single degree of freedom obeying bosonic commutation relation $[a, a^\dagger] = 1$ interacts with the external modes. We should note that the distinction between resonator and outside modes is blurred when the quality factor is finite and the cavity is partially open. Nevertheless in the standard input-output theory we keep the original modes as if they where isolated but we introduce an interaction term in the Hamiltonian which allows the

annihilation of an excitation inside the cavity with the creation of an excitation outside and the reciprocal. This perturbative description is, however, highly accurate when the quality factor is large. The coupling Hamiltonian is thus written

$$H_{int} = -i\hbar \sum_k g_k (a^\dagger b_k - b_k^\dagger a)\,, \tag{2.35}$$

where we neglected the counter-rotating terms ab_k and $a^\dagger b_k^\dagger$ as these terms oscillate at high frequencies in the interaction picture and have little effect on the dynamics if the coupling g_k is much smaller than the typical frequencies involved. This term is added to the transmission line Hamiltonian Eq. (2.29) and a general resonator Hamiltonian

$$H = H_{res} + H_{TL} + H_{int}\,. \tag{2.36}$$

The Heisenberg equation yields

$$\dot{b}_k = -i\omega_k b_k + g_k a\,, \tag{2.37}$$

for the transmission line modes and

$$\dot{a} = \frac{i}{\hbar}[H_{res}, a] - \sum_k g_k b_k\,. \tag{2.38}$$

for the resonator bosonic mode. We can formally integrate Eq. (2.37) from the initial condition t_0 before any interaction between the external wave packet and the resonator has happened

$$b_k(t) = e^{-i\omega_k(t-t_0)} b_k(t_0) + g_k \int_{t_0}^{t} d\tau\, e^{-i\omega_k(t-\tau)} a(\tau)\,, \tag{2.39}$$

and inject it in last term in the RHS of Eq. (2.38)

$$\begin{aligned}\sum_k g_k b_k &= \sum_k g_k e^{-i\omega_k(t-t_0)} b_k(t_0) + g_k^2 \int_{t_0}^{t} d\tau\, e^{-i\omega_k(t-\tau)} a(\tau) \\ &= \sum_k g_k e^{-i\omega_k(t-t_0)} b_k(t_0) + g_k^2 \int_{t_0}^{t} d\tau\, e^{-i(\omega_k-\omega_c)(t-\tau)} [a(\tau) e^{-i\omega_c(t-\tau)}] \,.\end{aligned} \tag{2.40}$$

From the first to the second line we arrange the term in square brackets to be slowly varying with τ. The term $e^{-i\omega_c(\tau-t)}$ can be interpreted as the free evolution if the resonator were an harmonic oscillator of frequency ω_c. We make the Markov approximation which assumes that the coupling is essentially constant over the relevant frequencies, i.e. frequencies around ω_c we have

$$\sum_k g_k^2 e^{-i(\omega_k-\omega_c)(t-\tau)} = \kappa\delta(t-\tau)\,. \tag{2.41}$$

Note that κ encompasses both the coupling strength and the transmission line mode density, in fact we have

$$\kappa = 2\pi g^2 \rho\,. \tag{2.42}$$

if g_k is taken constant $g_k = g$ and ρ is defined as

$$\rho = \sum_k \delta(\omega_c - \omega_k)\,. \tag{2.43}$$

If we introduce Eq. (2.41) back in Eq. (2.40) a definite integral, where $\delta(x)$ should be interpreted as a distribution, appears

$$\int_0^\infty \delta(x) = \int \theta(x)\delta(x) \quad . \tag{2.44}$$

The Heaviside step function $\theta(x)$ relates to the delta function as $\delta = \theta'$, consequently $\theta\delta = -\theta\delta + (\theta^2)'$ thus

$$\int dx\, \theta(x)\delta(x) = \frac{1}{2}\int dx\, (\theta^2(x))' = \frac{1}{2} \quad . \tag{2.45}$$

With this result we reach the intermediate expression

$$\dot{a} = \frac{i}{\hbar}[H_{res}, a] - \frac{\kappa}{2}a - \sum_k g_k e^{-i\omega_k(t-t_0)} b_k(t_0)\,, \tag{2.46}$$

we see that the resonator leak to the transmission line originates a damping term for the resonator mode as one could expect. The last terms drives the resonator and if we define the operator

$$b_{input}(t) = \frac{1}{\sqrt{2\pi\rho}} \sum_k e^{-i\omega_k(t-t_0)} b_k(t_0)\,, \tag{2.47}$$

we see that it evolves under the free transmission line Hamiltonian so we physically interpret it as the input field. With this definition we finally get

$$\dot{a} = \frac{i}{\hbar}[H_{res}, a] - \frac{\kappa}{2}a - \sqrt{\kappa}\, b_{input}(t)\,. \tag{2.48}$$

Analogously, the output mode b_{output} is radiated into the transmission line bath and evolves freely thereafter. As the resonator is partially open the output mode will also contain waves radiated by the resonator, these waves contain information about the internal dynamics of the resonator and are thus a way to probe this system. To obtain an equation of motion to the output mode we integrate Eq. (2.37) using a reference time $t_1 > t$ where all the wave packet no longer interacts with the cavity

$$b_k(t) = e^{-i\omega_k(t-t_1)} b_k(t_1) - g_k \int_t^{t_1} d\tau\, e^{-i\omega_k(t-\tau)} a(\tau)\,. \tag{2.49}$$

We proceed in the same fashion as before to obtain

$$\dot{a} = \frac{i}{\hbar}[H_{res}, a] + \frac{\kappa}{2}a - \sqrt{\kappa}\, b_{output}(t)\,. \tag{2.50}$$

where

$$b_{output}(t) = \frac{1}{\sqrt{2\pi\rho}} \sum_k e^{-i\omega_k(t-t_1)} b_k(t_1)\,. \tag{2.51}$$

From Eq. (2.50) and Eq. (2.48) we get the last relation we need

$$b_{output}(t) = b_{input}(t) + \sqrt{\kappa}\, a(t)\,. \tag{2.52}$$

The extension of this formalism to multiple input and output ports is direct, to each additional 'channel' there will be an associated operator with the same form of Eq. (2.47). This formalism will be explored in the next Chapter to model homodyne measurements, which is a typical experiment used to probe indirectly a system coupled to the resonator.

Chapter 3

Strong coupling ensembles of emitters to a resonator

Strong coupling is characterized by recurrent energy exchange between the resonator and the matter field and it takes place if the coupling overwhelms the dissipative processes. This seemly simple condition is a formidable experimental task demanding very high-Q resonators. With a moderate quality factor one can resort to the use of an ensemble of N emitters, in that case the collective coupling is enhanced by a factor $\sqrt{N}$, making it easier to meet the strong coupling requirements. In fact it took almost a decade for the experiments showing collective Rabi oscillations with 10^4 atoms [2] to be refined to the point where vacuum Rabi splitting with one atom (on average) could be observed [49, 50]. Another example comes from experiments with semiconductor nanostructures where the first strong coupling signatures were obtained in monolithic semiconductor quantum microcavity containing an ensemble of quantum wells [51]. Other systems could benefit from collective coupling including semiconductor nanocrystals [52], self-assembled quantum dots [53] and molecules in organic crystals [54].

The interest for this topic has been renewed in the framework of quantum information, with proposals to use collections of emitters as quantum memories for individual excitations. Indeed, ensembles of microscopic degrees of freedom benefit from the collective enhancement of the interaction strength , while possibly keeping the relaxation properties of a single emitter [55]. This led to a series

of recent proposals where cold atoms [56], polar molecules [57] or electronic spins [58, 55] coupled to a superconducting cavity have been suggested as long-storage quantum memories and optical interfaces. Following these proposals, recent experiments have demonstrated the strong coupling of a resonator to a collection of electronic spins in a crystal [59, 60]. This idea is particularly compelling for superconducting circuits where the Josephson junction based qubits, which couple strongly to electromagnetic fields enabling quantum information processing, could be complemented by ensembles of emitters with very high coherence times but rather small coupling with electromagnetic fields. In addition, the spin ensemble contains many collective modes that could be explored for example if one could apply a strong magnetic field gradient to make different modes interact selectively with the cavity as proposed in [61]. In this way, the spin ensemble could act as many quantum registers storing a large number of logical qubits.

In atomic experiments, although there is a finite broadening of the atomic spectra (due to Doppler broadening for instance) it is usually small compared to the cavity linewidth or the coupling strength. For this reason we can safely describe this ensemble as N identical atomic oscillators. In this case only one collective mode couples with the cavity and we have a direct analogy with the single-emitter case if we scale the coupling constant by a factor $\sqrt{N}$ [62]. However, in solid state systems the broadening is frequently larger than the cavity linewidth or the coupling strength (and the ensemble can no longer be reasonably approximated by an ensemble of identical emitters). That is the main motivation for this chapter, where we make a theoretical investigation on the properties of a system consisting in a resonator 'filled' with a large number of two-level emitters non-degenerate in frequency [1].

As we will see throughout this Chapter, we have to pay attention not only to the width of the emitters distribution but also on its shape which can vary among different systems and even different samples of the same system. We will show that provided the spectral density of emitters in the wings of the distribution decays faster than a Lorentzian, the losses will be dominated by the cavity and the emitters homogeneous linewidth (for large enough coupling).

[1] Parts of this chapter have been published in Physical Review A **00**, 003800 (2011)

3.1 Modelling transmission

The system under study is pictured in fig.3.1. To build the proper hamiltonian we have to modify Eq. (3.1) to account for the frequencies inhomogeneity

$$\frac{\hbar\omega_0}{2}\sum_{j=1}^{N}\sigma_z^j \quad \Rightarrow \quad \frac{\hbar}{2}\sum_{j=1}^{N}\omega_j\sigma_z^j\,. \tag{3.1}$$

From now on we consider the so called low-excitation regime in which the number of excitations is small compared to the total number of emitters. In this regime the behavior of a two-level system cannot be distinguished from the behavior of the two lower levels of a harmonic oscillator. In fact if the probability of exciting the j-th emitter is small we have $\langle\sigma_z^j\rangle = -1/2$ and the raising and lowering atomic operators which are analogous to creation and annihilation operators will display bosonic commutation relation : $[\sigma_-^j, \sigma_+^j] = -2\sigma_z^j \approx 1$. Each two-level emitter is properly modeled by a bosonic mode b_k (Holstein-Primakoff approximation). The total Hamiltonian writes

$$H = \hbar\omega_0 a^\dagger a + \sum_{j=1}^{N}\hbar\omega_j b_j^\dagger b_j - i\hbar\sum_j g_j(b_j^\dagger a - a^\dagger b_j)\,. \tag{3.2}$$

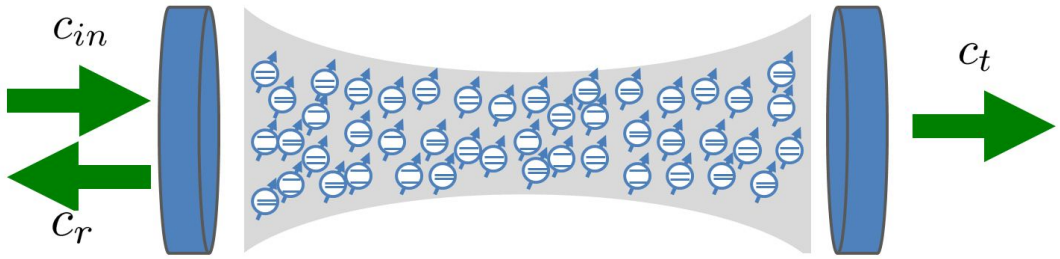

Figure 3.1: Scheme of the emitters-cavity coupled system. The cavity frequency is ω_0. The cavity mode is coupled to the outside world via two ports, on the left we have input and reflected channels and on the right we have the transmitted one. The j-th two-level system has frequency ω_j and interacts with the cavity mode with coupling constant g_j.

The Hamiltonian above corresponds to the resonator Hamiltonian in the lan-

guage of Section 2.3.3 where we presented the input-output formalism. The external modes are combined into the operators c_{in} (injected or pumping field), c_r (reflected field) and c_t (transmitted field) that lead to the damping κ of the intracavity field as in Eq's 2.47 and 2.51 . We also consider atomic losses γ, i.e. atomic emission in modes other than the cavity mode, these terms contributing to the damping of the emitters without pumping the resonator mode. With Eq. (2.48), the Heisenberg equations are written in the frame rotating at the frequency ω of the probe as

$$\begin{aligned}
\dot{a} &= -\left(\kappa/2 + i(\omega_0 - \omega)\right) a - \sqrt{\kappa/2} c_{in} + \sum_k g_k b_k \,, \\
\dot{b_k} &= -\left(\gamma/2 + i(\omega_k - \omega)\right) s_k - g_k a + \Xi(t) \,, \\
c_r &= c_{in} + \sqrt{\kappa/2} a \,, \\
c_t &= \sqrt{\kappa/2} a \,,
\end{aligned} \tag{3.3}$$

where $\Xi(t)$ is a noise operator associated with the atomic decay γ [47]. From this set of equations, and as demonstrated in Appendix A.1, it comes out that the evolution of the system can be modeled with a generalized Hamiltonian H_{eff} involving the respective complex emitters and cavity frequencies $\tilde{\omega}_k = \omega_k - i\gamma/2$ and $\tilde{\omega}_0 = \omega_0 - i\kappa/2$. Consequently, the system made of N atoms coupled to a cavity appears to be equivalent to an ensemble of $N+1$ coupled leaky cavities, and the problem reduces to the study of the classical evolution of the field in each cavity. This analogy is the basis of the model. Taking the average value and solving analytically the set of equations in the steady state regime, we get the following expression for the complex transmission of the cavity:

$$t(\omega) = \frac{\langle c_t \rangle}{\langle c_{in} \rangle} = \frac{-\kappa/2i}{\tilde{\omega}_0 - \omega - \sum_k g_k^2/(\tilde{\omega}_k - \omega)} \,. \tag{3.4}$$

The complex transmission can be directly measured via a homodyne measurement, if phase reference is not kept we will measured instead the transmission in energy $|t(\omega)|^2$. We are interested in the very large number of emitters N, so we describe the emitters as a continuous distribution with spectral density $\rho(\omega)$

spread around its central frequency ω_c and normalized to 1. The full width at half maximum (FWHM) is denoted Δ, and is used to parametrize each distribution. We define the spectral density distribution as $\rho(\omega) = \sum_k g_k^2 \delta(\omega - \omega_k)/\Omega^2$, where $\Omega^2 = \sum_k g_k^2$. Introducing this definition in eq.(3.4) and using the identity $1/(\omega_k - \omega - i\gamma) = \int d\omega' \delta(\omega' - \omega_k)/(\omega' - \omega - i\gamma)$ we obtain

$$t(\omega) = \frac{\kappa/2i}{\omega - \omega_0 + i\kappa/2 - W(\omega)}\,, \tag{3.5}$$

with

$$W(\omega) = \Omega^2 \int_{-\infty}^{\infty} \frac{\rho(\omega')d\omega'}{\omega - \omega' + i\gamma/2}. \tag{3.6}$$

In the following we consider three different continua, namely a Gaussian, a Lorentzian, and a rectangular distribution. Gaussian broadening is quite common in nature, from Doppler-broadened lines in gases to e.g. size distributions in ensembles of semiconductor nanocrystals [52] and self-assembled quantum dots [53]. Lorentzian distributions can be found in certain solid-state systems, such as spin ensembles in dipolar interaction [63] or dilute optically active impurities in crystals [64]. Finally, the rectangular distribution is a prototypical example of finite bandwidth distribution. The results obtained in this case can for instance qualitatively be applied to dilute ensembles of fluorescent molecules in organic crystals [54]. For these three distributions, we have obtained analytical expressions for the function $W(\omega)$, which are detailed in Appendix A.2.

3.2 Properties of the transmission function

We start this Section recalling some well-known results in the absence of inhomogeneous broadening ($\Delta = 0$). In that case, the distribution $\rho(\omega)$ is well described by a Dirac delta function, leading to $W(\omega) = \Omega^2/(\omega + i\gamma/2)$, and the transmission function has two poles $\lambda_\pm = \pm\sqrt{\Omega^2 - ((\kappa-\gamma)/4)^2} + i\dfrac{\kappa+\gamma}{4}$ [65]. Strong coupling is reached if $\Omega \gg \kappa, \gamma$ and is manifested by the appearance of a doublet in the transmission pattern located at $\pm\Omega$ (at first order in $\kappa/\Omega, \gamma/\Omega$). These two peaks are the spectral counterpart of the coherent and reversible exchange

of a quantum of energy between the cavity field and the symmetrical state $|S\rangle$ of the emitters ensemble. The transmission coefficient $t(\omega)$ is proportional to the Fourier-Laplace transform of the field's amplitude in the cavity initially fed with a single excitation $\langle 1,G|\, e^{-iH_{eff}t/\hbar}\, |1,G\rangle$ (this result is demonstrated in Appendix A.1, generalizing ref.[66] and is also valid in the case where $\Delta > 0$). The so-called collective Rabi oscillation takes place at the frequency Ω defined above, which in that case simply equals $\Omega = g_0\sqrt{N}$, and is damped on a timescale given by the finite linewidth of the peaks. In that temporal picture, strong coupling is reached when the excitation is exchanged several times before being lost in the environment.

We now study how the strong coupling features are modified by inhomogeneous broadening. We have plotted the transmission in energy $|t(\omega)|^2$ for Ω/Δ ranging from 0 to 3.5 in fig.3.2. To be only sensitive to the influence of inhomogeneous broadening, we have kept κ and γ negligible with respect to Ω. We have considered the three types of distributions introduced in Sec. 3.1, namely Lorentzian (a), Gaussian (b) and rectangular (c). Whatever the distribution, two peaks appear in the transmission pattern when $\Omega > \Delta$, a signature of Rabi oscillation in the temporal domain. A first rough interpretation is that strong coupling is reached when dephasing processes, that take place on a timescale Δ^{-1}, are slower than than energy exchanges, whose period still scales like Ω^{-1}. Note that the Rabi period is a collective quantity involving all the emitters, even emitters which are not spectrally matched to the cavity mode. This apparently puzzling feature had already been evidenced in [67] and is due to the fact that the mode interacts with a collective state of the matter field.

Inhomogeneous broadening not only states a novel condition to fulfill to ensure strong light-matter coupling. As it eventually accelerates the damping of Rabi oscillations, it also leads to the broadening of the polaritonic peaks, as it clearly appears in fig.3.2. In particular, the shape of the emitters distribution has a dramatic influence. An analytical expression for this width can be derived, in perturbation with respect to the small parameter Δ/Ω : namely, departing from the strong coupling case in the absence of inhomogeneous broadening, we evaluate how the poles of the transmission function are modified when $0 < \Delta \ll \Omega$. For the sake of simplicity we consider the limit $\gamma = 0$. The case of finite γ is

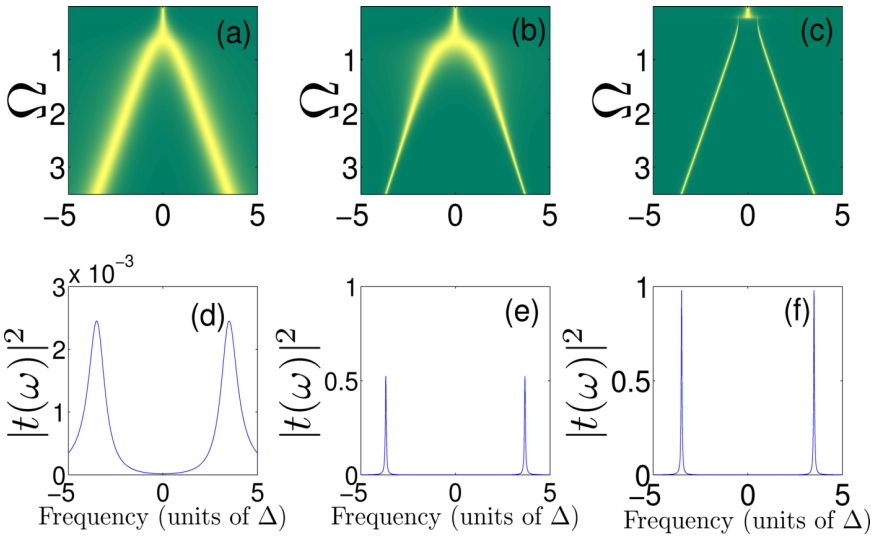

Figure 3.2: (Color online). Transmission of a cavity resonantly coupled to a broad distribution of emitters. (a,d) : Lorentzian; (b,e) : Gaussian; (c,f) : Rectangular. We took $\Delta = 1$ MHz, $\kappa = 0.1$ MHz, $\gamma = 10^{-4}$ MHz. Bottom : $\Omega = 3.5$ MHz. These values are typical of NV centers coupled to a superconducting resonator.

studied in Appendix A.3 in the limit $\gamma \ll \Delta$, which corresponds to the experimental situations we aim to describe. Using the Sokhatsky-Weierstrass formula in eq.(3.6) we have

$$\frac{W(\omega)}{\Omega^2} = P\int_{-\infty}^{\infty} \frac{\rho(\omega')d\omega'}{\omega - \omega'} - i\pi\rho(\omega)\,. \tag{3.7}$$

The modified poles of the transmission function are expected in the vicinity of $\pm\Omega$, so that we develop the expression of $W(\omega)$ for $\omega \sim \Omega \gg \Delta$:

$$W(\omega) = \frac{\Omega^2}{\omega}(1 + \mathcal{O}(\Delta^2/\omega^2)) - i\pi\Omega^2\rho(\omega)\,, \tag{3.8}$$

yielding for the poles of the transmission function (at first order in κ/Ω and second order in Δ/Ω), $\lambda_\pm = \pm\Omega + i\frac{\kappa+2\pi\Omega^2\rho(\Omega)}{4}$. Finally, keeping a finite γ leads

to the modified expression for the full width at half maximum of the peaks :

$$\Gamma = (\kappa + \gamma + 2\pi\rho(\Omega)\Omega^2)/2. \tag{3.9}$$

Looking at eq.(3.9), it appears that in the strong coupling regime, the polaritonic peaks remain located at $\pm\Omega$, but that inhomogeneous broadening adds a contribution to their linewidth. This contribution writes $2\pi\Omega^2\rho(\Omega)$ and scales like the density of emitters at the real frequency of the poles. This feature explains the sensitivity to the distribution shape that clearly appears in fig.3.2. The polaritonic linewidth decreases upon increasing Ω, provided the distribution $\rho(\omega)$ decays faster than $1/\omega^2$. The Lorentzian distribution is the limiting case for which the linewidth tends towards a constant Δ : whatever the coupling, the polaritonic linewidth is governed by inhomogeneous broadening. On the contrary, in the Gaussian and rectangular cases, increasing the ratio Ω/Δ allows to get rid of the influence of the parameter Δ, so that the width of the peaks only depends on the losses of the cavity and of individual emitters. In the rectangular case, this ideal behavior is even reached for finite values of the collective coupling strength Ω (while it remains a limit in the Gaussian case). This effect, that we call *cavity protection*, leads to an enhanced lifetime of the Rabi oscillation and has interesting consequences for quantum information storage as we show in Section3.5.

3.3 Origin of peak broadening

Before focusing on applications opened by cavity protection, we give an interpretation of peaks broadening. This amounts to understanding the damping of Rabi oscillations, which occurs even in the absence of any radiative losses $\kappa = \gamma = 0$. Our approach is based on a seminal paper of Fano [68], and consists in the diagonalization of the total Hamiltonian of the system $H = H_{cav} + H_{em} + H_{int}$.

In the absence of inhomogeneous broadening, preparing the system in the initial state $|1, G\rangle$ gives rise to Rabi oscillations between the atoms and the field. This state is a coherent superposition of two eigenstates of the Hamiltonian, namely the polaritons $\left|\psi_{\pm}^{0}\right\rangle = \frac{1}{\sqrt{2}}|0, S\rangle \pm i\frac{1}{\sqrt{2}}|1, G\rangle$, of energies $\pm\hbar\Omega$, where $|S\rangle$ is

the symmetrical matter state defined in Section III. Rabi oscillation is a quantum beat between these two components. In particular, all other emitters states, which do not interact with the electromagnetic field and are usually called "dark states", remain uncoupled.

The presence of inhomogeneous broadening strongly modifies the features of the emitters cavity coupling. We start the diagonalization by a change of basis from the bare emitters to a set of coarse grained states $\{|\omega\rangle\}$ regularly spaced in frequency. Consider you have a very large number of emitters distributed according to $\rho(\omega)$. Now let

$$|\omega\rangle = \frac{1}{\sqrt{\varepsilon}} \frac{1}{\sqrt{\rho(\omega)}} \sum_{\omega-\frac{\varepsilon}{2}<\omega_k\leq\omega+\frac{\varepsilon}{2}} |e_k\rangle \ , \tag{3.10}$$

we assume ε is small enough that the variation of $\rho(\omega)$ can be disregarded in this scale. In the limit of small ε these are the only states that interact with the cavity. This happens because we are forming locally symmetric states. The matrix elements of the Hamiltonian between excited resonator and $|\omega\rangle$ is

$$\begin{aligned} \langle\omega| H |1,G\rangle &= \langle\omega| \left(|1,G\rangle \langle 1,G| + \sum_k |e_k\rangle \langle e_k| \right) H |d\rangle \\ &= \sum_k g_k \langle\omega|e_k\rangle \\ &= \sqrt{\varepsilon}\sqrt{\rho(\omega)} g(\omega) \, . \end{aligned} \tag{3.11}$$

where $g(\omega)$ is the average coupling around $g(\omega)$. We can regain a 'coarse grained' continuous if we make $\varepsilon \to 0$. This way we end up with a continuous of states distributed with constant density in the ω axis that interact with the discrete cavity levels. We drop ε and make the interaction strength Ω normalized 'per unit frequency/energy'. As we are only interested in eigenstates which are not 'dark' all the matrix elements we need are

$$\begin{cases} \langle 1,G| H |1,G\rangle = \hbar\omega_0 \, , \\ \langle\omega'| H |1,G\rangle = \hbar\Omega\sqrt{\rho(\omega')} \, , \\ \langle\omega'| H |\omega\rangle = \hbar\omega\delta(\omega-\omega') \, , \end{cases} \tag{3.12}$$

as the remaining emitter states form a subspace which does not communicate via H. We shall now prove that the matrix element of H between two states each from one subspace are zero. Let $|\omega, e_k\rangle$ be the bare excited emitters on the bin of size ε around the frequency ω with k ranging from 1 to the total number of emitters in this bin $N(\omega)$. In addition to the vector $|\omega, 1\rangle = |\omega\rangle$ defined in Eq. (3.10) we have the orthonormal set

$$|\omega, j\rangle = \frac{1}{\sqrt{j(j-1)}} \sum_{k=1}^{j-1} |\omega, e_k\rangle - (j-1)\,|\omega, e_j\rangle \ , \tag{3.13}$$

for $j \in [2, N(\omega)]$, these are 'dark-states' that complete the basis to the one-excitation manifold. Nevertheless it is easy to see that

$$\begin{cases} \langle \omega, j|\, H\, |1, G\rangle = 0, \\ \langle \omega, j|\, H\, |\omega, 1\rangle = \frac{1}{\sqrt{N(\omega)}\sqrt{j(j-1)}} \sum_k^{j-1} (\omega_k - \omega_j) < \varepsilon, \end{cases} \tag{3.14}$$

and in the $\varepsilon \to 0$ limit the two subspaces decouple.

An eigenvector $|\psi_\omega\rangle$ of H with energy $\hbar\omega$ is searched under the form

$$|\psi_\omega\rangle = a(\omega)\,|1, G\rangle + \int d\omega' b(\omega, \omega')\,|\omega'\rangle \ , \tag{3.15}$$

where the quantity $|a(\omega)|^2$ is normalized with respect to ω. From the eigenvalues equation we get the system

$$\begin{aligned} a(\omega)\omega_0 + \int d\omega' b(\omega, \omega')\Omega\sqrt{\rho(\omega')} &= a(\omega)\omega \\ a(\omega)\Omega\sqrt{\rho(\omega')} + b(\omega, \omega')\omega' &= b(\omega, \omega')\omega \, . \end{aligned} \tag{3.16}$$

The continuous spectrum poses some difficulties, the solution of this set of equations involve a division by $\omega - \omega'$ which might be zero. This obstacle has been circumvented by Fano in [68] with the introduction of an Ansatz already containing a delta-like singularity

$$b(\omega, \omega') = \left[\frac{1}{\omega - \omega'} + z(\omega)\delta(\omega - \omega')\right] a(\omega)\Omega\sqrt{\rho(\omega')} \ , \tag{3.17}$$

where the term $(\omega - \omega')^{-1}$ should be taken as the principal part of the integral and $z(\omega)$ is to be determined latter. The substitution in Eq. (3.16) yields

$$z(\omega) = \frac{C(\omega)}{\Omega^2 \rho(\omega)}\,, \tag{3.18}$$

where

$$C(\omega) = \omega - \omega_0 - \Omega^2 \, P\!\int d\omega' \frac{\rho(\omega')}{\omega - \omega'}\,, \tag{3.19}$$

and $P\!\int$ stands for principal value. At this point we already have $a(\omega)$ and $b(\omega, \omega')$ up to a normalization factor. Ensuring that $|\psi_\omega\rangle$ are normalized yields

$$|\psi_\omega\rangle = \frac{\sqrt{\rho(\omega)}\Omega \left(|1, G\rangle + P\!\int d\omega' \frac{\sqrt{\rho(\omega')}\Omega}{\omega - \omega'} |\omega'\rangle \right) + C(\omega) |\omega\rangle}{\sqrt{C(\omega)^2 + (\pi \rho(\omega) \Omega^2)^2}}\,. \tag{3.20}$$

We have implicitly assumed that the distribution support is not bounded, as it is the case for Lorentzian and Gaussian. If this is not the case other solutions are possible as we discuss later. The amplitude of probability to find the excitation in the cavity mode can finally be written

$$\begin{aligned} \langle 1, G| \, e^{-iHt/\hbar} \, |1, G\rangle &= \langle 1, G| \, e^{-iHt/\hbar} \int d\omega' a^*(\omega') \, |\psi_{\omega'}\rangle \\ &= \int d\omega' |a(\omega')|^2 e^{-i\omega' t}\,. \end{aligned} \tag{3.21}$$

It can easily be shown that $|a(\omega)|^2$ is proportional to the transmission coefficient in energy $|t(\omega)|^2$ (namely, $|a(\omega)|^2 = \Omega^2 \rho(\omega) \left| \frac{t(\omega)}{\kappa/2} \right|^2$ for $\gamma, \kappa \to 0$), so that $|t(\omega)|^2$ corresponds to the Fourier transform of the occupation amplitude of the cavity mode. As we have checked in Appendix A.4, this result is completely consistent with the formalism of Laplace transform used in Section III in the absence of external sources of loss.

This approach sheds new light on the transmission function studied in Section III, which directly reflects the overlap between the initial state $|1, G\rangle$ and the continuum of eigenstates $|\psi_\omega\rangle$ of the Hamiltonian. The two peaks characteristics of

the strong coupling regime show that this initial state is a coherent superposition of two wave packets, reminiscent of the polaritons obtained when $\Delta = 0$. As the eigenstates of the Hamiltonian form an infinite continuum, these wavepackets always have a finite width, responsible for the damping of Rabi oscillations. Nevertheless, as it was shown above, increasing the collective coupling Ω may drastically change the shape of this overlap and eventually, lead to the narrowing of the peaks for distributions $\rho(\omega)$ decaying faster than ω^{-2}, a phenomenon that was defined above as cavity protection.

Distributions with a bounded support of width Δ (rectangular for example), provide an interesting limiting case where cavity protection is almost perfect. As a matter of fact, if $\Omega > \Delta$, the Hamiltonian eigenstates not only consist in a continuum ψ_ω lying within the support of the distribution, but also in two discrete states $|\psi_+\rangle$ and $|\psi_-\rangle$, located around $\omega = \pm\Omega$ (at first order in Δ/Ω), corresponding to the polaritons $\left|\psi_+^0\right\rangle$ and $\left|\psi_-^0\right\rangle$ when $\Delta = 0$. The initial state $|1, G\rangle$ mostly overlaps with these two eigenstates, making the problem similar to the case of standard Rabi oscillations in the absence of inhomogeneous broadening. In particular, if $\rho(\omega)$ is rectangular, the overlap of $|1, G\rangle$ with the discrete states equals $\mathcal{C} = 1 - (1/8)(\Delta/\Omega)^2$, giving rise to Rabi oscillations of infinite duration characterised by a contrast $\mathcal{C}$.

To conclude this part, we emphasize that the total damping rate $\Gamma = (\kappa + \gamma + 2\pi\rho(\Omega)\Omega^2)/2$ evidenced in Section III shows contributions of essentially different nature. The first type, related to κ and γ, is due to the irreversible loss of the excitation in the environment of the cavity or the emitters. The second type, related to $\pi\rho(\Omega)\Omega^2$, is Hamiltonian and thus reversible in principle with CRIB experiments. It is due to the interaction of the cavity with a continuum of emitters, leading to progressive dephasing of Rabi oscillations.

3.4 Open system approach

The approach developed in Section IV gives an interpretation of the peaks broadening within a Hamiltonian formalism. In this part, we adopt another point of view based on quantum open systems. As it was exposed above and pictured in fig.3.3, in the absence of inhomogeneous broadening, the symmetrical state

$|S\rangle$ is decoupled from the dark states. The excitation initially injected in the cavity mode remains thus trapped in the 'small system' consisting in the two polaritons $\left|\psi_{+}^{0}\right\rangle$ and $\left|\psi_{-}^{0}\right\rangle$. When inhomogeneous broadening is switched on, the symmetrical state couples to the dark states, which appear as an environment in which the excitation can decay. Broadening of the polaritonic peaks can be attributed to the decoherence induced by the bath of dark states. This picture is inforced by the computed expression for the width of the transmission peaks, $\Gamma = 2\pi\Omega^2\rho(\Omega)$, which could be interpreted as a natural linewidth for polaritons 'dressed' by the environment of dark states. Nevertheless, the analogy should be used with caution, as the coupling with the bath is not Markovian. This naive picture has still the advantage to give an intuitive insight on cavity protection, which is nothing but energetically decoupling the polaritons from the bath of dark states, as initially suggested in [69].

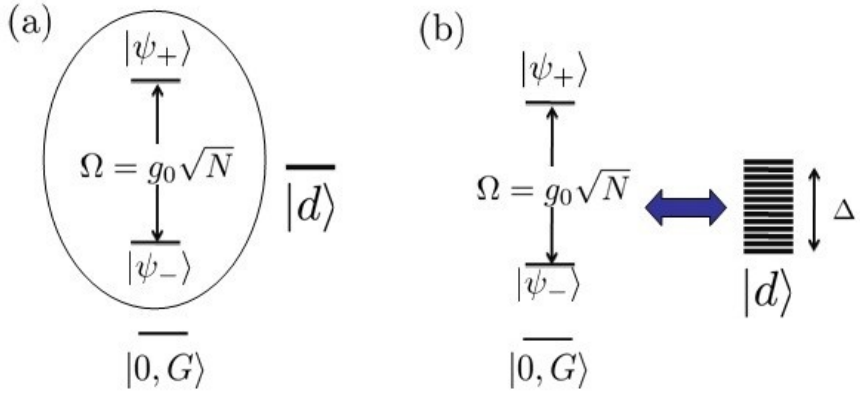

Figure 3.3: (Color online). Schematic diagram of the open system approach to inhomogeneous broadening. (a): $\Delta = 0$, the states $|\psi_{\pm}\rangle$ are isolated from the degenerate dark states $|\omega\rangle$. (b): $\Delta \neq 0$, the states $|\psi_{\pm}\rangle$ are coupled to the $|\omega\rangle$ states, which are non-degenerate in this case, with a coupling strength proportional to Δ .

To study the dynamics of the polaritonic relaxation, we have exactly computed the evolution of the state of the system initially prepared in $\left|\psi_{+}^{0}\right\rangle$, for different values of the collective coupling strength Ω, and for the three types of distribution, keeping the same FWHM $\Delta = 1$MHz. We have plotted in fig.3.4 the probability $|\left\langle\psi_{+}^{0}\right| e^{-iH_{eff}t}\left|\psi_{+}^{0}\right\rangle|^2$ of finding the excitation in the polariton, as a function of

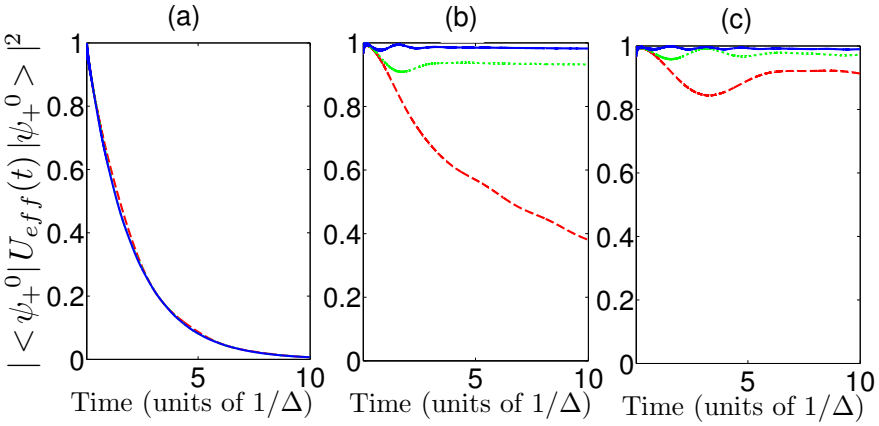

Figure 3.4: (Color online). Probability to recover an excitation initially stored in the state $|\psi_+\rangle$ after a time t. We took $\Delta = 1$ MHz, $\kappa = \gamma = 0$. (a) : Lorentzian ; (b) : Gaussian ; (c) : Rectangular. Red Dashed line : $\Omega = 1$ MHz; Green Dotted line : $\Omega = 2$ MHz; Blue line : $\Omega = 4$ MHz.

time. For the sake of clarity, we have neglected again the losses $\kappa = \gamma = 0$ (realistic values are considered below). As it can be seen in the figure, if the distribution is Lorentzian, the excitation exponentially decays in the environment, whatever the coupling Ω, on a typical timescale Δ^{-1}. This is consistent with the spectral study performed in Section III, where the width of the polaritonic peaks does not depend on the coupling with the cavity. On the contrary, the effect of cavity protection can be observed on the two other distributions. Damping is strongly inhibited as soon as $\Omega > \Delta$ if the distribution is Gaussian, but is always present whatever the coupling, which is the counterpart of the finite linewidth of the transmission peaks. Finally, in the case of a rectangular distribution, two timescales are visible. The initial state $\left|\psi_+^0\right\rangle$ mostly overlaps with the discrete state $|\psi_+\rangle$ defined above, but also with the continuum of eigenstates $|\psi_\omega\rangle$. The coherent superposition of the continuum of frequencies is damped on a short timescale Δ^{-1}, so that the probability quickly converges towards the quantity $|\left\langle\psi_+^0\right|\psi_+\rangle|^2$, which also scales like $(\Delta/\Omega)^2$.

3.5 Application to quantum memories

The previous Section establishes that for distributions allowing cavity protection, increasing the collective coupling Ω dramatically increases the potential storage time of one excitation in the polaritonic states, as energetic decoupling from the dark states is more pronounced. In particular, this storage time becomes insensitive to dephasing processes induced by inhomogeneous broadening. This allows to treat an inhomogeneous distribution as an effective oscillator of ground state $|G\rangle$ and first excited state $|S\rangle$, that benefits from the collective coupling Ω to the cavity and whose relaxation properties are solely governed by individual emitter properties γ. As a consequence, cavity protection opens the path to the implementation of long lived solid-state quantum memories, by exploiting ensembles of microscopic degrees of freedom, whose coherence times are remarkable. In this Section we use our modelling to estimate the performances of two such types of quantum memories.

3.5.1 Quantum memory based on dispersive coupling

Here we evaluate the potential of a broad ensemble of emitters dressed by a cavity mode for quantum information storage. The coupling should be dispersive to freeze Rabi oscillations between the mode and the atoms. This system offers an interesting situation where information has to be protected against two types of losses : the cavity losses, which are more critical when the mode and the distribution of emitters are on resonance, and the losses in the dark states, which on the contrary, are weaker as the atoms-cavity detuning is smaller. The atoms-cavity detuning is thus the cause of a tradeoff, and can be optimized with our modelling, as we show below.

The protocol of the quantum memory is the following. First, the detuning δ between the mode and the center of the distribution is slowly swept from $-\infty$ to a finite positive value, thus adiabatically mapping the quantum state of the cavity mode onto the emitter's ensemble : $(\alpha\,|0\rangle + \beta\,|1\rangle)\,|G\rangle \rightarrow |0\rangle\,(\alpha\,|G\rangle + \beta\,|\psi_+^0(\delta)\rangle)$. We have introduced the dressed state $|\psi_+^0(\delta)\rangle = \cos(\theta/2)\,|0,S\rangle + i\sin(\theta/2)\,|1,G\rangle$, and the mixing angle $\cot(\theta) = \delta/(2\Omega)$. The transfer of the excitation should be realized on a timescale longer than the Rabi period, but shorter than Δ^{-1} so that

no dephasing mechanism affects the process, this can be achieved under strong coupling as in this case $\Omega \gg \Delta$. The expected fidelity $\mathcal{F}(t)$ of such a quantum memory can be exactly computed with the present model; in particular, in the case where a single photon state is stored ($\beta = 1$), we get the simple expression $\mathcal{F} = |\langle\psi_+^0(\delta)| e^{-iH_{eff}t} |\psi_+^0(\delta)\rangle|^2$. We have plotted this quantity in fig.3.5. As explained above, $\mathcal{F}$ must be optimized by properly choosing the detuning δ, which should be low enough to maintain cavity protection, and high enough to reduce the sensitivity to cavity losses, which typically scale like $\kappa(\Omega/\delta)^2$. The maximal detuning δ_M leading to an efficient protective energy gap is $\Omega^2/\delta_M \sim \Delta$[70]. This condition induces an optimal reduction of the cavity losses by a factor of $(\Omega/\Delta)^2$.

The trade-off in the detuning clearly appears in the inset of fig.3.5, where we have plotted $\mathcal{F}$, as a function of the detuning δ, after ten cavity lifetimes, for different values of the ratio Ω/Δ. We have used standard parameters for circuit QED technology [59]. As it appears in the figure, a quantum memory based on a Gaussian distribution of emitters of linewidth $\Delta = 1$ MHz, strongly coupled to a cavity of width $\kappa = 0.1$ MHz with a strength $\Omega = 40$ MHz would yield a typical fidelity of 90% after 100 μs, a remarkable storage time compared to the lifetime of the cavity mode (10 μs) and the typical dephasing time of the ensemble (1 μs).

3.5.2 Quantum memory based on two emitters distributions

We focus now on a second type of quantum memory, based on two distributions of emitters allowing cavity protection, respectively detuned by $+\delta$ and $-\delta$ with respect to a cavity. Note that the case of a mode coupled to two such *discrete* emitters of ground and excited states $|g_i\rangle$ and $|e_i\rangle$ is exactly solvable, the poles of the transmission revealing the complex eigenfrequencies of the system [71]. In particular, when the emitters are on resonance with the mode ($\delta = 0$), the antisymmetrical state $(|e_1, g_2\rangle - |g_1, e_2\rangle)/\sqrt{2}$ is not coupled to the electromagnetic field. This dark state is naturally protected against spontaneous emission in the cavity, a property that can be used to store quantum information during a typical timescale given by the atomic dephasing time. Note that for artificial atoms like superconducting qubits or quantum dots this time can be quite short, which

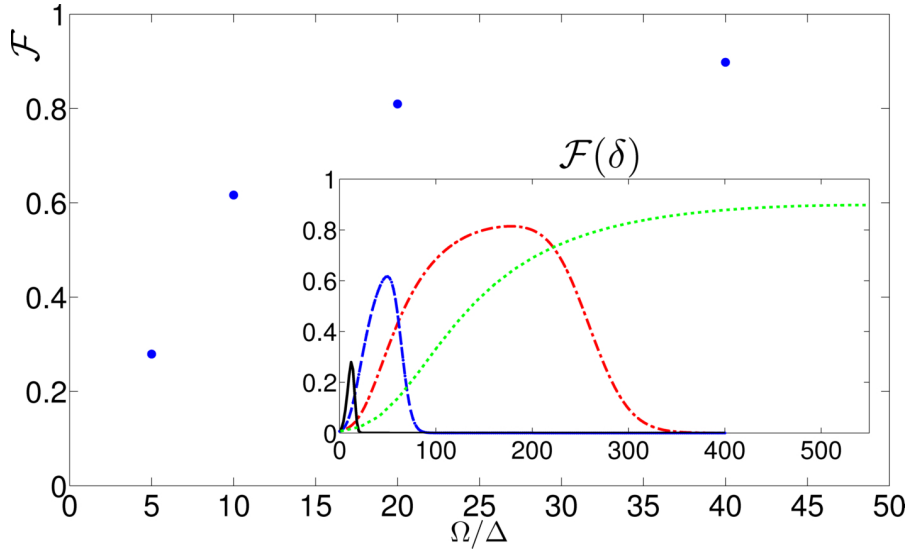

Figure 3.5: (Color online). Maximized fidelity $\mathcal{F}$ of regaining the excitation initially stored in the state $|\psi_+\rangle$ after $\tau = 10$ cavity lifetimes, as a function of Ω/Δ. We took $\Delta = 1$ MHz, $\kappa = 0.1$ MHz, $\gamma = 10^{-4}$ MHz. Inset : same quantity $\mathcal{L}$ as a function of detuning δ, after τ. Green dotted line : $\Omega = 40$ MHz ; Black solid line : $\Omega = 20$ MHz; Blue dashed line : $\Omega = 10$ MHz; Red dotted line : $\Omega = 5$ MHz.

is a severe drawback for quantum computation on chip. Here we suggest an experiment to prepare and exploit this dark state as a quantum memory, in the case where the discrete emitters are replaced by broad assemblies of atoms. This proposal allows to benefit from the collective atoms-cavity coupling, while the storage time now corresponds to the dephasing time of individual emitters, and is thus potentially quite long.

First we have checked the validity of the effective model if two ensembles are coupled to the cavity. We have plotted in fig.3.6a the exact transmission $|t(\omega)|^2$ of a cavity coupled to two Gaussian ensembles and verified that the position of the peaks are fitted by the eigenenergies computed in the discrete case. Moreover, we have superimposed the transmission resulting from the exact calculation and from the discrete model, as it can be seen in fig.3.6b after focusing on the central peak of the transmission pattern: the excellent agreement between the two plots fully validates the effective approach. This central peak corresponds

to the eigenstate $|\psi_d\rangle$ resulting from the coupling between the cavity mode and the antisymmetric state $|\mathcal{A}\rangle = (|G_1, S_2\rangle - |S_1, G_2\rangle)/\sqrt{2}$, its expression being $|\psi_d\rangle = (i\delta\,|1, G_1, G_2\rangle + \Omega\sqrt{2}\,|0, \mathcal{A}\rangle)/\sqrt{\delta^2 + 2\Omega^2}$. When $\delta \gg \Omega$, the excitation is mostly in the cavity, and mostly in the matter field in the opposite case. This change of nature clearly appears in the narrowing of the peak while lowering δ, as it can be seen in the figure, and confirmed by the expression for its linewidth $\Gamma_d = (\delta^2\kappa + 2\Omega^2\gamma)/(\delta^2 + 2\Omega^2)$. Note that this modelling might explain some recent experimental results [59], in which a superconducting cavity is strongly coupled to a inhomogeneous ensemble of NV centers of spin 1. Because of the geometrical strain, the transitions $|m_S = 0\rangle \rightarrow |m_S = 1\rangle$ and $|m_S = 0\rangle \rightarrow |m_S = -1\rangle$ are splitted, which can be modeled by two ensembles of emitters of different central frequencies. The visible presence of a narrow peak at the cavity frequency explains qualitatively the effect discussed above.

Coming back to the general case of two distinct ensembles, the state $|\psi_d\rangle$ could provide a new type of quantum memory as mentioned in the beginning of this Section. The protocol consists in feeding the cavity mode with a single photon while the ensembles are largely detuned, thus preparing the state $|1, G_1, G_2\rangle$, then adiabatically transferring the excitation to $|\psi_d\rangle$ by slowly lowering δ. Yet the ensembles cannot be brought to resonance with the mode as it would be the case for two discrete emitters. As it appears in fig.3.6c, the effective model breaks down when $\delta \sim \Delta$. At this point indeed, the distributions of emitters start to spectrally overlap with the central peak, leading to its broadening. This yields a minimal linewidth $\Gamma_d \sim \gamma + (\Delta^2/2\Omega^2)\kappa$, allowing to typically reduce the cavity losses by $(\Omega/\Delta)^2$. Here again the ratio $(\Omega/\Delta)^2$ appears as a major figure of merit for devices based on inhomogeneous ensembles strongly coupled to cavities.

3.6 Summary

We have shown that if an inhomogeneous distribution of emitters is strongly coupled to a cavity, the ensemble can be treated as a single effective emitter collectively coupled to the mode, whose relaxation is governed by single emitter's properties, provided that their spectral distribution decreases faster than $1/\omega^2$. This effect called "cavity protection" offers promising perspectives in the

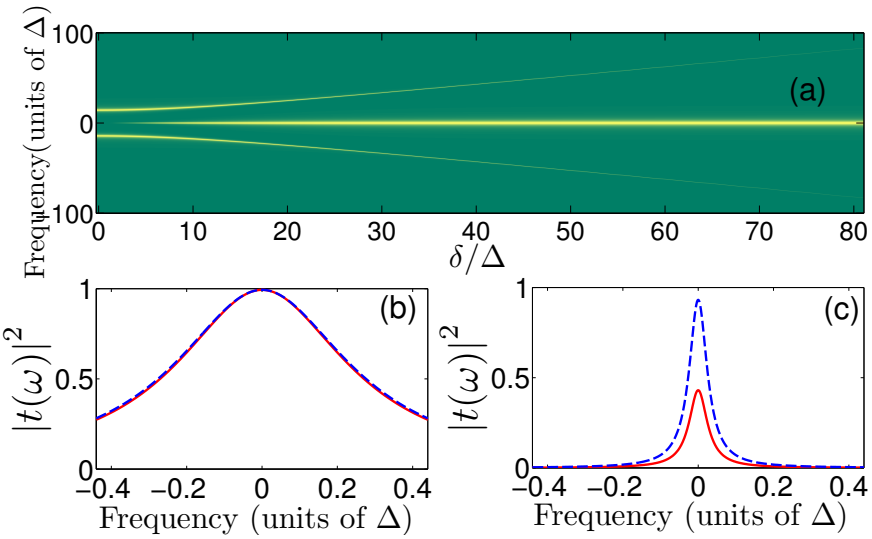

Figure 3.6: (Color online). (a) : Transmission of a cavity coupled to two Gaussian distributions of emitters, each detuned by $+\delta$ and $-\delta$ from the cavity frequency, δ is swept from 0 to 8 MHz. We took $\Omega = 1$MHz, $\Delta = 0.1$MHz, $\kappa = 0.5$MHz, $\gamma = 10^{-4}$MHz. (b) : Focus on the central peak with $\delta = 0.5$ MHz. Solid red line : Gaussian profile. Blue dashed line : two emitters of homogeneous linewidth γ. (c) : $\delta = 0.15$ MHz.

framework of quantum information with solid state integrable devices, in particular regarding the implementation of long lived high fidelity quantum memories. These results are quite general, and can fruitfully be applied to numerous important physical systems, ranging from semiconductor emitters coupled to optical cavities, to ensembles of spins in circuit QED. That is precisely our goal in the next Chapter, where we employ the model developed so far, with some minor modifications, to analyze a set of experimental data. The experimental work, performed by the Quantronics group of CEA Saclay, is one of the first to achieve strong coupling between a superconducting resonator to a Nitrogen-Vacancy spin ensemble.

Chapter 4

Hybrid circuits

In this chapter we report on the theoretical analysis of some of the first proof-of-concept experiments on hybrid quantum circuits. Hybrid circuits are devices that combine different physical systems in a way as to profit from complementary strengths and minimize the weaknesses. They are not an exclusivity of quantum circuits, in fact classical computers have been using hybrid circuits for a long time. For instance, electronic circuits that allow for fast processing are put together with magnetic hard-drives that provide high-volume information storage. It appears that the manipulation of quantum information could benefit from analogous ideas.

One of the goals of quantum hybrid circuits is to associate a macroscopic system, such as a superconducting qubit, which exhibits good scalability, tunability, and large coupling allowing for efficient readout and logical gate implementation, but have relatively short coherence(10μ s) times with microscopic systems. Microscopic systems (a trapped atom or spin for instance) on the other hand, have long coherence times (ms or even s) and can be identical to one another, but operate slowly due to their small couplings, and have limited scalability. The challenge, pursued at the moment by various groups, is to combine these different systems only inheriting the advantages of each one [58, 72]. Clearly many hybrids are possible. Apart from the different superconducting qubits available, we have a myriad of microscopical systems: from atoms trapped in optical lattices, Rydberg atoms and ions to spins in atomic clouds or in solids or even mechanical oscillators.

In this chapter we model an experiment coupling a transmon SQ to a nitrogen-vacancy(NV) spin ensemble mediated by the microwave coplanar resonator that we described in Section 2.3. The resonator can be spectrally tuned to interact with the spins or the qubit acting as a quantum bus. The NV centers provide a very versatile platform to process quantum information as the electronic spin can interact both with microwave and optical fields possibly working as a light-matter interface [73]. The electronic spin has a very long coherence time(ms) when isolated even at room temperature [74]. In addition the nitrogen nuclear spin could be exploited to obtain even longer coherence if one transfers quantum information from electron spins by using hyperfine interaction [75]. The microwave transition in the NV center matches well the typical qubit transitions with a ground state zero-field-splitting of 2.88 GHz.

In order to implement this hybrid circuit using the resonator bus, one has to implement a strong coupling between the resonator and both the superconducting qubit and the spin ensemble. Several experiments have demonstrated strong coupling between superconducting qubits and resonators [76, 20]. On the other hand, similar experiments on spin ensembles have not been implemented until recently and this was the first experimental challenge to be faced. Two independent groups have pioneered the strong coupling between an ensemble of spins and a resonator [59, 60]. Both placed a diamond crystal with spins from defects on diamond lattice, the crystal was placed at the position of maximum magnetic field of the resonator. The resonator was probed spectroscopically yielding a Rabi splitting of several MHz, a clear signature of strong coupling.

After this breakthrough the next step towards implementing the hybrid circuit using the spin ensemble as a memory was to store and retrieve microwave photons in the spin ensemble. This has been achieved in [77] for a coherent state involving 500 photons. We discuss the modeling of this experiment in Section 4.2.

Having established the building blocks of the full hybrid circuit the next step was to integrate them on the same sample. Experiments reported in [78] are a first proof-of-concept of a hybrid circuit with spin-ensemble based quantum memory for a superconducting qubit. In this experiment Kubo *et al* prepared arbitrary superpositions of the qubit states that were stored into collective excitations of the spin ensemble and retrieved back into the qubit. The quantum coherence of

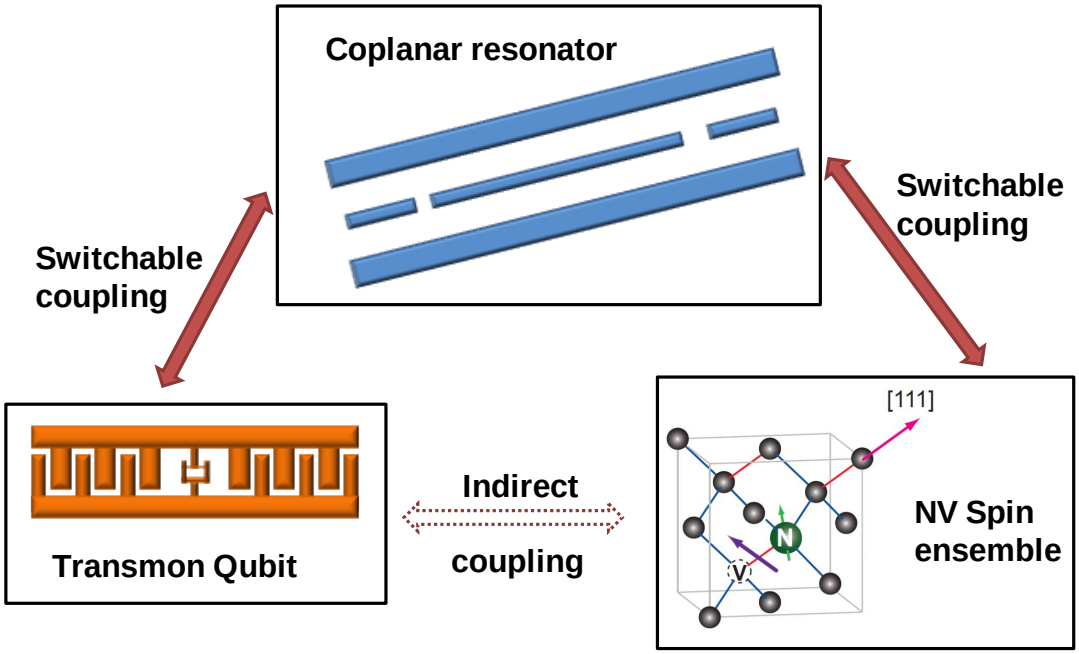

Figure 4.1: Schematic diagram showing how the building blocks of a hybrid circuit. The qubit and the dipole transition on the NV center are detuned allowing the resonator to interact selectively with either the qubit and the spin ensemble (as the resonator is tunable in frequency). Switching off the interaction is achieved when a large detuning is imposed between resonator an each of the other elements. SQ and spins couple only indirectly via the resonator acting as a quantum data bus.

the process was demonstrated by performing quantum state tomography of the qubit. We discuss the modeling of this experiment in Section 4.3.

These experiments take quantum circuits to a point where novel quantum technologies can emerge, one such new possibility has been explored in [79] where the same hybrid circuit was used to realize a new type of high-sensitivity low-temperature electron-spin-resonance (ESR) spectrometer. This set of experiments revealing the hyperfine structure of the NV centers is modeled in Section 4.4.

4.1 General setup and experimental techniques

In this section we present in more detail the properties of all the elements composing the circuit sketched in Fig. 4.1. This circuit is experimentally realized as shown in Fig. 4.2 and is roughly the same for the experiments in [77, 78, 79].

The main difference between [77] and [78, 79] is the addition of the transmon qubit. The scheme in Fig. 4.2 is the full setup, i.e. the setup in [77] does not contain the elements in the dashed box.

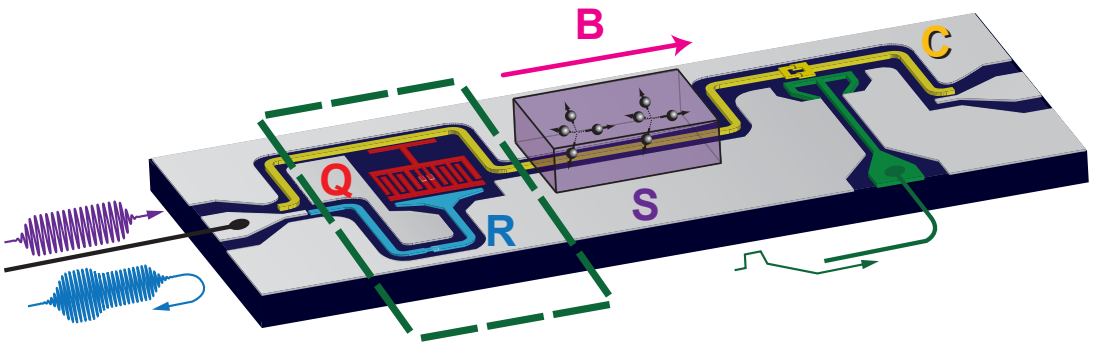

Figure 4.2: Sketch of the implementation of the transmon-NV hybrid circuit. The spin ensemble S consists of NV centers in a diamond crystal. They are coupled to the frequency-tunable waveguide resonator C which embeds the qubit Q. The qubit state can be readout with another resonator R. Microwave pulses for spin spectroscopy as well as for qubit readout are sent via an input port coupled both to C and to R. The qubit and its readout resonator is enclosed in the dashed box. The main difference between [78] and [77] is the addition of the transmon qubit, i.e. the setup in [77] does not contain the dashed box. Adapted from [78].

4.1.1 NV centers

NV centers have recently been used and proposed for a number of applications such as quantum computers, quantum cryptography and communication [80, 81], vectorial magnetic sensors [81, 82] spin-photon entanglement, and coupling them to a wide variety of interesting systems to achieve scalability [83, 84]. The NV

center arises when a vacant lattice site has a nitrogen atom as one of its nearest-neighbors in the diamond lattice. This point defect can be either the neutral NV^0 [85] or the negatively-charged NV^- center (commonly referred to as the NV center). The NV^- has attracted more attention as it has a spin-one ground state [86] with zero-field splitting and long spin-coherence time. It is composed of six electrons, three electrons come from the dangling bonds connecting the vacant site with the three nearest-neighbor C atoms, two come from the nitrogen-atomŠs dangling bond, and the other electron is captured from a donor. This point defect has a rather complex level structure and there is still debate on topics such as the ordering of the dark intermediate singlet states [87]. In this thesis we will model experiments made with microwave irradiation of the NV centers, this will allow us to restrict ourselves to the electronic ground state as the electronic transition are in the optical range.

The use of spin resonance techniques has shown that the ground state is a triplet [88, 86]. The ground state properties can be successfully described by a molecular model for the six electrons [89, 90]. The four lowest energy molecular orbitals are represented in Fig. 4.3 and if we fill the molecular orbitals from lowest to highest energy following HundŠs rules we find that the ground state has 2 unpaired electrons (these electrons originate the spin 1 observed experimentally). The ground state spin triplet couples to the ^{14}N nuclear spin I = 1 [1] yielding the hyperfine coupling Hamiltonian [2]

$$\begin{cases} H_S = DS_z^2 + E(S_x^2 - S_y^2) + \gamma_{NV}\vec{B}.\vec{S} \\ H_{SI} = A_{\parallel}S_zI_z + A_{\perp}(S_xI_X + S_yI_y) \\ H_I = PI_z^2 + \gamma_N\vec{B}.\vec{I}\,. \end{cases} \tag{4.1}$$

$P = -5$MHz is the ^{14}N quadrupole splitting and $\gamma_{NV} \equiv g_S\mu_B = 2.8$MHz G^{-1} ($\gamma_N \equiv -g_I\mu_N$) is the gyromagnetic ratio for the NV center spin (^{14}N nuclear spin) . $D = 2.88$GHz is the electronic zero-field splitting [86], responsible for energy splitting between the $|m_s = 0\rangle$ and $|m_s = \pm 1\rangle$ levels. The constant E is controlled

[1] In natural abundance, nitrogen is composed of 99.6% of ^{14}N, with spin I = 1, and 0.4% of ^{15}N, with spin I = 1/2. Throughout this thesis we shall neglect the presence of ^{15}N.

[2] In this chapter we call Hamiltonian and operator which is in fact the standard Hamiltonian divided by $\hbar$. This is convenient because all observable are frequencies.

by local strain felt by the defect and can vary considerably between different sample preparation techniques and even from one defect to another in the same sample. Typical values for E are in the range of MHz [91]. This local strain is one of the reasons why ensembles of NV centers display inhomogeneous broadening. $A_{\parallel} = -2.1$MHz and $A_{\perp} = -2.7$MHz are, respectively, the axial and transverse hyperfine constants [92, 93]. They cause a splitting of $A_{hs}^{N} = -2.16$MHz between transition frequencies for different I_z projections as indicated in Fig. 4.3.

In the presence of an applied magnetic field $\vec{B}$, the $|m_s = \pm 1\rangle$ levels split, revealing resonances separated by $2g_S\mu_B B$, where we suppose that the symmetry axis of this particular NV center is parallel to the magnetic field. For ensembles, there are four different NV orientations(see Fig. 4.3) and clearly the angle between the magnetic field and each of the four orientations is, in general, not the same. Provided that $g_S\mu_B|B| \ll D$, only the projection of the magnetic field on the NV axis affects the transition frequencies. This happens because the terms proportional S_x or S_y are spin flips, but the spins are separated by a gap $\hbar D$ which inhibits any spin flip as long as $g_S\mu_B|B| \ll D$. So in total there will be 24 transitions which are eight shifted copies of the triplet spectrum, cf Fig. 4.3 . For special magnetic field orientations (i.e. along the [100] crystal orientation), $\vec{B}.\vec{S}$ is the same for all four NV orientations, producing only six resonances.

The existence of optical transitions is a strong attribute of these point defects. They allow, for instance, optical spin polarization and spin-dependent fluorescence. These features translate into the possibility to access, initialize and readout a spin qubit optically [90, 94].

The last electron forming the NV^- center comes from nitrogen substitutional [95], i.e. nitrogen that substituted a carbon atom in the diamond lattice. However this defect has an electron spin which works as a spin bath inducing decoherence [96] to the spins. Furthermore this limits the conversion rate from nitrogen to NV centers in a diamond, at least with convention fabrication techniques, as less than half of the nitrogen atoms that enter the lattice can capture an electron to form a NV^- center.

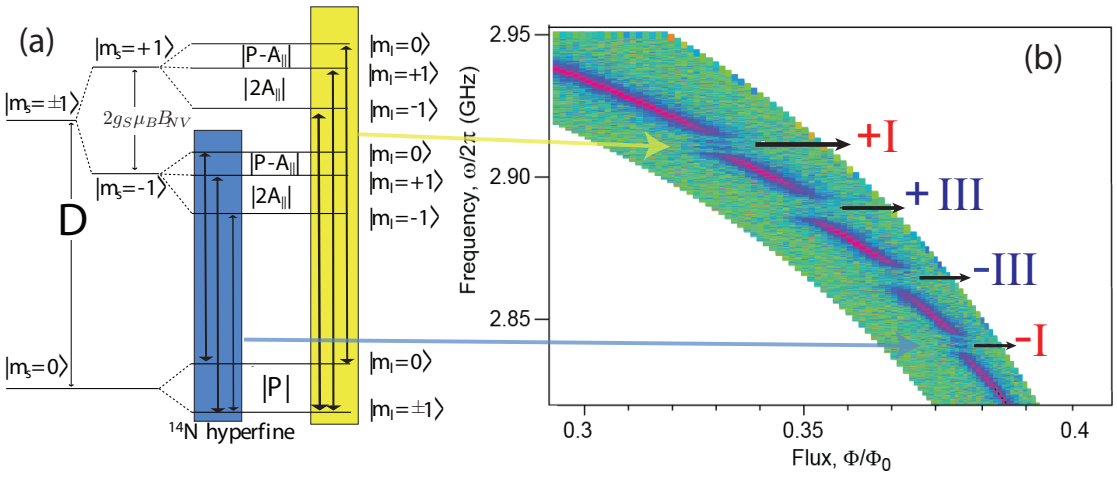

Figure 4.3: (a) Ground state level hyperfine structure of the NV center coupled to its ^{14}N spin under a small external field. Magnetic dipole transitions are shown with double-headed arrows. The strain constant E is taken to be zero. (b) Adapted from [78]. Two-dimensional plot of the transmission in energy through a resonator coupled to an ensemble of NV centers. On the y-axis we have the drive frequency, on the x-axis we have the flux of magnetic field used to tune the resonator (in this range the flux is roughly proportional to the resonator bare frequency). Color scale goes from -55 dB (green) to -30 dB (magenta). A magnetic field of intensity $B_{NV} = 1.1$mT (mistakenly report as $B_{NV} = 1.4$mT in [78]) is applied to the spins parallel to the [1, 1, 1] crystallographic axis. In this case there are only two different angles between the magnetic field and the different NV orientations, this originates 12 microwave transitions on the spins (see text). Each two of the four anticrossings correspond to the one of two distinct families of NV centers, being either along the [1, 1, 1] crystal direction parallel to or along one of the three other possible <1,1,1> axes. The yellow and blue arrows between the two figures relate the level structure with the associated anticrossing. Instead of a simple doublet as the one we found in Chapter 3 it is possible to distinguish several peaks in each anticrossing: a clear indicative of the hyperfine coupling. (To fix: dashes on the fig)

4.1.2 Transmon qubit readout

The qubit readout relies on the nonlinearity of the readout resonator R operated in the so-called JBA (Josephson Bifurcation Amplifier) mode. It behaves as a sample-and-hold detector, i.e. the first pulse maps different qubit states into different photonic states of the resonator that is then readout. It is based on the dispersive version of the qubit-resonator interaction Hamiltonian 2.34

$$H = \hbar(\omega_{res} + \chi\sigma_z)b^\dagger b + \hbar\Omega_z\sigma_z\,, \tag{4.2}$$

where $\chi = g^2/\delta$ is typically in the MHz range. This Hamiltonian is obtained when the detuning δ between resonator and qubit is much larger than their coupling g. The resonator is then shifted by an amount which is a function of the qubit state. To measure the qubit state one needs to detect this frequency change before the qubit relaxes by spontaneous emission. This can be done by sending a microwave pulse close to the resonance frequency and measuring the phase of the transmitted signal [19]. However, the noise imposed by the amplification apparatus limits the efficiency of this method. A first step of amplification can be made on-chip using a non-linear resonator which owns its non-linearity also to a Josephson junction [97, 98]. This non-linear resonator has two metastable oscillation states, if pumped at a particular frequency. When the drive current is increased the system becomes metastable with two possible dynamical states with different oscillation amplitudes, i.e. two possible photon populations. But the qubit interaction can shift the resonator so that the bistability curves will shift as a whole. We can then choose a driving power sufficient to switch the resonator when the qubit is in one state but that is not sufficient when it is in the other state. The dynamical states of the resonator will differ both in amplitude and phase depending on the qubit state. The switching is strongly hysteretic and once a switching event has occurred one can decrease the drive power and maintain while the state of the resonator is readout by a second pulse. This latching property conserves the information about the qubit state acquired during a small time interval in the resonator, so after the latching the measurement is not affected by the qubit relaxation anymore. This switching is easily detected by measuring the phase of the reflected readout pulse. Repeating the same sequence

then yields the resonator switching probability for a given readout pulse power. This allows to reconstruct response curves which change from 0 to 1 in a narrow power range close to bistability, see Fig. 4.4 .

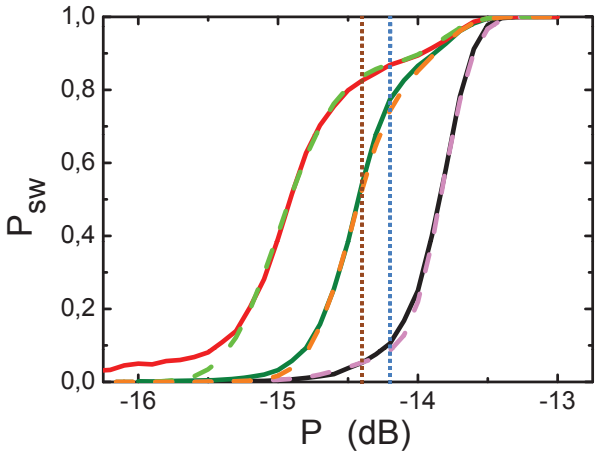

Figure 4.4: Readout resonator switching probability P_{sw} as a function of readout pulse power P_R. Black solid line: qubit in thermal equilibrium. Olive solid line: qubit prepared in $|e\rangle$. Red solid line: qubit prepared in $|f\rangle$, the second excited state of the transmon. This third level is used in composite readout pulses where the transmon is taken from $|e\rangle$ to $|f\rangle$ before readout to increase the contrast. Dotted blue vertical line indicates the readout power used for simple readout pulses, dotted brown vertical line indicates the readout power used for the composite readout pulse method. Adapted from [78].

4.2 Storage and retrieval of a microwave field

In this Section we analyze the first storage and retrieval cycle of microwave photons between a NV-center spin ensemble and a superconducting resonator. The experiment is well describe by the model of Chapter 3 where we showed that to first approximation the interaction between the electromagnetic field in the resonator and the spin ensemble involves only one collective variable, which behaves as a harmonic oscillator in the limit of low excitation energy [62]. When two such coupled harmonic oscillators are put into resonance, they coherently exchange energy with a period π/Ω where Ω is the collective coupling constant,

i.e. a classical Rabi oscillation. This dynamics is observed by measuring the amplitude of the microwave field leaking out of the resonator after its interaction with the spins, which is found to oscillate as a function of the interaction time. The large inhomogeneous broadening is the main limitation to the number of energy exchange cycles that can be observed, thus the situation described in Chapter 3 corresponds ideally to this system. From the theoretical point of view, the biggest difficulty is to obtain quantitative agreement for a set of data covering spectroscopic as well as different time-domain measurements.

4.2.1 Transmission Spectroscopy

The experimental setup is the one described in Section 4.1. Additional details on the diamond fabrication as well as the superconducting circuit can be found on [78] .The magnetic field $\vec{B}$ ($|B| = 1.7$ mT)used to Zeeman shift the NV center transitions is applied along the $[1, 0, 0]$ crystal axis. This orientation is useful because all the four NV center orientations make the same angle with $\vec{B}$ and, as discussed in Section 4.1.1, we will have only two spin transition frequencies in the electronic ground state(apart from hyperfine transitions and inhomogeneous broadening). This way a maximal number of spins do contribute to a large collective coupling. On the other hand this can have a negative impact of the observed linewidth as a small misalignment of $\vec{B}$ will yield different shifts for each NV direction.

In Chapter 3 we developed a single excitation theory while the experiment discussed in this Section is realized with ~ 500 excitations. Nevertheless as long as we can faithfully describe the system as a set of coupled harmonic oscillators (i.e. the number of excitations is small compared to $N \sim 10^{12}$) the dynamical equations do not depend on the number of excitations. To see this consider that we inject a coherent field of amplitude $\bar{c}_{in}$

$$\hat{c}_{in}(t) = e^{-i\omega t}[\langle c_{in}\rangle + \hat{\xi}(t)] \,, \tag{4.3}$$

where $\hat{\xi}(t)$ is responsible for the quantum fluctuations averaging to zero. Now if

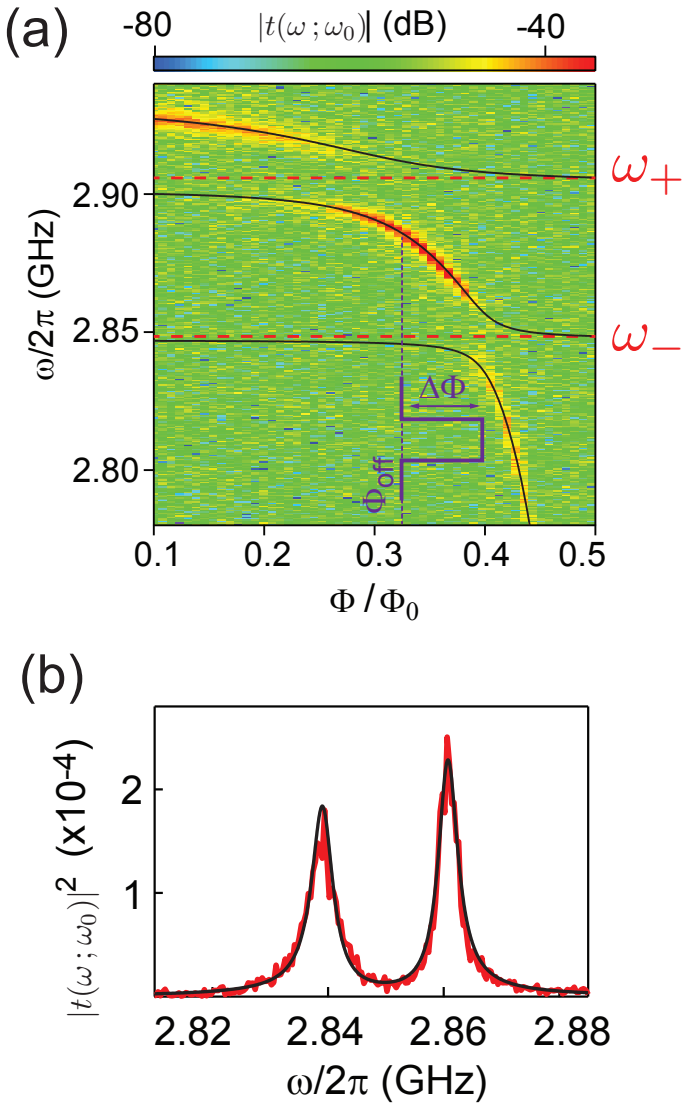

Figure 4.5: (a) Resonator transmission $|t(\omega, \omega_{res})|$ as a function of the drive frequency ω and of the flux (in units of the superconducting flux quantum $\Phi_0 = h/2e$) to tune the resonator bare frequency ω_{res} as described in Section 2.3.1. Two vacuum Rabi splittings are observed corresponding to the ω_- and ω_+ spin transitions . (c) Transmission in energy for a fixed resonator frequency close to resonance with ω_-. Red line is experimental data, black line is theory (rescaled in amplitude to fit the data). The spin density distribution found to agree with the experiments is a convolution of a Gaussian ($\sigma/2\pi = 5.12$ MHz) and a Lorentzian($\gamma/2\pi = 1.0$ MHz) distributions. The collective coupling is $\Omega/2\pi = 10.6$ MHz and the spins-resonator detuning is 0.5 MHz .

we insert this field in the set of input-output equations Eq. (3.3) we get

$$\begin{aligned}\frac{d\,\langle a(t)\rangle}{dt} &= -\left(\kappa/2 + i\omega_{res}\right)\langle a(t)\rangle + \sum_k g_k \langle b_k(t)\rangle - \sqrt{k/2}\,\langle c_{in}\rangle\ ,\\ \frac{d\,\langle b_k(t)\rangle}{dt} &= -\left(\gamma/2 + i\omega_k\right)\langle b_k(t)\rangle - g_k\,\langle a(t)\rangle\ .\end{aligned} \tag{4.4}$$

We can then see that this set of equations is formally identical to Eq. (A.1) and we can thus use the result obtained in Chapter 3. The first experiment modeled is a transmission spectroscopy Fig. 4.5. Quantitative predictions for this and the other experiments require to know not only the overall linewidth but also the detailed shape of the spins distribution $\rho(\omega)$. In particular Gaussian and Lorentzian distributions yield very different results. In NV centers ensembles, the inhomogeneous linewidth is caused by dipolar interactions with neighboring spins, either paramagnetic $P1$ centers that were not converted into NV centers during the sample processing, or ^{13}C nuclei which will be discussed in detail in Section 4.4.2. Neighboring NV centers do not contribute to the inhomogeneous linewidth because at the temperature of our experiment they are almost always frozen in the $m_S = 0$ state. Spin ensembles inhomogeneously broadened by dipolar interactions are expected to show a Lorentzian lineshape [54] with a cutoff; however we have complications in the experiment such as hyperfine coupling or misalignment of $\vec{B}$. As a result, we assume a phenomenological lineshape for our spin ensemble as a convolution of a normalized Gaussian of standard deviation σ with a normalized Lorentzian of HWHM γ. The resulting distribution is known as the Voigt profile and is also normalized

$$\begin{aligned}\rho(\omega';\sigma,\gamma) &= \int_{-\infty}^{\infty} G(\omega'';\sigma)L(\omega'-\omega'';\gamma)d\omega'\\ &= \frac{1}{\sigma\sqrt{2\pi}}\frac{\gamma}{\pi}\int_{-\infty}^{\infty}\frac{e^{\omega''^2/2\sigma^2}}{(\omega'-\omega'')^2+\gamma^2}\,d\omega'\ .\end{aligned} \tag{4.5}$$

An important property is that we can compute analytically the function $W(\omega)$ defined in 3.6:

$$W(\omega;\sigma,\gamma,\gamma_0) = \frac{\Omega^2}{\sigma\sqrt{2\pi}}\frac{\gamma}{\pi}\int\int\frac{e^{\omega''^2/2\sigma^2}}{(\omega'-\omega'')^2+\gamma^2}\frac{d\omega' d\omega''}{\omega-\omega'+i\gamma_0}\ . \tag{4.6}$$

We take the limit $\gamma_0 \to 0$, the decay of a single spin can be neglected in the time-scale $< 1\mu s$ compared to the $T_1 > 1$s expected for an NV spin

$$W(\omega;\sigma,\gamma) = -i\sqrt{\frac{\pi}{2}}\,\frac{\Omega^2}{\sigma}\,\exp\left\{-\left(\frac{\omega+i\gamma}{\sigma\sqrt{2}}\right)^2\right\}\mathrm{erfc}\left(-i\frac{\omega+i\gamma}{\sigma\sqrt{2}}\right)\,. \tag{4.7}$$

The function that is pictured in the theory plots takes into account the well-known NV center hyperfine splitting due to ^{14}N by adding up three identical distributions $\rho(\omega)$ separated by 2.2 MHz [99]. This is conveniently done since $W[\rho_1+\rho_2] = W[\rho_1]+W[\rho_2]$ for any two different spin distributions $\rho_{1,2}$. Using this formula for $W(\omega)$ we can evaluate the functions t_i necessary for the simulation of the time-domain experiments and that gives directly the transmission as plotted in Fig. 4.5 (b). The parameters are then optimized simultaneously for transmission spectroscopy in Fig. 4.5 and time-domain experiments in Fig. 4.6 and Fig. 4.8.

4.2.2 Rabi oscillations

The first time-dependent experiment is the resonant microwave field exchange on the resonator-spins. The resonant exchange is shown on Fig. 4.6 while the dependence with the resonator-spins detuned is explored in Fig. 4.7. The experimental sequence is sketched in Fig. 4.6 (a), first the resonator is populated at a time before $t = 0$ while it is kept out of resonance ($\Delta\omega/2\pi = 30$ MHz) by a microwave drive. At time $t = 0$ the resonator is abruptly tuned to resonance with the spins and they are left to interact for a time τ. When $t = \tau$ the resonator is once again taken out of resonance and the field it contains is measured as it leaks to the amplification chain and detection. After the $t = \tau$ the only evolution of the field is an exponential decay $|a(t > \tau)| = |a(\tau)|exp[-(t-\tau)/2T_{cav}]$. Measuring the amplitude of the exponentially damped microwave signal that leaks out of the cavity therefore directly yields $|a(\tau)|$. This sequence is repeated typically 5.10^5 times. The amplitude of the detected field in time t is plotted in 4.6 (b) as a function of the interaction time τ. The quantity of interest $|a(\tau)|$ is extracted by averaging $A(\tau,t)$ around $A(\tau,\tau+140ns)$. Such an average is show in 4.6 (c) where we can clearly see the storage-retrieval cycles at a time scale t_{Rabi} 50 ns compatible with the collective coupling extracted by the spectroscopy experiment

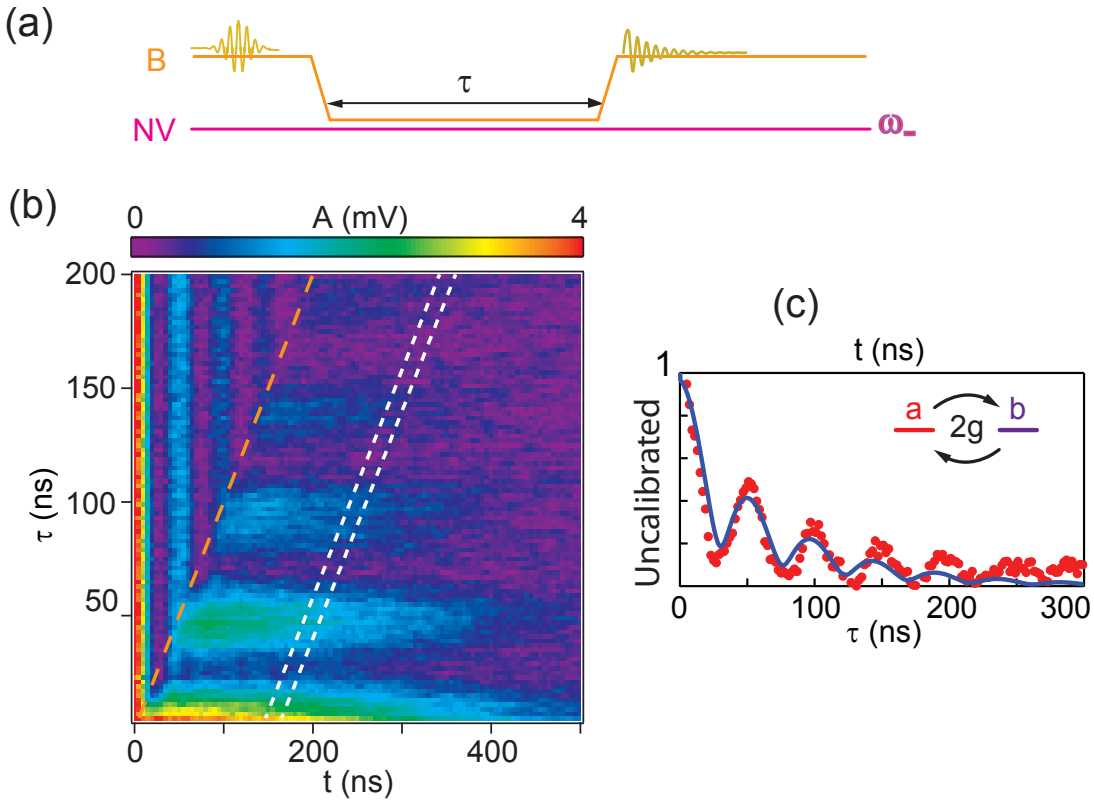

Figure 4.6: Rabi-like experiment. (a) Sketch of the pulse sequence. (b) The amplitude $A(\tau, t)$ of microwave pulses transmitted through the resonator is measured by homodyne detection at room temperature after amplification. (c) Normalized amplitude $a(\tau) = A(\tau, \tau \pm 140ns)$ evidencing the exchange of energy between resonator and a collective mode of the spin ensemble. Red dots are experimental data, blue is theory as explained in text. Adapted from [77].

and in agreement with the full theoretical simulation. As a direct proof of the influence of inhomogeneous broadening, the field amplitude decays to zero within a hundred of ns, a time scale not compatible with the spins T_1 s nor the cavity damping T_{cav} 100 ns. This type of decay is precisely the one we found in Section 3.4, and it can be seen as a coupling to a bath of dark states which act as an environment.

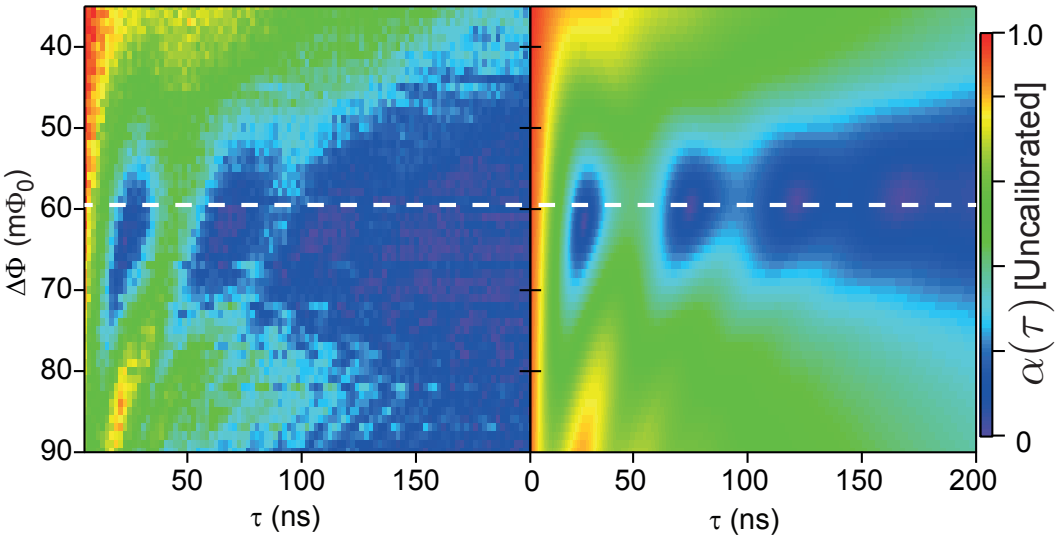

Figure 4.7: Coherent field exchange between the resonator and the spins for varying flux pulse amplitude. Normalized amplitude a$a(\tau) = A(\tau, \tau \pm 140ns)$is plotted as a function of resonator frequency tuned by the flux $\Delta\Phi$. Left graph is experimental data, right graph is theory. The white dashed line indicates the resonance condition as plotted in Fig. 4.6(c) .

In Fig. 4.7 the Rabi-like exchange is performed also out of resonance. As expected for two coupled oscillators. Out of resonance, the oscillations amplitude is reduced and their frequency slightly increases. The asymmetry with respect to the resonance frequency is caused by the nonlinear dependence of the bare resonator frequency with the flux and the fact that the resonator is always pumped with a positive detuning at time $t < 0$, and it is well reproduced by the theory. At around 65MHz we clearly see additional features not taken into account by the theory here. These are mainly due to spins having ^{13}C among their closest

neighbors, known to shift the electron spin frequency by this amount.

An additional complication for the simulation is that the resonator-spin detuning $\Delta\omega$ during the microwave pulse is finite. This means that instead of exciting a pure cavity state we excite a dressed state composed of cavity plus the superradiant spin state. To take this into account in the calculation, we make the approximation that this initial state is a coherent superposition of the excited resonator and excited superradiant spin mode. Indeed, introducing the vector $X(t)$ of coordinates $\left[\langle\hat{a}(t)\rangle, ..., \left\langle\hat{b}_j(t)\right\rangle, ...\right]$ and defining $x_G \equiv (1, 0, ...)$ and $x_S \equiv (0, g_1, ..., g_j, .., g_N)/\Omega$, the initial state is written

$$x(t=0) = \cos(\theta/2)x_G + i\sin(\theta/2)x_S\,, \tag{4.8}$$

with mixing angle $\tan\theta = 2\Omega/\Delta\omega$. As in Appendix A this definition is useful because $dX/dt = -(i/\hbar)H_{eff}X$ and the formal solution is readily obtained as

$$X(t) = \mathcal{L}^{-1}[(s + iH_{eff}/\hbar)^{-1}X(0)]\,. \tag{4.9}$$

The solution for the amplitude of the resonator is then proportional to

$$\alpha_{Rabi}(\tau) = \cos(\theta/2)\mathcal{L}^{-1}\left[t_1(s)\right] + i\sin(\theta/2)\mathcal{L}^{-1}\left[t_4(s)\right]\,. \tag{4.10}$$

Both $t_1(s) = x_G^\dagger(s + iH_{eff})^{-1}x_G$ and $t_4(s) = x_G^\dagger(s + iH_{eff})^{-1}x_S$ have been evaluated in Section A.1 to be $t_1(-i\omega) = i/\left[\omega - \omega_0 + i\kappa/2 - W(\omega)\right]$ and $t_4(-i\omega) = -it_1(-i\omega)W(\omega)/\Omega$. As we have already obtained $W(\omega)$ in Sexction A.2, computing $\alpha_{Rabi}(\tau)$ is thus achieved by numerically evaluating the inverse Laplace transform of t_1 and t_4.

4.2.3 Ramsey fringes

The last experiment of this set is a Ramsey-like experiment that gives direct information on the phase coherence of the stored microwave. The Ramsey sequence starts as before with a steady-state microwave field in the resonator which is kept out of resonance. The resonator is then brought to resonance for a time $\tau = \pi/2\Omega$ to implement a $\pi/2$ resonant pulse transferring about half of the energy to the

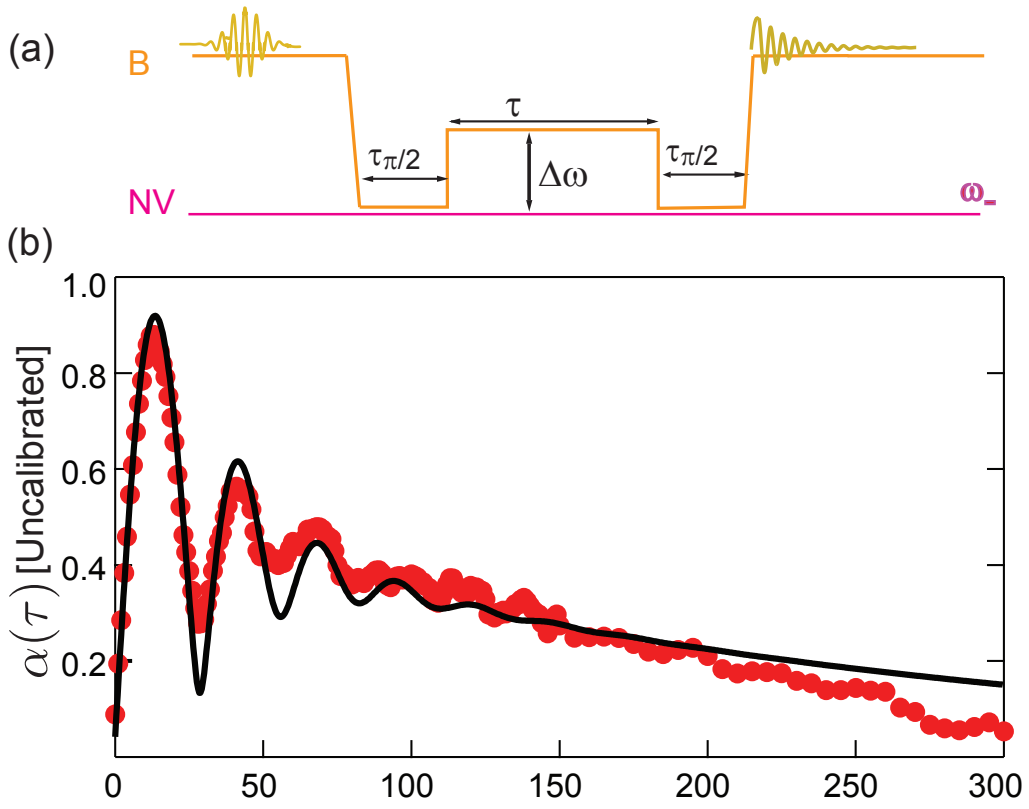

Figure 4.8: Ramsey-fringes-like experiment.(a) Sketch of the pulse sequence. (b) The normalized microwave amplitude $a(\Delta t)$ after the pulse sequence shown in the inset is plotted. Red dots are experimental data, the black continuous line is theory. The same parameters as on the previous simulations are used.

spin ensemble. The resonator is then detuned by $\Delta\omega/2\pi = 30$MHz by a flux pulse during a variable amount of time τ after which it is brought again to resonance for a second $\pi/2$ pulse and finally detuned so we can infer the resonator population at this stage.

The $\pi/2$ pulse corresponds to the transformation of the state x_G into the superposition $\frac{x_G - x_S}{\sqrt{2}}$. The state of the system after the first $\pi/2$ pulse and the off resonant interaction of duration τ can be evaluated using Eq. (4.9). We define $X_G(t)$ (resp. $X_S(t)$) as the vector of coordinates $[\langle a(t)\rangle, ..., \langle b_j(t)\rangle, ...]$ at time t with initial conditions x_G (resp. x_S). A second $\pi/2$ pulse is then applied before

the amplitude α_{RF} of the field in the resonator is measured :

$$\begin{aligned}\alpha_{RF} &= \frac{1}{\sqrt{2}} x_G^\dagger \cdot U_{\pi/2}(X_G(t) - X_S(t)) \\ &= \frac{1}{2}(x_G^\dagger + x_S^\dagger) \cdot (X_G(t) - X_S(t)) \\ &= \frac{1}{2}\mathcal{L}^{-1}(t_1(s) - t_2(s) + t_3(s) - t_4(s))\,,\end{aligned} \tag{4.11}$$

where $U_{\pi/2}$ is the evolution caused by the second $\pi/2$ pulse. Also $t_2(s) = {x_S}^\dagger \cdot (s + iH_{eff})^{-1} \cdot x_S$ and $t_3(s) = {x_S}^\dagger \cdot (s + iH_{eff})^{-1} \cdot x_G$ are evaluated in Section A.1 to be $t_2(-i\omega) = -t_1(-i\omega)W(\omega)(s + i\tilde{\omega}_0)/\Omega^2$ and $t_3 = -t_4$.

The beating between the effective spin oscillator and the resonator is observed in Fig. 4.8 at the frequency $\Delta\omega$. The theory curve also agrees fairly well. We can thus extract a single set of parameters $\sigma/2\pi = 5.12$ MHz, $\gamma/2\pi = 1.0$ MHz and collective coupling $\Omega/2\pi = 10.6$ MHz compatible with all three experiments.

4.3 Quantum memory implementation

In this Section we analyze the first experimental proof of concept of spin-ensemble based quantum memory. The sample used corresponds to the full circuit sketched in Fig. 4.2 . In addition to the elements of the sample of the previous Section, this sample has a superconducting transmon qubit with separate channels that allow for qubit state preparation and readout and a higher quality diamond crystal with less inhomogeneous broadening. Previous experiments of storage using an NV-spin ensemble were carried out in a 'classical' regime since the resonator and spin ensemble behaved as two coupled harmonic oscillators driven by large microwave fields. In the perspective of building a quantum memory, it is instead necessary to perform experiments at the level of a single quantum of excitation. The integration of the superconducting qubit on the same chip is what ultimately allows the exploration of this new regime. The experiment relies on the fact that we can transfer an arbitrary qubit state to the corresponding photonic state on the resonator, i.e. we can transform $(\alpha\,|g\rangle + \beta\,|e\rangle) \otimes |0\rangle_{res}$ into $|g\rangle \otimes (\alpha\,|0\rangle_{res} + \beta\,|1\rangle_{res})$. This SWAP gate could be performed by tuning ω_{res} into resonance with ω_{qubit} for a duration $\pi/2g_{qubit}$ in the same way that the experiment described in the previous

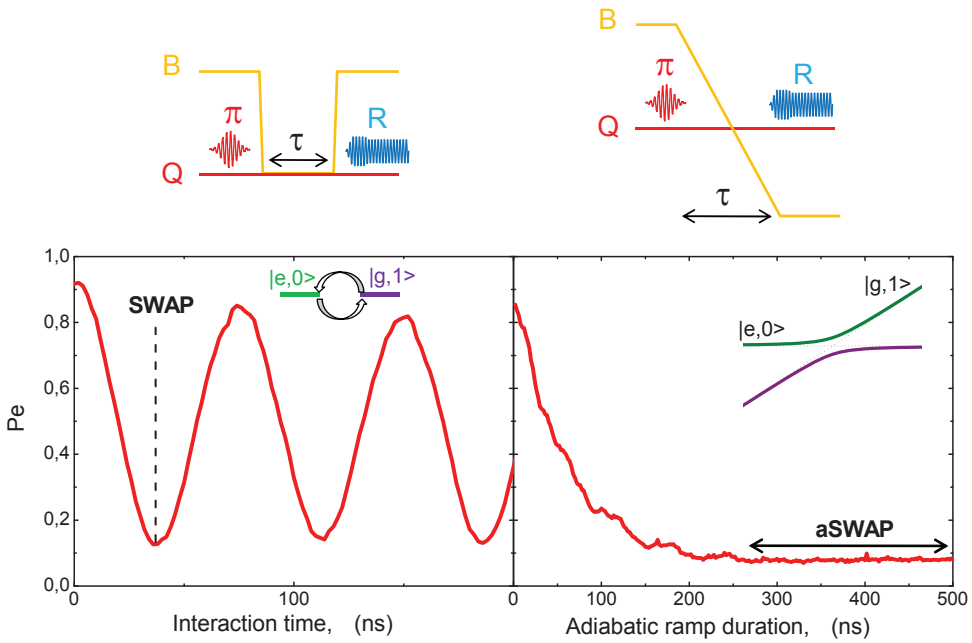

Figure 4.9: Comparison between resonant and adiabatic SWAP pulses. Left panel: principle of a resonant SWAP. After excitation of the qubit in $|e\rangle$, B is put suddenly into resonance with Q for an interaction time τ during which $|e,0\rangle$ and $|g,1\rangle$ exchange periodically energy. Right panel: principle of an adiabatic SWAP (aSWAP). The resonator is ramped through ω_{qubit} in a time τ, and the states of the resonator and qubit are swaped at the end of the pulse. For long enough ramp durations (in our case $\tau \gtrsim 300$ ns), the qubit excited state population is fully transferred into the bus. The pulse R represents the qubit readout that in this case works as an indirect readout of the resonator state. Note that one disadvantage of the aSWAP sequence is that a larger portion of the excitation can escape through the resonator.

Section transferred energy from the resonator to the spin ensemble. Instead Kubo *et al* prefered to adiabatically sweep ω_{res} across ω_{qubit} as this sequence is more immune to flux noise in the SQUID loop used to tune the resonator frequency as pictured in Fig. 4.9. In other words the flux noise translates into a fast noise in the resonator frequency which makes it difficult to maintain the resonance condition to within a few KHz as it is necessary to perform the resonant SWAP pulse. The adiabatic SWAP ($aSWAP$) achieves nevertheless the same quantum operation as the resonant SWAP except for an irrelevant dynamical phase. This way one can populate the resonator with single microwave photons and then proceed to store and retrieve this single excitation in the spins. As the interaction between qubit and spins is mediated by the resonator, we call it 'bus', shortened to B in the figures. Additionally the qubit works as a high efficiency detector for the resonator state. This can be done because, as discussed in Section 4.1.2, the qubit state can be read out with high efficiency and the $aSWAP$ pulse can be used to imprint the resonator state on the qubit.

The diamond sample consists of roughly the same density of NV defects as the one used in [77], of which 10^{12} are expected to couple to the resonator magnetic field. A static magnetic field is also used to lift the degeneracy between the $m_S = \pm 1$ states. This time, however, the direction of $\vec{B}$ is parallel to the $[1,1,1]$ crystal axis. Two groups of NVs thus experience different Zeeman shifts as this term is sensitive only to the projection of B along the $N-V$ axis. We denoted I the group along $[1,1,1]$ and III those along either of the three other $\langle 1,1,1\rangle$ axes as they are 3 times more numerous. As already shown in Fig. 4.3 this results in a total of 12 different transition frequencies and we group them in sets of three transitions separated by 2.2 MHz corresponding to the three ^{14}N nuclear spin projections denoted $\omega_{\pm I,\pm III}$. The advantage of this choice is that the group of spins along the $[1,1,1]$ direction do not suffer from additional inhomogeneous broadening caused by misalignment. This is because a small misalignment will generate the same shift for any spin in this direction.

The simulations in this Section follow the same scheme of the previous one. The differences are restricted to the fact that the phenomenological Gaussian convolution is no longer necessary and the spin densities can be taken to be Lorentzians and that here we are really dealing with single excitation, but as we

showed this has no large impact on the modeling.

4.3.1 Single photon storage

Instead of directly populating the resonator with a coherent field as in the previous experiment, this sequence starts with the preparation of the qubit in the state $|e\rangle$ by a π pulse that inverts the qubit. A first $aSWAP$ converts $|e\rangle$ into the bus Fock state $|1\rangle_{res}$; B is brought into or near to resonance with the spin ensemble for a duration τ; the resulting B state is then transferred back into the qubit, which is finally read-out. Fig. 4.10 (b) shows the resulting curve $P_e(\tau)$ when the bus is brought into resonance either with ω_{-III} or ω_{-I}. An oscillation in P_e is observed, revealing a storage in the spin ensemble of the single quantum of excitation initially in the qubit at $\tau_{s,III} = 65$ ns or $\tau_{s,I} = 97$ ns, and a retrieval back into the qubit at $\tau_{r,III} = 116$ ns or $\tau_{r,I} = 146$ ns. The fidelity of this storage-retrieval process, defined as $P_e(\tau_r)/P_e(0)$, is 0.14 for group III and 0.07 for group I. These relatively low values are not due to a short spin dephasing time, but rather to an interference effect caused by the HF structure of NV centers, as evidenced by the non-exponential damping observed in $P_e(\tau)$. The higher quality of the sample and the higher detection efficiency contribute to a very clean experiment that agrees to a high level of precision with the theory curves. The simulation takes into account the HF structure, with the linewidth of the three HF peaks as the adjustable parameter. A linewidth of 1.6 MHz is in this way determined for the spins in group I, and of 2.4 MHz for group III, this larger value being likely due to a residual misalignment of B_{NV} from the $[1,1,1]$ crystalline axis causing each of the three $< 1,1,1 > N-V$ orientations non-collinear with the field to experience slightly different Zeeman shifts. A misalignment of 0.02 rad would be enough to cause a broadening such as we observe. We also note that the best fit is achieved for the splitting of 2.3 MHz between the three peaks of the HF structure which is slightly larger than the value reported in most articles (2.18 MHz). We cannot, however, determine precisely whether this difference actually reflects a change in the HF interaction parameters of the NV center at low temperature. We find that $\Omega_I/2\pi = 2.9$ MHz and $\Omega_{III}/2\pi = 3.8$ MHz fit best our data, the difference in the coupling constants

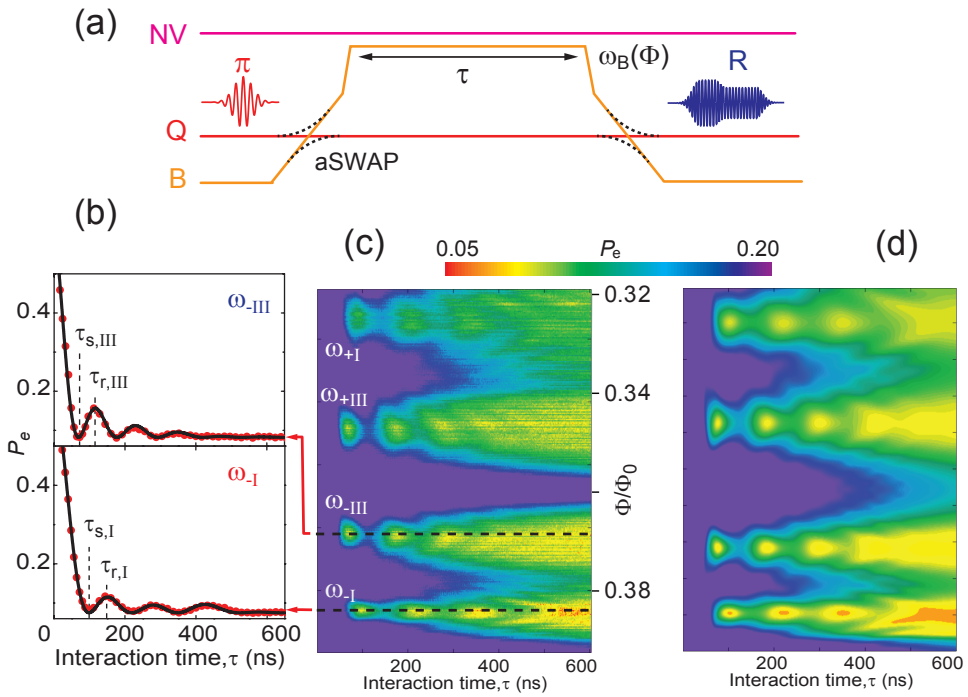

Figure 4.10: Storage and retrieval of a single quantum of excitation from the qubit to the spin ensemble. (a) Experimental sequence showing the microwave pulses used for exciting the qubit in $|e\rangle$ (red) and for reading it out (blue), as well as transition frequencies of the quantum bus (orange), qubit (red), and spins (magenta). (b) Experimental (red dots) and theoretical (black line) probability $P_e(\tau)$ for ω_{res} tuned to ω_{-III} (top graph) or ω_{-I} (bottom graph), showing the storage and retrieval times τ_s and τ_r. (c) Two-dimensional plot of P_e versus interaction time τ and flux pulse height Φ, showing resonance with the four spin groups. Chevron-like patterns are observed, showing a faster oscillation with reduced amplitude when ω_B is detuned from the spin resonance. Note that the difference between the ω_- and ω_+ patterns in the same NV group is simply caused by the non-linear dependence of ω_{res} on the flux Φ. (d) Simulation of P_e versus interaction time τ and flux pulse height reproducing all the main features.

can be explained by the larger number of type III spins and the fact that the magnetic field lines of the resonator do not make the same angle with the I and III N-V axis. We also note that in both curves shown in Fig. 4.10 (b) $P_e(\tau)$ tends towards 0.08 at long times which correspond to a thermal population of temperature ~ 50 mK.

4.3.2 Ramsey-fringes

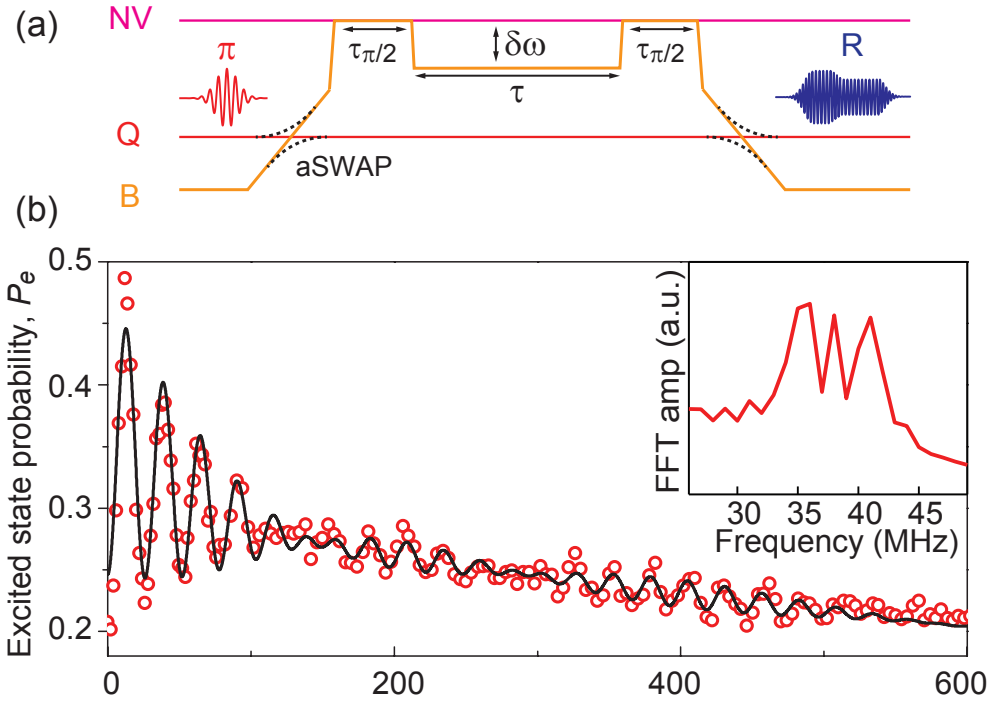

Figure 4.11: Ramsey-fringes-like experiment. The probability of finding the excited qubit used to detect the resonator state is plotted as a function the time τ between the $\pi/2$ pulses. Red dots are experimental data, the black continuous line is theory. The same parameters as on the previous simulations are used.

A single-photon Ramsey-fringes-like is performed to evaluate the quantum coherence of the stored in the ensemble, Fig. 4.11. A one photon Fock state is prepared in the same way as the Rabi-like experiment, after that the bus is tuned to ω_{-I} for a duration $\tau_{\pi/2} = \tau_{s,-I}/2$, ω_{res} is then suddenly detuned by

$\Delta\omega/2\pi = 38$ MHz for a time τ. At this point, the joint bus-spin ensemble state is an entangled state $\left(|1\rangle_{res}|G\rangle_{-I} + e^{i\varphi}|0\rangle_{res}|S\rangle_{-I}\right)/\sqrt{2}$ with a phase $\varphi = \Delta\omega\tau$. A second $\tau_{\pi/2}$ pulse converts the phase φ into population of $|1\rangle_{res}|G\rangle_{-I}$. This population is finally transferred to the qubit, and read-out. Oscillations at frequency $\Delta\omega$ are observed in $P_e(\tau)$ as seen in Fig. 4.11, confirming that the resonator and the spins are entangled after the first $\pi/2$ pulse. These oscillations are modulated by a beating pattern, with an overall damping of the oscillations envelope in $\sim$ 200 ns. Quite remarkably, this beating observed in the qubit excited state probability is directly caused by the HF structure of NV centers, as proved by the Fourier transform of $P_e(\tau)$ which shows three HF lines. The full calculation of the system dynamics quantitatively captures both the beatings and the oscillations damping, which is thus completely explained by the 1.6 MHz inhomogeneous linewidth of each HF line taken into account in the theory. In this sample the hyperfine structure is as important as the inhomogeneous broadening in limiting the storage time of quantum information in the NV centers ensemble. Note that unlike the inhomogeneous broadening, the hyperfine coupling to the nuclear spin of ^{14}N could be turned into a useful resource if quantum information was transferred from the electron spin to the nuclear spin degree of freedom, which has a much narrower linewidth. Finally refocusing techniques borrowed from quantum memories in the optical domain [100] should increase the storage time by two orders of magnitude.

4.4 Electron spin resonance spectroscopy

One of the goals of the development of hybrid circuits is to explore new phenomena that could eventually span novel quantum technologies. An example of such a novel technology is a high sensitivity electron spin (ESR) spectroscopy [101] that we describe in this Section. The sample is the same used in the experiment of the previous Section and the novelty consists in pumping directly the spins and measuring the signal with the superconducting qubit that acts as a single-microwave-photon detector, resulting in an enhanced sensitivity. With this setup Kubo *et al* measured the NV center absorption spectrum at 30 mK with no more than 15 spins excited at each time. The use of superconducting quantum

electronics in high sensitivity ESR spectroscopy allows to boost the sensitivity lost when measuring spins at millikelvin temperatures. These measurements have to be restricted to low powers to avoid saturation as the spins take a long time to relax. High Q resonators with cryogenic low noise amplifiers have been used in [102]. The hybrid circuit allows to go one step further and use the qubit as an on-chip single microwave photon detector.

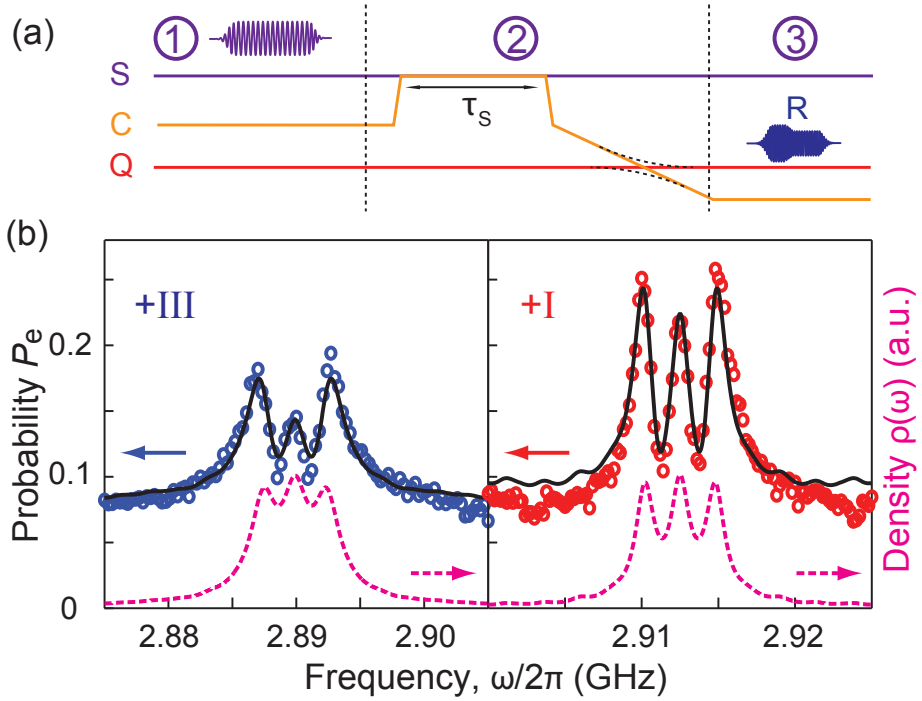

Figure 4.12: (a) Experimental pulse sequence used for qubit-detected ESR: (1) The spins are first weakly excited by a microwave pulse with a frequency ω_p; (2) the resulting spin excitation is transferred to the cavity C by a fast flux pulse which brings ω_{res} in resonance with ω_K ($K = +I, +III$) for a swap time $\tau_{s,K}$, and then to the qubit by an adiabatic swap ($aSWAP$). (3) The qubit excited state probability P_e is finally measured. (b) Measured (open circles) and calculated (solid line) $P_e(\omega_p)$ for spin ensemble $+III$ (left) and $+I$ (right). The spin density $\rho(\omega)$ used in the calculation is shown as a dashed line.

The experimental sequence starts with the injection of a microwave field at the frequency ω_p, this pulse is injected via the resonator that is kept detuned from

spins and qubit at this state. The fact that the resonator is detuned with respect to the injected field means that this field is attenuated and as the attenuation factor is constant in the region around the probed spin resonance this factor only renormalizes the injected power. In order to measure the absorption we transfer the excitation of the spins to the resonator, this is accomplished as the resonator is tuned into resonance with the spin transition being studied for a time τ_S defined in Fig. 4.10. This time is chosen to give a maximal transfer of energy and it is reminiscent of a resonant π pulse. The resonator then is adiabatically sweept trough the qubit anticrossing in a way as to transfer the absorption signal to the qubit which can be readout. Repeating this experimental sequence yields the probability P_e to find the qubit in its excited state. Provided the average number of microwave photons emitted by the spins into the resonator stays lower than 1 to avoid saturating the qubit, the resulting excited state probability $P_e(\omega_p)$ is expected to reproduce the spin ensemble absorption spectrum. Experimental results of Fig. 4.12 indeed display the characteristic HF structure of NV centers consisting in three peaks separated by 2.2 MHz for both spin ensembles $+I$ and $+III$.

The sensitivity of such an ESR spectrometer is set by the efficiency at which signal photons can be transferred from the spins to the resonator, then to the qubit, and by the fidelity with which the qubit state can be measured.

The qubit state is detected in a single-shot with a fidelity of $\simeq 0.7$ at the end of an experimental sequence that lasts typically $50\,\mu$s, yielding a 1% precision on the probability P_e in one second. The transfer of one microwave photon from the cavity to the qubit is performed with an efficiency of the order of unity (in our experiment it is around 0.7 limited by losses in the cavity and qubit), so the limiting factor is the efficiency of the transfer of the spin ensemble excitation to the cavity during their resonant interaction. At first sight one might think that since the spin ensemble and cavity are in the strong coupling limit, one excitation of the spin ensemble should also be converted into a microwave photon with an efficiency of the order of 1, similar to what happened in the coherent oscillations shown in Fig. 4.11. This reasoning is not correct here because the collective spin mode excited by the spectroscopy pulse does not necessarily match perfectly the superradiant mode. Indeed, although the spatial matching of the two modes is

excellent since the spectroscopy pulse is applied through the cavity, this is not the case for spectral matching: only spins having a resonance frequency within the spectroscopy pulse bandwidth $\delta/2\pi = 150$ kHz around ω_p contribute, whereas all spins within the hyperfine(HF) line (total width $\Delta/2\pi \sim 5$ MHz) contribute to the superradiant mode. As a result, one expects an overlap of order $\sqrt{\delta/\Delta}$, implying that the transfer efficiency is limited to about $\delta/\Delta \approx 1/20$. We now make this argument rigorous.

4.4.1 Modeling

To evaluate the resonator population after the interaction with the spins we need to calculate the probability that the excitation created at $t = 0$ in the spins is transferred to the cavity after a time t, this probability being the square modulus of $\langle 0| a(t) b^\dagger_{\omega_p} |0\rangle$. The spins excitation is created by a microwave pulse of central frequency ω_p with a pulse envelope in frequency described by $\alpha_{\omega_p}(\omega) = \alpha(\omega - \omega_p)$, and a typical envelope is a Lorentzian function with FWHM δ. We can define an operator $b^\dagger_{\omega_p}$ that describes the excitation induced by this pulse as

$$b^\dagger_{\omega_p} = \frac{1}{\sqrt{\sum_j |\alpha_{\omega_p}(\omega_j)|^2 g_j^2}} \quad \sum_k \alpha_{\omega_p}(\omega_k) g_k b^\dagger_k \,, \tag{4.12}$$

which comes simply from the standard atom-field interaction for a classical light source such as the one used in the experiment. Once more it is convenient to introduce the vector $X(t)$ of coordinates $\left[\left\langle a(t)a^\dagger(0)\right\rangle, ..., \left\langle b_j(t)a^\dagger(0)\right\rangle, ...\right]$ and use the formal solution of $dX/dt = -(i/\hbar)H_{eff}X$ to write

$$\langle 0| a(t) b^\dagger_{\omega_p} |0\rangle = {x_G}^\dagger \cdot X(t) = \mathcal{L}^{-1}\left[t_{\omega_p}(s)\right] \,, \tag{4.13}$$

with $x_G = (1, 0, 0, ...)$. The initial condition $X(0)$ is the one produced by $b^\dagger_{\omega_p}$ given in Eq.4.12, thus

$$\begin{aligned} t_{\omega_p}(-i\omega) &= \frac{\sum_k \alpha_{\omega_p}(\omega_k) g_k}{\sqrt{\sum_j |\alpha_{\omega_p}(\omega_j)|^2 g_j^2}} \; [(s + iH_{eff})^{-1}]_{0,k} \\ &= \frac{\sum_k \alpha_{\omega_p}(\omega_k) g_k}{\sqrt{\sum_j |\alpha_{\omega_p}(\omega_j)|^2 g_j^2}} \; \left[\frac{g_k \; t_1(-i\omega)}{i\gamma_0 + (\omega - \omega_p)}\right] \\ &= \frac{t_1(-i\omega)}{i\gamma_0 + (\omega - \omega_p)} \frac{\sum_k \alpha_{\omega_p}(\omega_k) g_k^2}{\sqrt{\sum_j |\alpha_{\omega_p}(\omega_j)|^2 g_j^2}} \,, \end{aligned} \tag{4.14}$$

where $t_1(-i\omega) = i/\left[\omega - \omega_0 + i\kappa/2 - W(\omega)\right]$ with $W(\omega) = \sum_j g_j^2/\left[\omega - \omega_j + i\gamma_0/2\right]$. Note that we evaluated $t_{\omega_p}(s)$ for $s = -i\omega$. This is sufficient to perform the Laplace transform inversion as there are no singularities in the imaginary axis of t_{ω_p}. Since the spin density $\rho(\omega)$ is defined as, then $\rho(\omega) = \sum_j \frac{g_j^2}{\Omega_K^2} \, \delta(\omega - \omega_j)$

$$t_{\omega_p} = \frac{\Omega_K \; t_1(-i\omega)}{i\gamma_0 + (\omega - \omega_p)} \frac{(\alpha * \rho)(\omega_p)}{\sqrt{(|\alpha|^2 * \rho)(\omega_p)}} \,. \tag{4.15}$$

The spectral width of the microwave pulse is, in our case, much smaller than any scale that characterizes our distribution $\rho(\omega)$. This allows the rewriting of the convolution above as

$$\frac{(\alpha * \rho)(\omega_p)}{\sqrt{(|\alpha|^2 * \rho)(\omega_p)}} = A\sqrt{\rho(\omega_p)} \,, \tag{4.16}$$

where the constant $A = \frac{\int \alpha(\omega) d\omega}{\sqrt{\int |\alpha(\omega)|^2 d\omega}}$ is purely characterized by the pulse envelope with no dependence on ω_p, yielding for example $A = \sqrt{\delta}\sqrt{\pi/2}$ for a Lorentzian envelope. This means that if we consider that the spins are distributed at a typical range Δ the equation above gives a rigorous justification of the rule of thumb that says that the efficiency of the spins-resonator transfer is given by the overlap $\sqrt{\delta/\Delta}$. Additionally this shows that the density of emitters in the frequency ω_p can be directly measured if we have access to the population in the resonator. To generate the theoretical curve in Fig. 4.12, we perform a numerical inversion of the Laplace transform for each ω_p and take $|\langle 0| a(t) b^\dagger_{\omega_p} |0\rangle|^2$ at $t = \tau_{S,III}$ or

$t = \tau_{S,I}$.

Note that the parameters needed to compute the theoretical curve were already determined on the experiment described in Section 4.3. It is remarkable that a quantitative agreement shown in Fig. 4.12 is obtained. From this calculation, we deduce that the average excitation of the spin ensemble at resonance in the data shown in Fig. 4.12 is of the order of 15, in agreement with the qualitative argument presented above. In the present state of the experiment, the qubit-based ESR spectrometer therefore measures the spectrum of an ensemble of 10^{11} NV centers at an excitation level of order $15\,\mu_B$, in an one minute integration time. We also note that our calculation reproduces a puzzling feature of the data that was not discussed yet: the middle peak of the $P_e(\omega_p)$ curve has a lower amplitude than the two other peaks, both for the $+I$ and the $+III$ curves as seen in Fig. 4.12, although the spin density $\rho(\omega)$ is clearly expected to show a maximum in the central peak. Our ESR protocol thus appears to slightly distort the absorption spectrum. This phenomenon originates from the ω_p dependence of the energy transfer efficiency from the spins into the cavity, caused by the fact that $\Omega_K \approx \Delta$ in our sample. It could be corrected in future experiments either by increasing Ω_K or by transferring the spin excitation to the cavity with an adiabatic passage.

Note, however, that a quantitative agreement could only be obtained after the inclusion of additional ESR frequencies in the distribution $\rho(\omega)$ caused by the hyperfine interaction of the NV center with neighboring ^{13}C nuclei with the 1.1% natural abundance as expected. Fig. 4.13 compares the simulation with and without these additional transitions at a slightly higher power injected on the spins. It is remarkable that the experiment is sensible to the point of detecting such a small effect. These transition could be taken into account because they were carefully measured in the literature. In the next section we review a bit about the physics behind this effect.

4.4.2 Isotopic impurities in NV centers

So far we neglected the nuclear spin of the carbon atoms that form the diamond crystal. This is because the most abundant carbon isotope is the ^{12}C which in

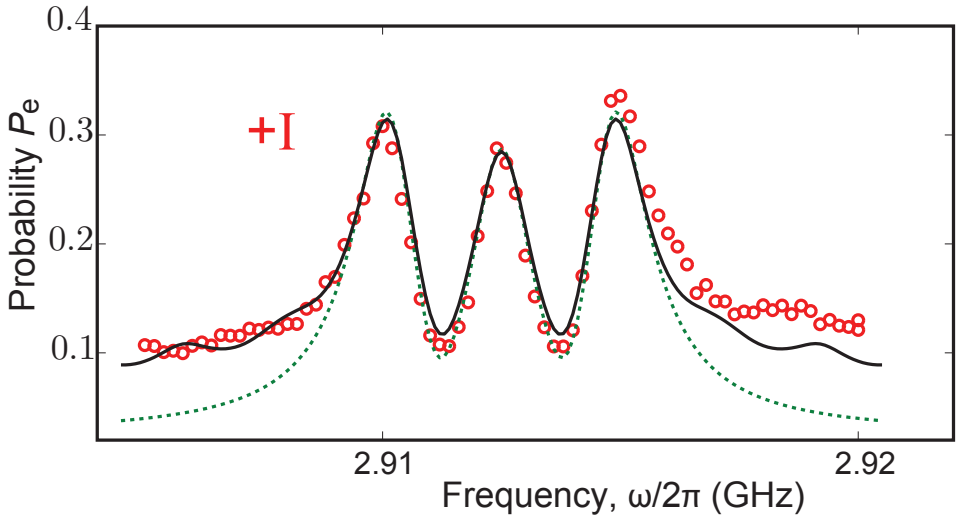

Figure 4.13: Experimental data for ESR spectroscopy at larger power (red circles). At this power the differences between the simulation taking into account the ^{13}C additional ESR frequencies (black solid line) and the simulation without these transitions (green doted line) are clear. Note that in the experiment the central oscillations go bellow the point on the sides of the spectral window, an effect that could never be reproduced without the ESR lines shifted by the hyperfine interaction with ^{13}C spins.

fact does posses zero total nuclear spin. Nevertheless, if the crystal is fabricated with carbon which is not isotopically purified there will be 1.1% of ^{13}C atoms. As this isotope posses a nuclear spin $I^{(C)} = 1/2$, when it lies on a neighboring lattice site of the NV defect, the spin Hamiltonian Eq. (4.1) will gain additional terms

$$H_C = \gamma_C \vec{B}.\vec{I}^{(C)} + \vec{S}.\mathcal{A}_C.\vec{I}^{(C)} \ . \tag{4.17}$$

Note that for each position that the ^{13}C can occupy we have a different tensor $\mathcal{A}_C$. The equation above can be simplified with a secular approximation in which we neglect S_x and S_y terms, which can be justified because these operators are related to an unlikely spin-flip(as long as the elements of $\mathcal{A}_C$ are small compared to $D = 2.88$GHz). This way we can replace the tensor $\mathcal{A}_C$ by a vector $\vec{A}$ and Eq. (4.17) becomes

$$H_C = \gamma_C \vec{B}.\vec{I}^{(C)} + S_z \vec{A}_C.\vec{I}^{(C)} \ . \tag{4.18}$$

To understand the effects of this coupling let us study the operator H_C for a fixed ^{14}N nuclear-spin projection (the results are unchanged if we consider another projection).

In the basis $\left\{\left|m_S = 0, m_I^{(C)} = \frac{1}{2}\right\rangle, \left|0, -\frac{1}{2}\right\rangle, \left|-1, \frac{1}{2}\right\rangle, \left|-1, -\frac{1}{2}\right\rangle, \left|1, \frac{1}{2}\right\rangle, \left|1, -\frac{1}{2}\right\rangle\right\}$, H_C is given by

$$H = \left(\begin{array}{cc:cc:cc}
\frac{\gamma_c B}{2} & 0 & 0 & 0 & 0 & 0 \\
0 & -\frac{\gamma_c B}{2} & 0 & 0 & 0 & 0 \\ \hdashline
0 & 0 & E_- - \frac{Az - \gamma_c B}{2} & -\frac{1}{2}(A_x - iA_y) & 0 & 0 \\
0 & 0 & -\frac{1}{2}(A_x + iA_y) & E_- + \frac{Az - \gamma_c B}{2} & 0 & 0 \\ \hdashline
0 & 0 & 0 & 0 & E_+ + \frac{Az - \gamma_c B}{2} & \frac{1}{2}(A_x - iA_y) \\
0 & 0 & 0 & 0 & \frac{1}{2}(A_x + iA_y) & E_+ - \frac{Az - \gamma_c B}{2}
\end{array}\right),$$

where $E_\pm = D \pm \gamma_{NV} B$. The diagonalization of each of the 2×2 blocks can be carried with ease if we notice that each 2×2 matrix is identical to the one of a spin $1/2$ placed in a magnetic field. For instance in the subspace $\{\left|m_S = -1, m_C = \pm\frac{1}{2}\right\rangle\}$ the matrix is

$$V_{\{-1,\pm\frac{1}{2}\}} = E_- - \sigma_z \frac{A_z - \gamma_c B}{2} - \sigma_x \frac{A_x}{2} - \sigma_y \frac{A_y}{2} \ . \tag{4.19}$$

The fictitious field has a projection in the plane xy with an intensity proportional to $A_{\perp z} = \sqrt{A_x^2 + A_y^2}$ and from this simple analogy we see that if $|A_z - \gamma_c B| \gg A_{\perp z}$ the field is almost parallel to the z axis and the eigenstates should not change from the uncoupled case. If a spin half was placed in a field $B \parallel \hat{z}$, the hamiltonian in the basis of eigenstate of σ_z will be diagonal and we see that the two eigenvalues are proportional to $\pm B$. But the $\hat{z}$ direction is no different from any other so from this simple argument we can get the eigenvalues for $V_{\{-1,\pm\frac{1}{2}\}}$ as

$$\begin{cases} E_1 = E_- - \sqrt{A_{\perp z}^2 + (A_z - \gamma_C B)^2}\,, \\ E_2 = E_- + \sqrt{A_{\perp z}^2 + (A_z - \gamma_C B)^2}\,. \end{cases} \tag{4.20}$$

We could obtain the eigenvectors if we noted that, in analogy with the field in the $\hat{z}$ direction, the eigenstates have Bloch vectors parallel to the fictitious field (for details see Complement B_{IV} of [103] or Sec. 3.4 of [3]). For a high field $B \approx 500$ G we can get $A_x = \gamma_c B$ and thus the eigenstates will mix equally $|m_C = 1\rangle$ and $|m_C = -1\rangle$ yielding new allowed transitions [104]. We will be rather constrained to much smaller fields and we will be on the situation where the eigenstates are unaltered. In our case, the ^{13}C nuclear-spin projection is identical regardless of the NV center electronic spin and only two nuclear-spin conserving transitions can be observed in the subspace $\{\left|m_S = -1, m_C = \pm\frac{1}{2}\right\rangle\}$. By considering all the ^{14}N nuclear-spin projections and also the transitions involving $m_S = +1$ we have a total of 12 transitions for each family of NV centers (defects which have the same angle between the NV axis and the external magnetic field).

We now study the values of hyperfine splitting induced by nearby ^{13}C nuclear spins for a low magnetic field magnitude ($B < 20$ G). As the gyromagnetic ratio for $\gamma_C = 1.07$ KHz $G^{-}1$ is small the nuclear Zeeman will be small compared to $|\vec{A}|$ and we can write the splitting between transition frequencies associated with different ^{13}C nuclear-spin projection as

$$\begin{aligned} A_{hs}^C &= \pm\sqrt{A_{\perp z}^2 + A_z^2}\left(1 + \frac{\gamma_c B}{2\sqrt{A_{\perp z}^2 + A_z^2}}\right) \\ &\approx \pm\sqrt{A_{\perp z}^2 + A_z^2}\,. \end{aligned} \tag{4.21}$$

The second line of Eq. (4.21) is justified when A_{hs}^{C} is in the MHz range while $\gamma_c B < 20$ Khz. This simplifies the analysis as A_{hs}^{C} does not depend on the angle between the external magnetic field and the ^{13}C nuclear spin. The lattice sites of the diamond lattice around an NV defect are depicted and labeled in Fig. 4.14. Experiments performed measuring Electron-Spin-Resonance signals from single defects have identified a range of discrete values for A_{hs}^{C} which is reminiscent of the discrete positions that the C atoms can occupy on the lattice. They agree with *ab initio* calculations in a way that is possible to identity the lattice site associated with a given A_{hs}^{C}, this data is displayed in Table 4.1. Each of these lattice sites is occupied with probability 1.1% by a ^{13}C nuclear spin. So if we make a cutoff at $A_{hs}^{C} = 1$MHz, we can consider only the first 36 nearest sites which means that around $(1-\varepsilon)^{36} = 67\%$ of the NV centers will have no shift due to ^{13}C, $36\varepsilon.(1-\varepsilon)^{35} = 27\%$ will display a shift associated with a single ^{13}C and less than 6% will interact strongly with more than one ^{13}C.

Lattice Site	Distance to site()	Number of sites	$A_{hfs}(MHz)$ Measured	$A_{hfs}(MHz)$ Theory
A	3.89	6	13.72(3)	14.8
B	3.9	3	12.78(1)	13.9
C	2.52	3	-8.92(3)	-7.5
D	2.50	6	-6.52(4)	-5.7
E,F	2.93, 2.96	6,3	4.2(1)	4.6, 4.7
G,H	5.05, 5.05	6,3	2.4(3)	2.6, 2.3

Table 4.1: Observed hyperfine splittings A_{hfs} at low magnetic field ($<$ 50G) from [105]. Each hyperfine shift is an average value for what has been observed in a set of 3 to 5 single NV centers which give approximately the same value for A_{hfs}. The number in parenthesis give the deviation found within a given set. Identification of the lattice site in which we have a ^{13}C is possible because of the close agreement with theoretical prediction from *ab initio* model using supercell density functional calculations [105]. Not shown on the table is the A_{hfs} associated with ^{13}C as one of the first-neighbors (lattice site 'o'), in this case we have a large shift $A_{hfs} = 130$ MHz [106, 93] .

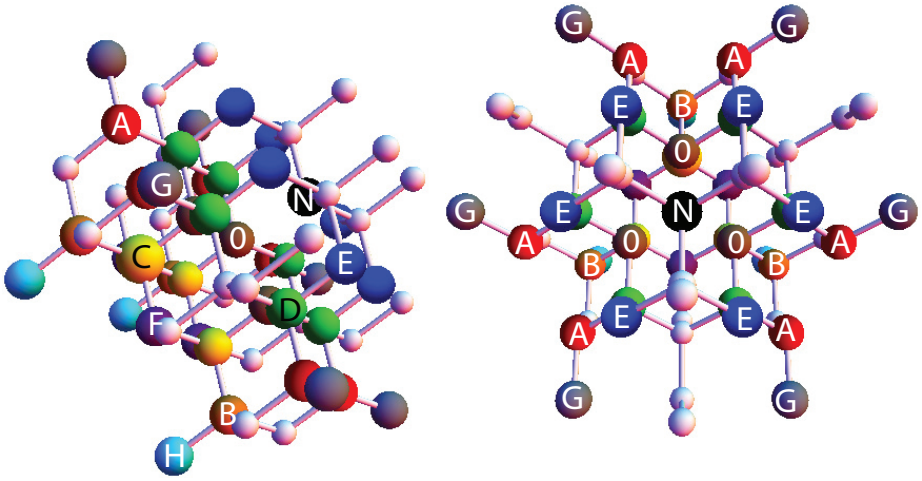

Figure 4.14: Reproduced from [105] with author's permission. Two views of the geometry of the NV defect, with lattice sites for proximal ^{13}C nuclear spins labeled as in table 4.1. The nitrogen is labeled 'N', whereas sites labelled Ś0Š are the nearest neighbors to the vacancy ($A_{hfs} = 130$ MHz).

4.5 Summary

In conclusion the experiments we modeled bring the first proof of concept of a spin-based quantum memory for superconducting qubits and one of the first technologies derived from hybrid circuits. We have successfully explained all the experimental data and shown that the experiments are sensible to the point where a quantitative agreement can only be obtained if we include hyperfine interaction with 1.1% natural abundance ^{13}C.

Chapter 5

Proposal for fast readout in a Josephson qubit

A fast high-fidelity readout is an essential requirement for quantum information processing, in particular for implementations like measurement-based quantum computing [17, 16]. A high readout fidelity can be a valuable resource to deal with moderate gate fidelities if one is to implement quantum error correction codes [107]. Fault-tolerant quantum computing requires readout fidelities (defined as $F = 1-\varepsilon$ where ε is the probability of determining the state incorrectly) of 99.9% to avoid a large increase in the number of physical qubits per logical qubit [108]. For any physical implementation of a qubit readout, fidelity is usually limited by the time available to integrate a detector's signal, to give the best possible signal-to-noise ratio, before the qubit decays. Besides, fast acquisition is important if we want to exploit the information after the measurement as in a state preparation protocol or in a closed feedback loop. In this framework, the ability to perform fast single shot readout of a quantum bit is highly desirable.

In superconducting qubits, the highest one shot fidelity up to now was obtained by switching quantum measurements using escape process [109] and bifurcation amplifier[97, 98]. In fact, a high efficiency bifurcation amplifier was used to readout the qubit in the experiments we analyzed in Section 4.4 where the apparatus demonstrated unprecedent spin-spectroscopy sensitivity. The intrinsic drawback of these methods is their destructiveness. An alternative readout

consists in coupling dispersively a qubit to a resonator [110]. The qubit acts as a state-dependent refractive index that shifts the resonator frequency and the measurement of this shift is performed by probing the resonator with an external microwave. The QND character is preserved as long as one remains in the dispersive regime, limiting the photon population $\bar{n}$ of the resonator below a critical value[111], so as the probe power. Large averaging and low temperature amplifiers have thus to be used to reach high fidelity. Thanks to recent advances in parametric amplification using Josephson junction circuits [45, 112, 113, 114, 115], single shot readout has been demonstrated. However this measurement scheme still requires very small resonator linewidth, lowering the circuit bandwidth and imposing several hundred nanoseconds measurement time. Moreover, even with parametric amplifier improvements, the photon population inside the resonator still remains large ($\bar{n} \geq 10$) [114, 115] and may induce additional qubit dephasing or relaxation. Consequently, further improvements need to be realized to reach fast and high fidelity measurements.

In this Chapter, we propose an original method which is able to realize fast QND measurements of a qubit with large resonator linewidth and measurement bandwidth, while preserving high fidelity. The protocol is based on the use of a diamond-shape artificial atom and the system consists in an inductive dc-SQUID coupled to a coplanar resonator described in Section 5.1. In Section 5.2 we evaluate the performance of this device taking into account experimental amplification noise and realistic circuit parameters.

5.1 Coupled qubits in the dc-SQUID

In our method we shall consider the symmetrical dc-Squid depicted in Fig. 5.1 which presents a total inductance L associated with the SQUID loop. Following Chapter 2 it is simple to write its total Hamiltonian: we just have to add energies of the form of the current biased junction studied in Section 2.2.3 and consider the flux quantization in the loop. Note that the external current I_e does not circulate in the loop and, therefore, does not contribute to the flux. This way the

Hamiltonian is given by

$$H = 4E_C(N_1^2 + N_2^2) - E_J[\cos(\phi_1) + \cos(\phi_-)] + \frac{E_L}{2}\left(\phi_1 - \phi_2 - \phi_e\right)^2 + \frac{\hbar}{4e} I_e(\phi_1 + \phi_2)\,, \tag{5.1}$$

It is convenient to write the Hamiltonian as a function of the sum and thye difference of the Josephson phases $\phi_\pm = (\phi_1 \pm \phi_2)/2$

$$H = 2E_C(N_+^2 + N_-^2) - 2E_J\cos(\phi_+)\cos(\phi_-) + 2E_L\left(\phi_- - \frac{\phi_e}{2}\right)^2 + \frac{\hbar}{2e} I_e\phi_+\,. \tag{5.2}$$

The classical dynamical equations for the phase can be cast in the suggestive form

$$\begin{cases} m\ddot{\phi}_+ = -\partial_{\phi_+} U(\phi_+, \phi_-) \\ m\ddot{\phi}_- = -\partial_{\phi_-} U(\phi_+, \phi_-)\,, \end{cases} \tag{5.3}$$

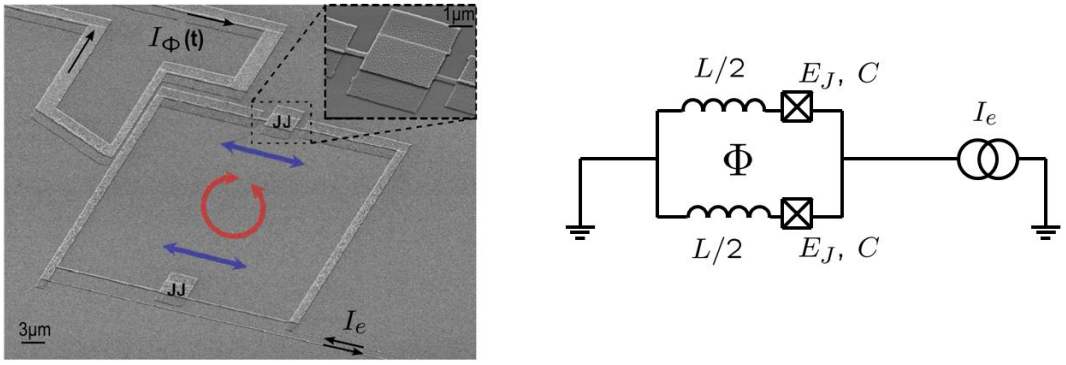

Figure 5.1: A micrograph of the circuit made with aluminium is shown on the left. The symmetric and antisymmetric oscillation modes are illustrated by blue and red arrows, respectively. The two small squares are the two Josephson junctions (enlarged in the top right inset). The flux Φ applied on the loop is generated by the current I_Φ running next to the loop. Courtesy of Olivier Buisson. On the right the equivalent electrical circuit were only the flux Φ caused by I_Φ is shown.

and the phase dynamics is mapped on the dynamics of a particle of 'mass' $m = 2C(\hbar/2e)^2$ and coordinates (ϕ_+, ϕ_-) evolving in the potential $U(\phi_+, \phi_-)$

$$U(\phi_+, \phi_-) = 2E_J \left[-\cos(\phi_+)\cos(\phi_-) + \frac{E_L}{E_J}\left(\phi_- - \frac{\phi_e}{2}\right)^2 - \frac{\hbar}{2e}\frac{I_e}{E_J}\phi_+ \right] . \quad (5.4)$$

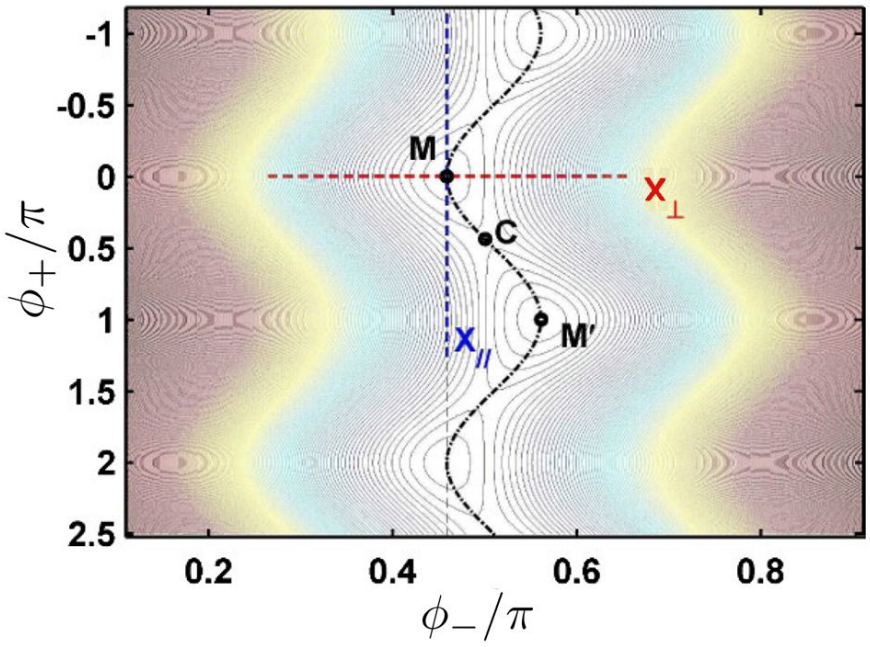

Figure 5.2: 2D potential for a dc SQUID with $E_L = 3E_J$, $I_e = 0$ and $\Phi = 0.51\Phi_0$. M and M' indicate two different local minima separated by a saddle point C. The dashed black line represents the trajectory of minimum energy. Adapted from [116].

If $E_L/E_J \gg 1$, the term $\cos(\phi_+)\cos(\phi_-)$ is dominated by the term $\frac{E_L}{E_J}\left(\phi_- - \frac{\phi_e}{2}\right)^2$ and we can see that the potential will trap the phase difference and the quantum behavior of the circuit is described only by the 'longitudinal' mode associated with the one-dimensional motion of the ϕ_+ phase. The dc-SQUID circuit has been extensively studied in this regime where it behaves as a tunable phase qubit [117, 118, 119]. Here we will consider instead a circuit with large loop inductance $E_J \geq E_L$ and the dynamics of the system becomes fully two-dimensional. This regime has been experimentally observed only very recently in [120]. The 2D

potential Eq. (5.4) is plotted in Fig. 5.2 with $E_L = 3E_J$. For $\hbar I_e < 2eE_J$ this potential presents a periodic series of local minima separated by potential barriers. We know describe the dynamics of the particle trapped in a potential minimum following [116]. In this work the authors showed that the zero-bias current point $I_e = 0$ is protected against current fluctuation so we shall restrict our development to this case. The origin of the protection is that at this point the two first eigen-energies do not depend on the bias current to first order. We now place ourselves at the minimum $\phi_+^{min} = 0$ and $\phi_-^{min} + (E_J/2E_L)\sin\phi_-^{min} = \hbar I_e/(2eE_J)$. We define the coordinates $(\hat{x}_\parallel, \hat{x}_\perp)$ centered in the minimum corresponding to the motion parallel or transverse to the trajectory of minimum energy. By expanding the potential to fourth order we have the Hamiltonian given by $H = H_\parallel + H_\perp + C$, where $H_\parallel$ and $H_\perp$ describe the anharmonic oscillators in each direction having $\omega_\parallel$ and $\omega_\perp$ as the frequencies of the first transition. C describes the coupling of these anharmonic oscillators

$$C(\hat{x}_\parallel, \hat{x}_\perp) = \hbar g_{21}\hat{x}_\parallel^2\hat{x}_\perp + \hbar g_{22}\hat{x}_\parallel^2\hat{x}_\perp^2 \,. \tag{5.5}$$

The coupling constants are tuned by the circuit parameters and they are found to be $\hbar g_{22} = -e^2/(2C\sqrt{1+2E_L/E_J})$ and $\hbar g_{21} = -E_J(\hbar/m)^{3/2}(\omega_\parallel\sqrt{\omega}_\perp)^{-1}\sin(\phi_-^{min})$ and are typically much smaller than the plasma frequencies $\omega_\parallel, \omega_\perp$ [120, 116]. This frequency hierarchy allows us to treat C as a perturbation of the uncoupled modes which have energies $E_{n_\parallel,n\perp} = E_{n_\parallel} + E_{n\perp}$. We introduce annihilation operators $\hat{a}_\parallel$ and $\hat{a}_\perp$ of the longitudinal and transversal modes obtaining

$$\begin{aligned} C(\hat{a}_\parallel, \hat{a}_\perp) =& \frac{1}{2\sqrt{2}}\hbar g_{21}[\hat{a}_\parallel^2 + (\hat{a}_\parallel^\dagger)^2 + 2\hat{a}_\parallel^\dagger\hat{a}_\parallel + 1](\hat{a}_\perp + \hat{a}_\perp^\dagger) \\ &+ \frac{1}{4}\hbar g_{22}[\hat{a}_\parallel^2 + (\hat{a}_\parallel^\dagger)^2 + 2\hat{a}_\parallel^\dagger\hat{a}_\parallel + 1][\hat{a}_\perp^2 + (\hat{a}_\perp^\dagger)^2 + 2\hat{a}_\perp^\dagger\hat{a}_\perp + 1] \,. \end{aligned} \tag{5.6}$$

One advantage of the annihilation operators is that they give direct information about which are the relevant processes. For instance $(a_\parallel^\dagger)^2 a_\perp$ is a term that leads to the simultaneous annihilation of one excitation in the transverse mode with the double excitation of the longitudinal mode. Such events are highly rare and have no appreciable effect on the dynamics if we do not meet a quasi-resonant condition $2\omega_\parallel \simeq \omega_\perp$. This term was exploited in [120] to generate coherent frequency

conversion, i.e. a coherent exchange of a single excitation of the transverse mode with a double excitation of the longitudinal one. Here we choose instead to tune the circuit (or the external flux) to yield $g_{21} \ll |2\omega_{\parallel} - \omega_{\perp}|$. In this case, by projecting the Hamiltonian in the qubits subspaces we get

$$H_{qubits} = \hbar\omega_{qb}\sigma_z^{qb}/2 + \hbar(\omega_a - g_{zz}\sigma_z^{qb})\sigma_z^a/2\,, \tag{5.7}$$

$g_{zz} \equiv -g_{22}$; where the logical (ancilla) qubit 'qb'('a') is composed by the first two levels of the longitudinal (transversal) mode. In the absence of coupling between the two modes, the transition frequency of the qubit and ancilla are defined as ω_{qb} and ω_a, respectively. By reducing the critical current of the junctions, keeping the ratio E_J/E_L constant, one can increase the strength of the coupling term g_{zz} up to 250 MHz providing a strong dispersive frequency shift proportional to the state of each qubit. The interaction Hamiltonian we have just obtained is of particular interest to build a diamond-shape artificial atom. The g_{zz} term can be viewed as an analogue of a cross-Kerr term between the two quantum systems. This interaction leads to a conditional energy transition of the ancilla which depends on the quantum state of the qubit $|g\rangle_{qb}$ and $|e\rangle_{qb}$. The respective frequencies of the transitions $|g\rangle_{qb}|g\rangle_a \rightarrow |g\rangle_{qb}|e\rangle_a$ and $|e\rangle_{qb}|g\rangle_a \rightarrow |e\rangle_{qb}|e\rangle_a$ are $\hbar(\omega_a + g_{zz})$ and $\hbar(\omega_a - g_{zz})$ as sketched in 5.3.

5.2 QND readout on the dc-SQUID

The artificial atom will be coupled to a coplanar waveguide resonator that will mediate the interaction with microwave pulses. When the artificial atom is localized at the center of the resonator, the quantum fluctuation of the flux is maximal and the voltage fluctuations are reduced to zero. Because of zero-current and zero-flux bias working point, the qubit is not affected by flux fluctuations, leading to zero-coupling between the resonator and the qubit. This way, σ_z^{qb} commutes with the Hamiltonian of the system, ensuring the non-destructive character of the measurement whatever the number of photons in the resonator. The artificial atom

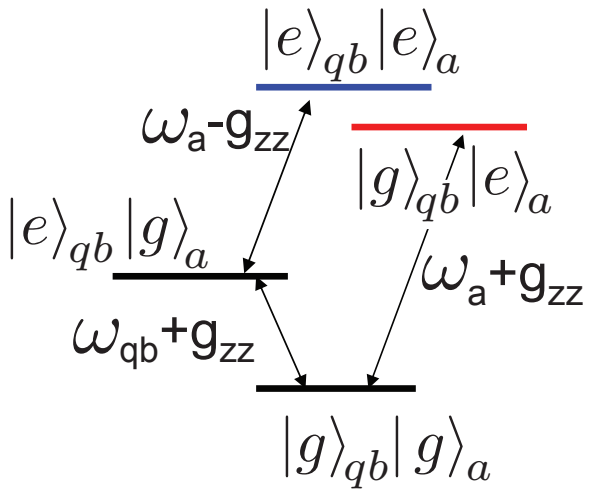

Figure 5.3: Energy levels of the diamond shape artificial atom.

inside a coplanar resonator is described by the Hamiltonian:

$$\begin{aligned} H_{free} &= \hbar\omega_{qb}\sigma_z^{qb}/2 + \hbar(\omega_a - g_{zz}\sigma_z^{qb})\sigma_z^a/2 \\ &+\hbar\omega_r(a^\dagger a + 1/2) - i\hbar g_a(a\sigma_+^a - a^\dagger\sigma_-^a)\,. \end{aligned} \tag{5.8}$$

The three first terms describe the artificial atom, the fourth term the resonator at frequency ω_r. We consider the frequency condition between the resonator and the ancilla: $\omega_r = \omega_a + g_{zz}$. In this picture, the first qubit is the qubit to read out, the second qubit playing the role of an ancilla whose frequency depends on the first qubit state. The resonator is not coupled to the qubit but only coupled to the ancilla, which is an important difference with respect to other readout schemes. The transmission is conditioned to the state to measure through a QND process. Contrary to dispersive coupling based methods, this approach imposes no harsh constraint on the amplification and resonator bandwidth, allowing to reach fast, one shot, high fidelity QND read-out of our qubit even with the present day amplifier technology.

The system will be probed by a transmission experiment where the microwave transmission through the resonator is measured for different pumping powers and frequencies. To describe the transmission properties of the cavity as a function

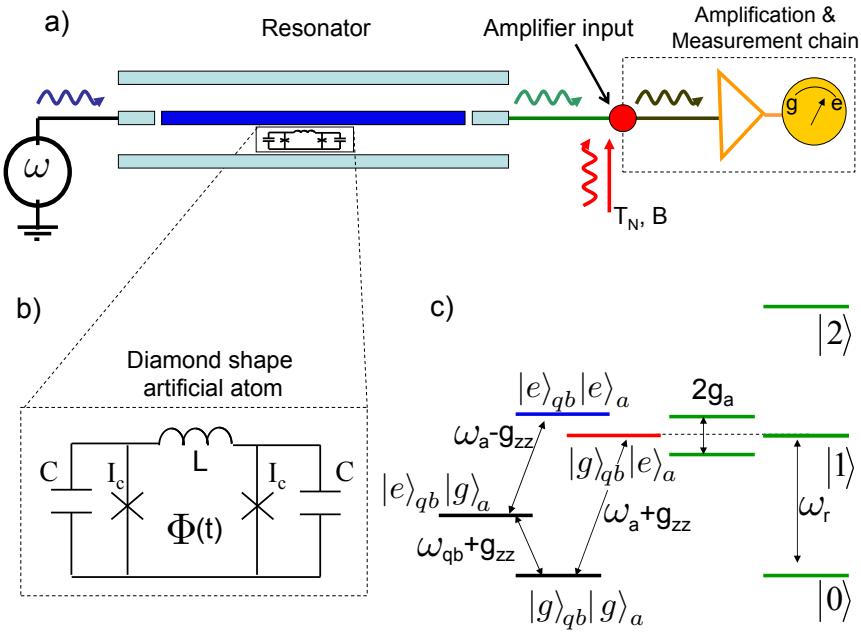

Figure 5.4: a) Schematic circuit for a fast QND read-out. The incident microwave signal ($\omega = \omega_r + \delta_L$) is transmitted through the 1D resonator coupled to a superconducting artificial atom which contains the qubit to be measured. The signal is amplified and homodyne detected to measure the amplified transmitted signal. The noise amplifier, characterized by its noise temperature T_N and bandwidth B, is illustrated by additional microwave source at the amplifier input. b) The artificial atom is realized by an inductive dc-SQUID leading to a transmon qubit coupled to an ancilla qubit by a cross-Kerr term. The ancilla is strongly coupled to the resonator. c) Energy spectrum of the diamond shape artificial atom and the resonator. The 1D resonator and the ancilla are coupled resonantly ($\omega_r = \omega_a + g_{zz}$) or dispersively ($\omega_r > \omega_a - g_{zz}$) depending on the qubit state, leading to a large variation of the transmitted signal amplitude.

of the qubit state, we write a closed set of differential equations from Eq. (5.8) describing the time evolution of the system operators in the Heisenberg picture. These are deduced from input-output equations established in the case of a transmitting cavity as in [121]. We define the external fields b_{in} (injected microwave field), b_r (reflected field), and b_t (transmitted field) that lead to the damping of the intracavity field: $b_r = b_{in} + i\sqrt{\kappa}a$ and $b_t = i\sqrt{\kappa}a$ where κ is the resonator coupling to external transmission line modes. We consider an overcoupled cavity, that allows to neglect the internal losses of the resonator. Therefore κ defines the resonator linewidth. The qubit energy relaxation and dephasing times are assumed to be very long compared to resonator relaxation time ($\kappa T_1 \gg 1$ and $\kappa T_2 \gg 1$). The Heisenberg equations are written in the frame rotating at the frequency ω of the probe, yielding

$$\begin{aligned}
\dot{\sigma_z^a} &= -2g_a(\sigma_+^a a + \sigma_-^a a^\dagger)\,, \\
\dot{\sigma_-^a} &= -i(\omega_r - \omega + \delta_s)\sigma_-^a + g_a\sigma_z^a a\,, \\
\dot{\sigma_-^{qb}} &= -i(\omega_{qb} - g_{zz}\sigma_z^a)\sigma_-^{qb}\,, \\
\dot{a} &= -i(\omega_r - \omega)a - \kappa a + g_a\sigma_-^a + i\sqrt{\kappa}b_{in}\,,
\end{aligned} \tag{5.9}$$

where $\delta_j = -g_{zz}(1 + \sigma_z^{qb})$ is the qubit state dependent shift. The index j defines the qubit state ($j = g$ or e). Note that, as expected from a QND measurement, the evolution preserves $\langle\sigma_z^{qb}\rangle$. We are interested in the transmission properties of this system in the steady state regime established after a time much larger than $1/\kappa$. We adopt the semiclassical approach where the quantum correlations between atomic and field operators are neglected [121]. Frow now on we identify the operators with their average complex values as they could be measured in a homodyne experiment. The ratio $t(\omega) = \langle b_t\rangle / \langle b_{in}\rangle$ checks, in the steady-state regime

$$\begin{aligned}
t_j(\omega) &= t_0(\omega)\left\{1 - \frac{1}{1+\frac{p}{p_s}}\left[1 - \frac{2i(\omega_r + \delta_j - \omega)}{\Gamma t_0(\omega)}\right]^{-1}\right\} \\
\frac{p_s}{\Gamma} &= \frac{(\omega_r + \delta_j - \omega)^2}{\Gamma^2} + \left[\frac{(\omega_r - \omega)}{\Gamma}\frac{(\omega_r + \delta_j - \omega)}{\kappa} - 1/2\right]^2
\end{aligned} \tag{5.10}$$

where we introduced the relaxation time in the cavity mode $\Gamma = 2g^2/\kappa$ and the drive power p in units of photons per second $p = \left\langle b_{in}^{\dagger} b_{in} \right\rangle$. The quantity $t_0(\omega) = -[1 + i(\omega_r - \omega)/\kappa]^{-1}$ is the transmission of the empty resonator, and p_s is the saturation power of the atom-cavity system.

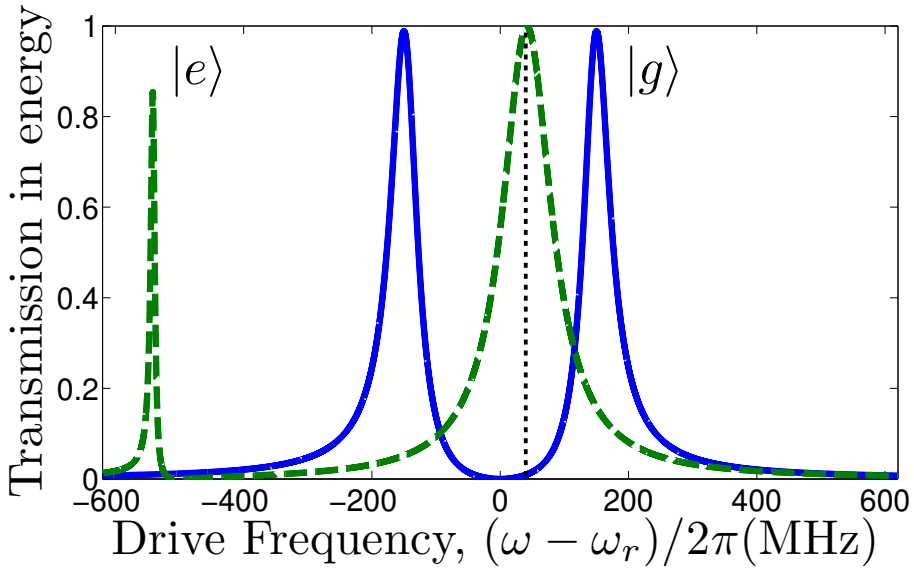

Figure 5.5: Transmission coefficient at low pump power for a microwave pulse injected in a 1D resonator containing a diamond-shape artificial atom with $\kappa =$ 40MHz and $p =$ 1photon/ns. Blue solid curve: qubit state $|g\rangle$. Green dashed curve: qubit state $|e\rangle$. Frequency is centered on the bare cavity. For all the numerical calculations, we took $g_{zz}/2\pi = 250$ MHz , $g_a/2\pi = 150$ MHz and a cavity linewidth $\kappa/2\pi = 40$ MHz ($Q = 250$) and $p << p_s$. The black dotted line indicates the pump frequency δ_L, at this point the transmission varies abruptly as the qubit state changes.

The essence of the protocol is pictured in Fig.5.5, in the linear regime when $p \ll p_s$. In this regime, the transmission is given by $t_j(\omega) = \left[\frac{1}{t_0(\omega)} + \frac{i\Gamma}{2(\omega_r + \delta_j - \omega)}\right]^{-1}$. If the qubit is in state $|g\rangle$, $\delta_g = 0$ so that the ancilla qubit is resonant with the cavity mode and the transmission consists of two peaks located at $\pm g_a$ with respect to the frequency of the resonator. If the qubit is in state $|e\rangle$, $|\delta_e| = 2g_{zz}$, inducing a dispersive coupling between the resonator and the ancilla provided that $g_{zz} > g_a$. The transmission essentially consists in a single peak slightly

shifted by a quantity $\delta_L = g_{zz}(\sqrt{1+g_a^2/g_{zz}^2}-1)$ with respect to the bare cavity frequency (see Fig. 5.5). Thus a change in the state of the qubit to measure can now translate into a switch from dispersive to resonant coupling between the resonator and the ancilla. This is evidenced by a visible displacement in the transmission peaks by a quantity g_a, which can be as high as $150MHz$, between one and two orders of magnitude higher than the usual dispersive ac-Stark shift[122, 115]. As will shall see, this strong effect allows to increase the linewidth of the resonator while keeping a high fidelity readout. Working with a low Q cavity has important advantages. First, it drastically increases the total bandwidth of the circuit, thus the readout speed. Moreover, for the same probe power, the average intracavity photon number is lower, which is known to preserve the lifetime and coherence time of the qubit. The readout is performed by the injection of a short microwave pulse of power p at the frequency $(\omega_r + \delta_L)/2\pi$. Thus, the transmitted power depends on the state of the qubit, giving rise to two conditional output signals $p_{t|j} = \left\langle b_t^\dagger b_t \right\rangle = |t_j|^2 p$. Note that when p largely overcomes p_s, one recovers the transmission pattern $t_0(\omega)$ of the empty cavity, a signature of saturation [121] which limits the information on the qubit state.

We introduce now the model to optimize the measurement scheme. The performances of the readout are usually quantified by two figures of merit, namely its fidelity $\mathcal{F}$ and speed. The speed is all the higher as the typical correlation time between two measurements τ_c is lower. It is related to the inertia of the circuit, in particular imposed by the resonator as τ_c is always larger or equal to κ^{-1}. Fidelity and correlation time depend on two independent parameters that should be optimized: first, the resonator linewidth should be narrow enough to give a large contrast between the two transmission patterns ($\kappa < g_a, g_{zz}$); but large enough to allow large transmitted signal and therefore high speed qubit readout for a given photon number $\bar{n}$ inside the resonator $p_{t|j} = \bar{n}\kappa$. In the same way, the driving power p should be sufficiently low to avoid the saturation of the ancilla $p < p_s$, but high enough to have large $p_{t|j}$. It is worth to note that the frequency chosen for the drive populates minimally the ancilla because the dressed ancilla-resonator states are always detuned from the driving field. This allows to use potentially high values for p before the ancilla saturates.

5.2.1 Amplification noise

In a typical circuit QED experiment, microwave photons are usually amplified before being sent through a homodyne detection scheme and digitalized within a short time interval τ, which is usually taken equal to τ_c. For our purpose, we shall consider the field at the entrance of the amplifying chain. The chain is modeled by a perfect amplifier [112] radiating at the input of the circuit a thermal field of effective temperature T_N. This temperature ranges from a few hundreds of mK for the recent generation of quantum limited devices[113, 114], to $4-10$K for commercial device. The total noise power is $\mathcal{N} = (k_B T_N/\hbar\omega)B$, where ω is the operating frequency and B the bandwidth of the amplifier. Note that like the resonator, the amplifier behaves as a filter, thus imposes a lower band to the correlation time $\tau_c > B^{-1}$. Consequently, high speed measurements are obtained at the price of increased bandwidth and noise power $\mathcal{N}$.

Estimation of the fidelity readout is based on the photon number distributions $\mathbf{P}(n|j)$ conditioned to the qubit state ($j = g, e$) that we computed using the Glauber-Sudarshan P-representation [123]. In this representation, the superposition of two fields is given by the convolution of the two P functions. In our case, this simply corresponds to the P-representations of a thermal field of temperature T_N displaced by a coherent field of amplitude $\sqrt{p_{t|j}}$ (the phase is unimportant as there is no phase relation between the added fields)

$$P(\alpha) = \frac{1}{\pi\mathcal{N}} \exp(-|\alpha - \sqrt{p_{t|j}}|^2/\mathcal{N})\,. \tag{5.11}$$

With this representation of the density matrix we can readily calculate the generating function [124] for the photon statistics

$$\begin{aligned}\sum_{n=0}^{\infty} \mathbf{P}(n|j)(1-\xi)^n &= \left\langle e^{-\xi\langle n\rangle}\right\rangle_\alpha \\ &= \frac{1}{1+\xi\mathcal{N}\tau} \exp\left(-\frac{\xi p_{t|j}\,\tau}{1+\xi\mathcal{N}\tau}\right),\end{aligned} \tag{5.12}$$

where $\langle\rangle_\alpha$ stands for phase-space averaging and $\langle n\rangle$ is the average of the number operator. We can promptly extract $\mathbf{P}(n|j)$ by considering the n-th derivative in

both sides of Eq. (5.12) at $\xi = 1$. In this particular case we can simplify the calculation by making the change of variables : $u \equiv \frac{\mathcal{N}\tau}{1+\mathcal{N}\tau}(1-\xi)$

$$\sum_{n=0}^{\infty} \mathbf{P}(n|j) \left(\frac{1+\mathcal{N}\tau}{\mathcal{N}\tau}\right)^n u^n = \frac{\exp(\frac{-p_{t|j}\,\tau}{1+\mathcal{N}\tau})}{1+\mathcal{N}\tau} \frac{\exp(\frac{-x\,u}{1-u})}{1-u} \tag{5.13}$$

where $x \equiv \frac{-p_{t|j}\tau}{(1+\mathcal{N}\tau)\mathcal{N}\tau}$. Note that the last term in the right-hand-side of Eq. (5.13) is nothing but the generating function of the Laguerre polynomials $L_n(x)$

$$\sum_{n=0}^{\infty} L_n(x) u^n = \frac{\exp(\frac{-x\,u}{1-u})}{1-u}\,, \tag{5.14}$$

and it is thus easy to see that

$$\mathbf{P}(n|j) = \frac{\mathcal{N}^n \tau^n}{(1+\mathcal{N}\tau)^{n+1}} \exp\left(\frac{-p_{t|j}\,\tau}{1+\mathcal{N}\tau}\right) L_n\left(\frac{-p_{t|j}\ /\mathcal{N}}{1+\mathcal{N}\tau}\right)\,. \tag{5.15}$$

5.2.2 Expected Fidelity

An inference error happens when the measurement yields a result in a region where both distributions are non-negligible. We will thus infer the qubit state to be the one associated with the larger probability when it could be the other way around. The fidelity depends on the overlap between the distributions $\mathbf{P}(n|g)$ and $\mathbf{P}(n|e)$ as $\mathcal{F} = 1 - \frac{1}{2}\sum_n \mathbf{P}_e \Theta[\mathbf{P}_g - \mathbf{P}_e] + \mathbf{P}_g \Theta[\mathbf{P}_e - \mathbf{P}_g]$.

The histograms plotted in Fig. 5.6 clearly show how the amplification noise has a large effect on the statistics of the counts associated with each of the qubit states. As the noise power increases with T_N the fidelity is degraded(a vs c and b vs d). By increasing the integration time, one can regain fidelity (a vs b and c vs d). As a matter of fact, it increases the signal, but it also allows to operate with a lower bandwidth, reducing the noise power. With this protocol, a fidelity as high as 90% can already be reached with a commercial amplifier, within a typical time of $\tau = 50$ns.

On the other hand, Fig. 5.7 shows optimization of the fidelity as a function of the resonator linewidth and probe power in the case of a state of the art amplifier of effective temperature $T_N = 140$mK [114]. The digitalization time $\tau = 10$ns has

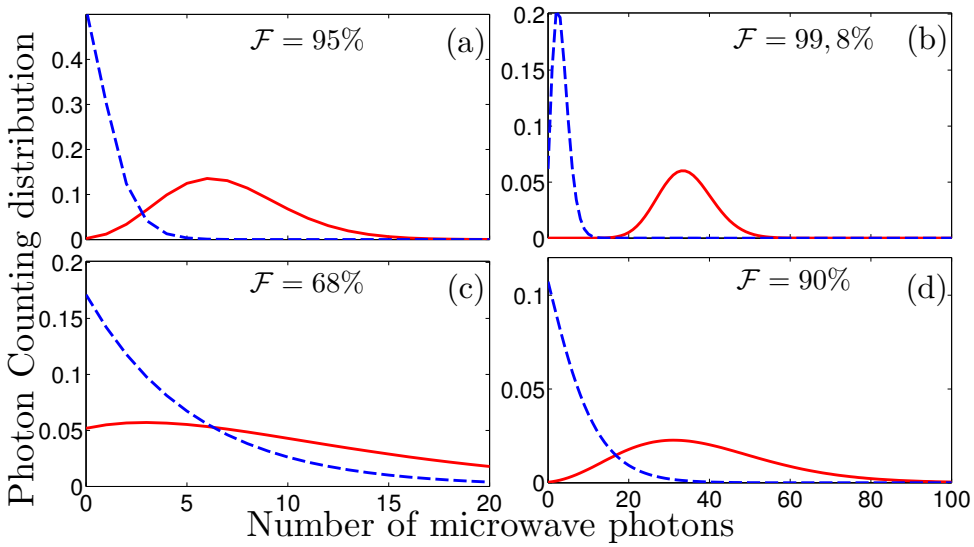

Figure 5.6: Photon distribution at the entrance of the amplifier. Histograms $\mathbf{P}(n|e)$ (red solid) and $\mathbf{P}(n|g)$ (blue dashed) with $\kappa = 40MHz$ and $p = 1photon/ns$. (a) $T_N = 140$mK, $\tau = 10$ns, $B = 50$MHz; (b) $T_N = 140$mK, $\tau = 50$ns, $B = 10$MHz; (c) $T_N = 4$K, $\tau = 10$ns, $B = 50$MHz; (d) $T_N = 4$K, $\tau = 50$ns, $B = 10$MHz.

been chosen, compatible with a bandwidth $B = 50$MHz. A fidelity $\mathcal{F} = 95\%$ can be reached with a resonator linewidth $\kappa = 50$ MHz and very small pumping power (see Fig. 5.6), corresponding to an intra-cavity population $\bar{n} = 1.8$ photons. This fidelity corresponds to up to date results obtained in the dispersive measurement scheme with the same amplifier [114, 125]. In these last cases still, the dynamics is one order of magnitude slower because of the inertia imposed by the resonator of linewidth $\kappa \sim 5$MHz, imposing a typical correlation time of $\tau_c = 100$ns.

The fidelity of the readout can be increased to the price of an increased measurement time, by performing a sequence of q independent measurements. In this approach, recording uncorrelated outcomes allows for exponentially fast convergence to arbitrarily high measurement fidelity. The optimal way to update the conditional probabilities of having the qubits in $|g\rangle$ or $|e\rangle$ is simply to use the Bayes' rule [125, 9, 126] at each of the q measurements. To evaluate the fidelity

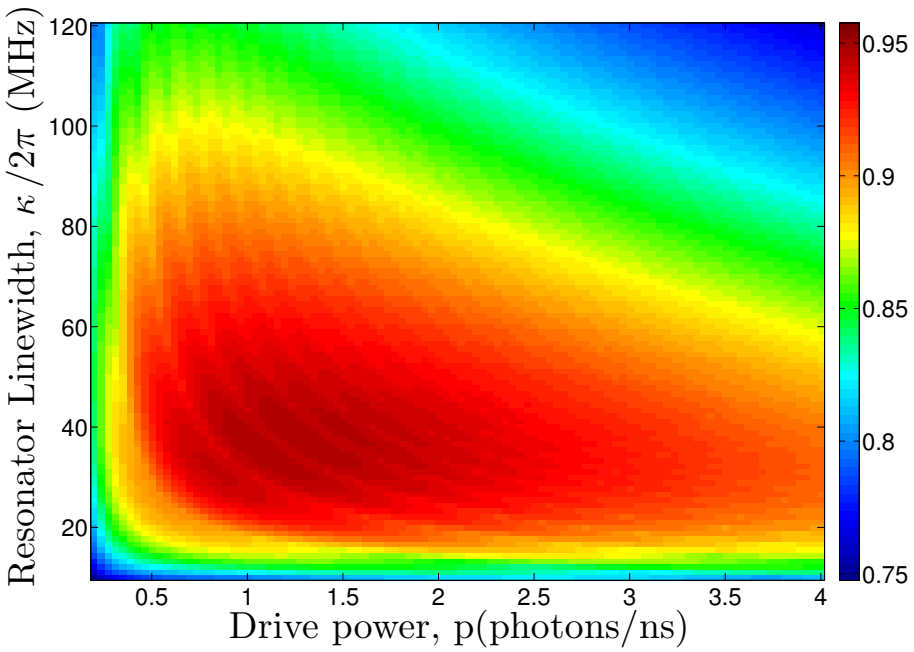

Figure 5.7: Single measurement fidelity for a state of the art amplifier (T_N = 140mK) and an acquisition time τ = 10 ns versus drive power p in units of photons/10ns and resonator linewidth κ. Optimal value of F= 95% is reached for broad range around $\kappa = 40$MHz and $p = 1 photon/ns$.

$\mathcal{F}$ after q steps we use Chernoff information [127],

$$C = -\inf_{0<\lambda<1} \log_2 \sum_n (\mathbf{P}(n|g))^{1-\lambda} (\mathbf{Pr}(n|e))^{\lambda}, \tag{5.16}$$

which bounds asymptotically the misclassifying error probability $\mathcal{E} = 1 - \mathcal{F}$ after q steps as $\mathcal{E} \leq 2^{-qC}$. With a commercial amplifier, the optimal value $C = 1.2$ is obtained after 50ns, which translates into a fidelity of $99,9\%$ after 8 integrations, i.e. 400ns. In the case of a state-of-the-art amplifier we can reach $C = 1.8$ after only 10ns, yielding $99,9\%$ after 60ns. We plot the Chernoff information as a function of drive power and cavity linewidth in Fig. 5.8. The proposed scheme, using low temperature amplifier allows to drastically increase the bandwidth and the speed of the readout and to perform projective measurement of the qubit on a timescale much shorter that the recent measured relaxation time, $T_1 = 50\mu s$ [42].

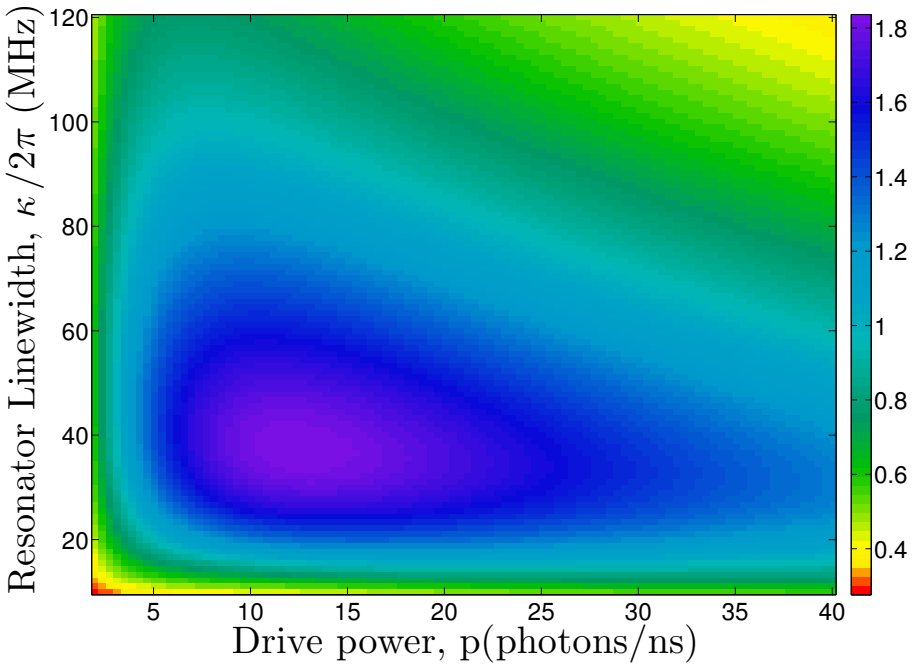

Figure 5.8: Chernoff information between the distributions associated with each logical qubit state ($|g\rangle$, $|e\rangle$) for a state of the art amplifier ($T_N = 140$mK) and an acquisition time $\tau = 10$ ns versus drive power p in units of photons/10ns and resonator linewidth κ. For broad range around $\kappa = 40$MHz and $p = 1 photon/ns$ we have C> 1.8.

This scheme opens the path to the observation of quantum jumps in circuit QED with a very high temporal resolution, comparable to the performances of recent experiments performed with Rydberg atoms [5], where the system is typically measured 10^3 times before undergoing a quantum jump.

In conclusion we propose a new read-out scheme based on a superconducting diamond shape artificial atom which contains a transmon qubit strongly coupled to an ancilla qubit by a cross-Kerr term. The intrinsic properties of such an atom are used to amplify the quantum measurements performances. We show high fidelity fast QND read-out of the transmon qubit with commercial amplifier. Using quantum limited amplifier, 60 ns read-out time and 99.9% fidelity are predicted. This original method overcomes the current read-out limitation of the superconducting qubits based on high Q resonators and small amplification

bandwidth. As a side effect the intra-cavity population is minimal, $\bar{n} = 1.8$ for the optimal parameters, minimizing any adverse effect on the qubit coherence properties. This opens the way to the monitoring of the quantum jumps of the qubit with very high temporal resolution, to the generation of non-classical states [128] or the implementation of quantum error correction codes [15] using closed feedback loops.

Chapter 6

Conclusion and Perspectives

We presented the theoretical description of superconducting circuits based on Josephson junctions, beginning with a simple theoretical description for the physics of superconducting circuits to obtain the Hamiltonian of a generic circuit. We revisited some of the typical circuits showing how they can yield the three basic Josephson qubits. We discussed how these qubits couple to resonators and how these resonators interact with external control pulses. This is the theoretical framework in which all the thesis is based.

We investigated theoretically the coupling of a cavity mode to a continuous distribution of emitters, discussing the influence of the emitters inhomogeneous broadening on the existence and on the coherence properties of the polaritonic peaks. We found that their coherence depends crucially on the shape of the distribution and not only on its width. Under certain conditions the coupling to the cavity protects the polaritonic states from inhomogeneous broadening, resulting in a longer storage time for a quantum memory based on emitters ensembles. A direct perspective in this subject is the search of protocols which could alleviate the short storage time imposed by the inhomogeneous broadening. Spin echo techniques can be used in principle but they require a new theoretical approach as the spin ensemble will not be restricted to a few excitations anymore.

We showed that taking into account the inhomogeneous broadening it is possible to simulate successfully a number of pioneer experimental results on a hybrid circuit based on an ensemble of NV centers. Both spectroscopical and dynamical signals were simulated culminating with a high sensibility spin spectroscopy

where unexpected features were reproduced. The modeling has been shown to be a powerful tool to obtain the properties of the spin ensembles coupled to a resonator. This will hopefully serve as a guide for the next generation of samples in the pursuit of better coherence properties.

We studied theoretically the transmitted microwave signal of a resonator coupled to a diamond-shape artificial atom. We showed how this level scheme appears in high inductance dc-SQUID and identified logical and ancilla qubits coupled through a cross-Kerr like term. We investigated how the transmission through the resonator depends on the qubit state, showing that the ancilla goes from resonant to the dispersive regime leading to a large contrast in the transmitted microwave signal amplitude. We evaluated the performance of this device in measuring the logical qubit state taking into account experimental amplification noise and realistic circuit parameters. Simulations show that this original method can be faster and have higher fidelity than currently used methods. As a short-term perspective, the scheme should be optimized to work in reflection geometry where instead of the difference in the transmitted power the states could be distinguished by the phase of the reflected field. More generally other Josephson qubits could exploit a similar readout method based on the diamond level-scheme.

We consider the work presented in this thesis to be a contribution, although modest, to the circuit quantum electrodynamics framework in which it is inserted.

Appendix A

Appendix A

Supplementary material for Chapter 3 .

A.1 Dynamics

In this part, we establish the link between the complex transmission of the cavity, and the evolution of the system if the mode a is initially fed with a single photon. This evolution is governed by the set of equations (3.3) written in the free frame ($\omega = 0$). The input fields are in the vacuum, the state of the system is $|1, G\rangle = a^\dagger(0)\,|0\rangle$ where $|0\rangle$ is the ground state of the total system. We are interested in the quantities $\langle a(t)a^\dagger(0)\rangle$ and $\langle b_k(t)a^\dagger(0)\rangle$, which represent the probability amplitude of the excitation in the cavity mode and in each emitter respectively, as it will appear later. The average values are taken in state $|0\rangle$. We get

$$\begin{aligned}\langle \dot{a}(t)a^\dagger(0)\rangle &= -\left(\kappa/2 + i\omega_0\right)\langle a(t)a^\dagger(0)\rangle + \sum_k g_k\langle b_k(t)a^\dagger(0)\rangle \\ \langle \dot{b_k}(t)a^\dagger(0)\rangle &= -\left(\gamma/2 + i\omega_k\right)\langle b_k(t)a^\dagger(0)\rangle - g_k\langle a(t)a^\dagger(0)\rangle\end{aligned} \tag{A.1}$$

Defining the vector $|\psi\rangle$ of coordinates $(\langle a(t)a^\dagger(0)\rangle, ..., \langle b_k(t)a^\dagger(0)\rangle, ...)$, its evolution simply follows the Schrödinger like equation $\hbar\dfrac{d}{dt}\,|\psi\rangle\,(t) = -iH_{eff}\,|\psi\rangle\,(t)$,

with

$$H_{eff}/\hbar = \begin{pmatrix} \tilde{\omega}_0 & ig_1 & ig_2 & \dots \\ -ig_1 & \tilde{\omega}_1 & & \\ -ig_2 & & \tilde{\omega}_2 & \\ \vdots & & & \ddots \end{pmatrix} . \tag{A.2}$$

We have used the complex frequencies for the cavity $\tilde{\omega}_0$ and for the emitters $\tilde{\omega}_k$ defined above. Note that these results are in full agreement with the ones obtained in the Green function formalism by Kurucz et al [70]. It appears that the dynamics of the problem can be modeled with the effective Hamiltonian H_{eff}. In particular, one can define an effective evolution operator $O(t) = e^{iH_{eff}t/\hbar} O e^{-iH_{eff}t/\hbar}$, such that $\langle a(t)a^\dagger(0)\rangle = \langle 0| a(0)e^{-iH_{eff}t/\hbar}a^\dagger(0)|0\rangle$. This quantity can be rewritten $\langle 1,G| e^{-iH_{eff}t/\hbar} |1,G\rangle$, justifying that we talk of the probability amplitude of the excitation in the cavity mode, starting from the initial state $|1,G\rangle$. The problem is solved using e.g. standard Laplace transform method. Defining $\mathcal{L}(f(t)) = F(s) = \int_0^\infty \exp(st) f(t) dt$, we have

$$|\psi(t)\rangle = \mathcal{L}^{-1}\left((s + iH_{eff}/\hbar)^{-1} |\psi(0)\rangle\right) , \tag{A.3}$$

where we have used the Laplace transform property: $\mathcal{L}\{\frac{d}{dt}|\psi(t)\rangle\} = s|\Psi(s)\rangle - |\psi(0)\rangle$. We finally define $t_1(s) = \langle 1,G| (s + iH_{eff}/\hbar)^{-1} |1,G\rangle$. Inverse Laplace transform of this coefficient gives back the quantity $\langle 1,G| e^{-iH_{eff}/\hbar t} |1,G\rangle$. We easily get

$$t_1(s) = \frac{1}{s + i\tilde{\omega}_0 + \sum_k \frac{g_k^2}{s+i\tilde{\omega}_k}} , \tag{A.4}$$

From eq.(3.5) and eq.(A.4), we finally write the link between the transmission coefficient in amplitude $t(\omega)$ and the coefficient $t_1(s)$ characterizing the dynamics

of the system,

$$t(\omega) = -\frac{\kappa}{2} t_1(-i\omega)\,. \tag{A.5}$$

This establishes the relation between the amplitude $\alpha_1(t) = \langle 1, G|\, e^{-iH_{eff}t/\hbar}\, |1, G\rangle$ and the transmission $t(\omega)$ as:

$$\int_0^\infty \alpha_1(t) e^{i\omega t} dt = -\frac{2}{\kappa} t(\omega)\,. \tag{A.6}$$

One can use the method exposed above to compute the expression of the probability amplitude for a state initially prepared in $\left|\psi_+^0(\delta)\right\rangle$, namely $\left\langle\psi_+^0(\delta)\right|\, e^{-iH_{eff}t/\hbar}\, \left|\psi_+^0(\delta)\right\rangle$ studied in Section 3.5. In general, we can decompose it as

$$\begin{aligned}
&\left\langle\psi_+^0(\delta)\right|\, U_{eff}(t)\, \left|\psi_+^0(\delta)\right\rangle = \\
&= \cos^2(\theta/2)\, \langle 1, G|\, U_{eff}\, |1, G\rangle + \sin^2(\theta/2)\, \langle 0, S|\, U_{eff}\, |0, S\rangle + \\
&+ i \sin(\theta/2)\cos(\theta/2)\, (\langle 0, S|\, U_{eff}\, |1, G\rangle - \langle 1, G|\, U_{eff}\, |0, S\rangle) \\
&= \cos^2(\theta/2)\alpha_1(t) + \sin^2(\theta/2)\alpha_2(t) + \\
&+ i \sin(\theta/2)\cos(\theta/2)\, (\alpha_3(t) - \alpha_4(t))\ ,
\end{aligned} \tag{A.7}$$

where $U_{eff}(t) \equiv e^{-iH_{eff}t/\hbar}$.

We need only to calculate the four matrix elements $\alpha_i(t)$. Defining $t_i(s) = \mathcal{L}(\alpha_i(t))$ we obtain in the case of a continuous distribution,

$$\begin{aligned}
t_2(s) &= -\frac{W(is)}{\Omega^2} t_1(s)(s + i\tilde{\omega_o}) \\
t_3(s) &= t_1(s)\frac{iW(is)}{\Omega} \\
t_4(s) &= -t_3(s)\,.
\end{aligned} \tag{A.8}$$

A.2 $W(\omega)$ for specific distributions

We now evaluate the function $W(\omega)$ for all the specific continua analyzed in the paper. This function allows the evaluation of the complex transmission using $t(\omega) = (\kappa/2i)(\omega - \omega_0 + i\kappa/2 - W(\omega))^{-1}$, but also appears in other formulae.

Gaussian

The Gaussian distribution writes $\rho(\omega) = \frac{\sqrt{\ln 2}}{\Delta\sqrt{\pi}} e^{-(\omega^2 \ln 2)/\Delta^2}$. $W(\omega)$ is thus,

$$W_G(\omega) = \frac{1}{i}\frac{\sqrt{\ln 2}\,\Omega^2}{\Delta}\sqrt{\pi}\left(\frac{i}{\pi}\int_{-\infty}^{\infty}\frac{d\omega' e^{-\omega'^2}}{\left(\frac{\omega+i\gamma/2}{\Delta/\sqrt{\ln 2}} - \omega'\right)}\right). \tag{A.9}$$

Remembering that

$$\frac{i}{\pi}\int_{-\infty}^{\infty} d\omega' \frac{e^{-\omega'^2}}{z-\omega'} = e^{-z^2}\,\mathrm{erfc}(-iz) \tag{A.10}$$

where erfc is the complex complementary error function, it comes

$$W_G(\omega) = -i\frac{\sqrt{\ln 2}\,\Omega^2}{\Delta}\sqrt{\pi} e^{-(\frac{\omega+i\gamma/2}{\Delta/\sqrt{\ln 2}})^2}\,\mathrm{erfc}\left(-i\frac{\omega+i\gamma/2}{\Delta/\sqrt{\ln 2}}\right). \tag{A.11}$$

Rectangular

In the case of a rectangular distribution, the density of emitter is $\rho(\omega) = \frac{1}{\Delta}(\Theta(\omega - \Delta/2) - \Theta(\omega + \Delta/2))$ we have

$$W_R(\omega) = \frac{2\Omega^2}{i\Delta}\,\mathrm{ArcTan}\left(\frac{\Delta}{\gamma - 2i\omega}\right). \tag{A.12}$$

Lorentzian

The density of emitter is $\rho(\omega) = \frac{\Delta/2}{\pi}\frac{1}{(\Delta/2)^2+\omega^2}$, thus

$$W_L(\omega) = \frac{\Omega^2}{\omega + i\gamma/2 + i\Delta/2}\,. \tag{A.13}$$

From the equation above we see that for Lorentz distribution we do not achieve cavity protection, i.e. the inhomogeneous broadening always contributes as if it were homogeneous.

A.3 Development with finite γ

We start rewrite $W(\omega)$ from eq.(3.6) as

$$\begin{aligned} W(\omega) = \Omega^2 \int_{-\infty}^{\infty} d\omega' \frac{\omega'^2}{\omega'^2+\gamma^2}\frac{\rho(\omega'+\omega)}{\omega'} - \\ -i\pi\Omega^2 \int_{-\infty}^{\infty} d\omega' \frac{\gamma}{\pi(\omega'^2+\gamma^2)}\rho(\omega+\omega')\,. \end{aligned} \tag{A.14}$$

The integrands contain products of a function of width γ and another with width Δ. If $\gamma \ll \Delta$, the integrals take the form:

$$\begin{aligned} W(\omega) = \Omega^2 P\!\int_{-\infty}^{\infty} \frac{\rho(\omega')d\omega'}{\omega-\omega'} - \\ -\,i\Omega^2\left(\pi\rho(\omega) + \frac{\gamma}{2}\,P\!\int_{-\infty}^{\infty}\frac{\rho(\omega')d\omega'}{(\omega-\omega')^2}\right)\,. \end{aligned} \tag{A.15}$$

We are interested in the development of $W(\omega)$ near the poles of the transmission function in the absence of inhomogeneous broadening, namely $\omega \sim \Omega$.

Denoting $r = \omega'/\omega$, and using the identity $\sum r^k = 1/(1-r)$, we find :

$$\begin{aligned} W(\omega) = \frac{\Omega^2}{\omega}\left(1 + \sum_{k=1}^{\infty}\frac{\mu_k}{\omega^k} - i\pi\rho(\omega)\right) - \\ - i\frac{\Omega^2}{\omega^2}\frac{\gamma}{2}\left(1 + \sum_{k=1}^{\infty}(k+1)\frac{\mu_k}{\omega^k}\right), \end{aligned} \tag{A.16}$$

where μ_k is the k-th moment of the distribution $\rho(\omega)$ about its origin

$$\mu_k \equiv \int_{-\infty}^{\infty} d\omega\rho(\omega)\omega^k \,. \tag{A.17}$$

Note that this development is only valid if $\omega \gg \omega'$, which is the case in the present study as $\omega \sim \Omega \gg \Delta > \omega'$. From the normalization and considering only symmetric distributions, we have $\mu_0 = 1$ and $\mu_1 = 0$. μ_2 gives the first non-zero correction and it is typically proportional to the square of the FWHM (as an example, $\mu_2 = \Delta^2/(2\ln 2)$ in the case of a Gaussian distribution). To first non-zero correction we have:

$$\begin{aligned} W(\omega) &= \frac{\Omega^2}{\omega}(1 + \mu_2/\omega^2) - i\left(\frac{\gamma}{2}\frac{\Omega^2}{\omega^2} + \pi\Omega^2\rho(\omega)\right) \\ &= \frac{\Omega^2(1+\mu_2/\omega^2)}{\omega + i\gamma/2} - i\pi\Omega^2\rho(\omega)\,, \end{aligned} \tag{A.18}$$

where we have used $\Omega \gg \gamma$. One easily infers the modifications to the transmission poles induced by inhomogeneous broadening. They are located at

$$\omega_{\pm} = \pm\Omega\sqrt{1 + \mu_2/\Omega^2 - \left(\frac{\kappa + 2\pi\rho(\Omega)\Omega^2 - \gamma}{4\Omega}\right)^2}. \tag{A.19}$$

Their width check $\Gamma = \frac{\kappa+\gamma+2\pi\Omega^2\rho(\Omega)}{2}$, in correspondence with what stated in Sec. 3.2. Note that this procedure is only valid for distribution with well defined

moments. This is not the case of the Lorentzian, nevertheless $W(\omega)$ can be exactly evaluated in this case. The exact calculations for the 3 cases taken under consideration are the subject of appendix A.2.

A.4 Two ways to obtain the temporal evolution

We have found two ways to evaluate $\alpha_1(t) = \langle 1, G| \, e^{-iH_{eff}t/\hbar} \, |1, G\rangle$, the first at Appendix A.1 uses a Laplace-Fourier transform of $-t(\omega)/(\kappa/2)$ the second uses the standard Fourier transform of $2\pi\Omega^2 \, \rho(\omega) \, |t(\omega)/(\kappa/2)|^2$ for $\kappa, \gamma \to 0$ as in Sec. 3.3. The first way is more general in the sense that it can include emitter and cavity radiative losses, the second describe a reversible process originated in a Hamiltonian evolution. We now show that both ways coincide when we disregard losses.

From Appendix A.1 we have

$$\int_0^\infty \alpha_1(t) e^{i\omega t} dt = t_1(-i\omega) \,, \tag{A.20}$$

where, if $\gamma, \kappa \to 0$

$$t_1(-i\omega) = \frac{i}{\omega - \omega_0 - \Omega^2 P\!\int \frac{\rho(\omega')d\omega'}{\omega - \omega'} + i\pi\Omega^2\rho(\omega)} \,. \tag{A.21}$$

We now take the real part of eqs.(A.20 , A.21) , yielding

$$\begin{aligned} &\Re\left\{\int_0^\infty \alpha_1(t) e^{i\omega t} dt\right\} = \\ &= \Re\left\{\frac{i}{\omega - \omega_0 - \Omega^2 P\!\int \frac{\rho(\omega')d\omega'}{\omega - \omega'} + i\pi\Omega^2\rho(\omega)}\right\} \\ &= \pi\Omega^2\rho(\omega)|t_1|^2 \,, \end{aligned} \tag{A.22}$$

if we consider time reversibility of the lossless dynamics we have $\alpha_1(-t) =$

$(\alpha_1(t))^*$ and thus

$$\begin{aligned} &2\Re\left\{\int_0^\infty \alpha_1(t)e^{i\omega t}dt\right\} = \\ &= \int_0^\infty (\alpha_1(t)e^{i\omega t} + \alpha_1^*(t)e^{-i\omega t})dt \\ &= \int_{-\infty}^\infty \alpha_1(t)e^{i\omega t}dt\,. \end{aligned} \tag{A.23}$$

Eq.(A.22) and eq.(A.23) together give

$$\int_{-\infty}^\infty \alpha_1(t)e^{i\omega t}dt = 2\pi\Omega^2\ \rho(\omega)\,|t_1|^2\ , \tag{A.24}$$

which is precisely what we find applying the inverse Fourier transform in eq.(3.21). Note we had to use the time-reversibility which is only valid in the lossless case.

References

[1] P. Goy, J. M. Raimond, M. Gross, and S. Haroche. Observation of cavity-enhanced single-atom spontaneous emission. *Phys. Rev. Lett.*, 50:1903–1906, Jun 1983. 1

[2] Y. Kaluzny, P. Goy, M. Gross, J. M. Raimond, and S. Haroche. Observation of self-induced rabi oscillations in two-level atoms excited inside a resonant cavity: The ringing regime of superradiance. *Phys. Rev. Lett.*, 51:1175–1178, Sep 1983. 1, 2, 33

[3] Serge Haroche and Jean Michel Raimond. *Exploring the Quantum: Atoms, Cavities, and Photons*. Oxford Univ. Press, Oxford, 2006. 1, 4, 84

[4] J. M. Raimond, M. Brune, and S. Haroche. Manipulating quantum entanglement with atoms and photons in a cavity. *Rev. Mod. Phys.*, 73:565–582, Aug 2001. 2

[5] Sebastien Gleyzes, Stefan Kuhr, Christine Guerlin, Julien Bernu, Samuel Deleglise, Ulrich Busk Hoff, Michel Brune, Jean-Michel Raimond, and Serge Haroche. Quantum jumps of light recording the birth and death of a photon in a cavity. *Nature*, 446(7133):297–300, March 2007. 2, 102

[6] Andrew C. Doherty, Salman Habib, Kurt Jacobs, Hideo Mabuchi, and Sze M. Tan. Quantum feedback control and classical control theory. *Phys. Rev. A*, 62:012105, Jun 2000. 2

[7] X. Zhou, I. Dotsenko, B. Peaudecerf, T. Rybarczyk, C. Sayrin, S. Gleyzes, J. M. Raimond, M. Brune, and S. Haroche. Field locked to a fock state by quantum feedback with single photon corrections. *Phys. Rev. Lett.*, 108:243602, Jun 2012. 2

[8] G. Nogues, A. Rauschenbeutel, S. Osnaghi, M. Brune, J. M. Raimond, and S. Haroche. Seeing a single photon without destroying it. *Nature*, 400(6741):239–242, July 1999. 2

[9] Christine Guerlin, Julien Bernu, Samuel Deleglise, Clement Sayrin, Sebastien Gleyzes, Stefan Kuhr, Michel Brune, Jean-Michel Raimond, and Serge Haroche. Progressive field-state collapse and quantum non-demolition photon counting. *Nature*, 448(7156):889–893, August 2007. 2, 100

[10] Charles H. Bennett and David P. DiVincenzo. Quantum information and computation. *Nature*, 404(6775):247–255, March 2000. 3

[11] Peter W. Shor. Polynomial-time algorithms for prime factorization and discrete logarithms on a quantum computer. *SIAM J. Comput.*, 26(5):1484–1509, 1997. 3

[12] Lov K. Grover. Quantum mechanics helps in searching for a needle in a haystack. *Phys. Rev. Lett.*, 79:325–328, Jul 1997. 3

[13] Frederic Grosshans, Gilles Van Assche, Jerome Wenger, Rosa Brouri, Nicolas J. Cerf, and Philippe Grangier. Quantum key distribution using gaussian-modulated coherent states. *Nature*, 421(6920):238–241, January 2003. 3

[14] Marco Tomamichel, Charles Ci Wen Lim, Nicolas Gisin, and Renato Renner. Tight finite-key analysis for quantum cryptography. *Nat Commun*, 3:634–, January 2012. 3

[15] Michael A. Nielsen and Isaac L. Chuang. *Quantum Computation and Quantum Information (Cambridge Series on Information and the Natural Sciences)*. Cambridge University Press, 2000. 3, 103

[16] Michael A. Nielsen. Quantum computation by measurement and quantum memory. *Physics Letters A*, 308(2âĂŞ3):96 – 100, 2003. 3, 87

[17] H. J. Briegel, D. E. Browne, W. Dur, R. Raussendorf, and M. Van den Nest. Measurement-based quantum computation. *Nat Phys*, 1:19–26, January 2009. 3, 87

[18] Mikio Nakahara and Martti M. Salomaa. *DiVincenzo Criteria and Beyond*, chapter 2, pages 3–15. 2004. 3

[19] Alexandre Blais, Ren-Shou Huang, Andreas Wallraff, S. M. Girvin, and R. J. Schoelkopf. Cavity quantum electrodynamics for superconducting electrical circuits: An architecture for quantum computation. *Phys. Rev. A*, 69:062320, Jun 2004. 4, 25, 60

[20] A. Wallraff, D. I. Schuster, A. Blais, L. Frunzio, R.-S. Huang, J. Majer, S. Kumar, S. M. Girvin, and R. J. Schoelkopf. Strong coupling of a single photon to a superconducting qubit using circuit quantum electrodynamics. *Nature*, 431(7005):162–167, September 2004. 4, 25, 54

[21] I. Chiorescu, P. Bertet, K. Semba, Y. Nakamura, C. J. P. M. Harmans, and J. E. Mooij. Coherent dynamics of a flux qubit coupled to a harmonic oscillator. *Nature*, 431(7005):159–162, September 2004. 4

[22] Max Hofheinz, E. M. Weig, M. Ansmann, Radoslaw C. Bialczak, Erik Lucero, M. Neeley, A. D. O/'Connell, H. Wang, John M. Martinis, and A. N. Cleland. Generation of fock states in a superconducting quantum circuit. *Nature*, 454(7202):310–314, July 2008. 4

[23] Max Hofheinz, H. Wang, M. Ansmann, Radoslaw C. Bialczak, Erik Lucero, M. Neeley, A. D. O'Connell, D. Sank, J. Wenner, John M. Martinis, and A. N. Cleland. Synthesizing arbitrary quantum states in a superconducting resonator. *Nature*, 459(7246):546–549, May 2009. 4, 5

[24] J. Bardeen, L. N. Cooper, and J. R. Schrieffer. Microscopic theory of superconductivity. *Phys. Rev.*, 106:162–164, Apr 1957. 8

[25] To be published. *Quantum machines: measurement and control of engineered quantum systems*. Les Houches Summer Session Series. Oxford University Press., 2012. 8, 27

[26] B.D. Josephson. Possible new effects in superconductive tunnelling. *Physics Letters*, 1(7):251 – 253, 1962. 10

[27] A. A. Golubov, M. Yu. Kupriyanov, and E. Il'ichev. The current-phase relation in josephson junctions. *Rev. Mod. Phys.*, 76:411–469, Apr 2004. 10, 11

[28] W. Meissner and R. Ochsenfeld. Ein neuer effekt bei eintritt der supraleitfÃd'higkeit. *Naturwissenschaften*, 21:787–788, 1933. 10.1007/BF01504252. 12

[29] Fritz London. *Superfluids, Volume 1, Macroscopic Theory of Super Conductivity*. Chapman and Hall, 1950. 12

[30] M. H. Devoret. Quantum fluctuations in electrical circuits. *Les Houches Session LXIII, Quantum Fluctuations*, 1:351–386, 1995. 14, 21

[31] Bernard Yurke and John S. Denker. Quantum network theory. *Phys. Rev. A*, 29:1419–1437, Mar 1984. 14

[32] V Bouchiat, D Vion, P Joyez, D Esteve, and M H Devoret. Quantum coherence with a single cooper pair. *Physica Scripta*, 1998(T76):165, 1998. 15

[33] Y. Nakamura, Yu. A. Pashkin, and J. S. Tsai. Coherent control of macroscopic quantum states in a single-cooper-pair box. *Nature*, 398(6730):786–788, April 1999. 15, 21

[34] D. Vion, A. Aassime, A. Cottet, P. Joyez, H. Pothier, C. Urbina, D. Esteve, and M. H. Devoret. Manipulating the quantum state of an electrical circuit. *Science*, 296(5569):886–889, 2002. 16

[35] K Bladh, T Duty, D Gunnarsson, and P Delsing. The single cooper-pair box as a charge qubit. *New Journal of Physics*, 7(1):180, 2005. 16

[36] Jens Koch, Terri M. Yu, Jay Gambetta, A. A. Houck, D. I. Schuster, J. Majer, Alexandre Blais, M. H. Devoret, S. M. Girvin, and R. J. Schoelkopf. Charge-insensitive qubit design derived from the cooper pair box. *Phys. Rev. A*, 76:042319, Oct 2007. 16

[37] Jens Koch, Terri M. Yu, Jay Gambetta, A. A. Houck, D. I. Schuster, J. Majer, Alexandre Blais, M. H. Devoret, S. M. Girvin, and R. J. Schoelkopf. Charge-insensitive qubit design derived from the cooper pair box. *Phys. Rev. A*, 76:042319, Oct 2007. 17

[38] John M. Martinis, S. Nam, J. Aumentado, and C. Urbina. Rabi oscillations in a large josephson-junction qubit. *Phys. Rev. Lett.*, 89:117901, Aug 2002. 19

[39] O. Buisson, F. Balestro, J. P. Pekola, and F. W. J. Hekking. One-shot quantum measurement using a hysteretic dc squid. *Phys. Rev. Lett.*, 90:238304, Jun 2003. 20

[40] S M Girvin, M H Devoret, and R J Schoelkopf. Circuit qed and engineering charge-based superconducting qubits. *Physica Scripta*, 2009(T137):014012, 2009. 20

[41] G. Wendin and V. S. Shumeiko. Quantum bits with josephson junctions (review article). *Low Temperature Physics*, 33(9):724–744, 2007. 20

[42] Hanhee Paik, D. I. Schuster, Lev S. Bishop, G. Kirchmair, G. Catelani, A. P. Sears, B. R. Johnson, M. J. Reagor, L. Frunzio, L. I. Glazman, S. M. Girvin, M. H. Devoret, and R. J. Schoelkopf. Observation of high coherence in josephson junction qubits measured in a three-dimensional circuit qed architecture. *Phys. Rev. Lett.*, 107:240501, Dec 2011. 21, 101

[43] Antonio D. Corcoles, Jerry M. Chow, Jay M. Gambetta, Chad Rigetti, J. R. Rozen, George A. Keefe, Mary Beth Rothwell, Mark B. Ketchen, and M. Steffen. Protecting superconducting qubits from radiation. *Applied Physics Letters*, 99(18):181906, 2011. 21

[44] John M. Martinis, K. B. Cooper, R. McDermott, Matthias Steffen, Markus Ansmann, K. D. Osborn, K. Cicak, Seongshik Oh, D. P. Pappas, R. W. Simmonds, and Clare C. Yu. Decoherence in josephson qubits from dielectric loss. *Phys. Rev. Lett.*, 95:210503, Nov 2005. 21

[45] A. A. Clerk, M. H. Devoret, S. M. Girvin, Florian Marquardt, and R. J. Schoelkopf. Introduction to quantum noise, measurement, and amplification. *Rev. Mod. Phys.*, 82:1155–1208, Apr 2010. 21, 88

[46] A. Palacios-Laloy, F. Nguyen, F. Mallet, P. Bertet, D. Vion, and D. Esteve. Tunable resonators for quantum circuits. *Journal of Low Temperature Physics*, 151:1034–1042, 2008. 10.1007/s10909-008-9774-x. 23, 24, 25

[47] C. W. Gardiner and M. J. Collett. Input and output in damped quantum systems: Quantum stochastic differential equations and the master equation. *Phys. Rev. A*, 31:3761–3774, Jun 1985. 27, 36

[48] D. F. Walls and G. J. Milburn. *Quantum Optics*. Springer, 1994. 27

[49] R. J. Thompson, G. Rempe, and H. J. Kimble. Observation of normal-mode splitting for an atom in an optical cavity. *Phys. Rev. Lett.*, 68:1132–1135, Feb 1992. 33

[50] F. Bernardot, P. Nussenzveig, M. Brune, J. M. Raimond, and S. Haroche. Vacuum rabi splitting observed on a microscopic atomic sample in a microwave cavity. *EPL (Europhysics Letters)*, 17(1):33, 1992. 33

[51] C. Weisbuch, M. Nishioka, A. Ishikawa, and Y. Arakawa. Observation of the coupled exciton-photon mode splitting in a semiconductor quantum microcavity. *Physical Review Letters*, 69(23):3314–3317, 1992. 33

[52] C. B. Murray, C. R. Kagan, and M. G. Bawendi. Self-organization of cdse nanocrystallites into three-dimensional quantum dot superlattices. *Science*, 270(5240):1335–1338, 1995. 33, 37

[53] J. Y. Marzin, J. M. Gérard, A. Izraël, D. Barrier, and G. Bastard. Photoluminescence of single inas quantum dots obtained by self-organized growth on gaas. *Phys. Rev. Lett.*, 73:716–719, Aug 1994. 33, 37

[54] AurÃľlien A. L. Nicolet, Clemens Hofmann, Mikhail A. Kol'chenko, Boleslaw Kozankiewicz, and Michel Orrit. Single dibenzoterrylene molecules in an anthracene crystal: Spectroscopy and photophysics. *ChemPhysChem*, 8(8):1215–1220, 2007. 33, 37, 64

[55] Atac Imamoglu. Cavity qed based on collective magnetic dipole coupling: Spin ensembles as hybrid two-level systems. *Phys. Rev. Lett.*, 102:083602, Feb 2009. 33, 34

[56] J. Verdú, H. Zoubi, Ch. Koller, J. Majer, H. Ritsch, and J. Schmiedmayer. Strong magnetic coupling of an ultracold gas to a superconducting waveguide cavity. *Phys. Rev. Lett.*, 103:043603, Jul 2009. 34

[57] P. Rabl, D. DeMille, J. M. Doyle, M. D. Lukin, R. J. Schoelkopf, and P. Zoller. Hybrid quantum processors: Molecular ensembles as quantum memory for solid state circuits. *Phys. Rev. Lett.*, 97:033003, Jul 2006. 34

[58] J. H. Wesenberg, A. Ardavan, G. A. D. Briggs, J. J. L. Morton, R. J. Schoelkopf, D. I. Schuster, and K. Mølmer. Quantum computing with an electron spin ensemble. *Phys. Rev. Lett.*, 103:070502, Aug 2009. 34, 53

[59] Y. Kubo, F. R. Ong, P. Bertet, D. Vion, V. Jacques, D. Zheng, A. Dréau, J.-F. Roch, A. Auffeves, F. Jelezko, J. Wrachtrup, M. F. Barthe, P. Bergonzo, and D. Esteve. Strong coupling of a spin ensemble to a superconducting resonator. *Phys. Rev. Lett.*, 105:140502, Sep 2010. 34, 48, 50, 54

[60] D. I. Schuster, A. P. Sears, E. Ginossar, L. DiCarlo, L. Frunzio, J. J. L. Morton, H. Wu, G. A. D. Briggs, B. B. Buckley, D. D. Awschalom, and R. J. Schoelkopf. High-cooperativity coupling of electron-spin ensembles to superconducting cavities. *Phys. Rev. Lett.*, 105:140501, Sep 2010. 34, 54

[61] Janus H. Wesenberg, Zoltan Kurucz, and Klaus Mølmer. Dynamics of the collective modes of an inhomogeneous spin ensemble in a cavity. *Phys. Rev. A*, 83:023826, Feb 2011. 34

[62] R. H. Dicke. Coherence in spontaneous radiation processes. *Phys. Rev.*, 93:99–110, Jan 1954. 34, 61

[63] D. Hone, V. Jaccarino, Tin Ngwe, and P. Pincus. Microscopic inhomogeneous broadening and nuclear spin-spin interactions. *Phys. Rev.*, 186:291–305, Oct 1969. 37

[64] D L Orth, R J Mashl, and J L Skinner. Optical lineshapes of impurities in crystals: a lattice model of inhomogeneous broadening by point defects. *Journal of Physics: Condensed Matter*, 5(16):2533, 1993. 37

[65] Lucio Claudio Andreani, Giovanna Panzarini, and Jean-Michel Gérard. Strong-coupling regime for quantum boxes in pillar microcavities: Theory. *Phys. Rev. B*, 60:13276–13279, Nov 1999. 37

[66] Alexia Auffèves, Benjamin Besga, Jean-Michel Gérard, and Jean-Philippe Poizat. Spontaneous emission spectrum of a two-level atom in a very-high-q cavity. *Phys. Rev. A*, 77:063833, Jun 2008. 38

[67] R. Houdré, R. P. Stanley, and M. Ilegems. Vacuum-field rabi splitting in the presence of inhomogeneous broadening: Resolution of a homogeneous linewidth in an inhomogeneously broadened system. *Phys. Rev. A*, 53:2711–2715, Apr 1996. 38

[68] U. Fano. Effects of configuration interaction on intensities and phase shifts. *Phys. Rev.*, 124:1866–1878, Dec 1961. 40, 42

[69] Z. Kurucz, M. W. Sørensen, J. M. Taylor, M. D. Lukin, and M. Fleischhauer. Qubit protection in nuclear-spin quantum dot memories. *Phys. Rev. Lett.*, 103:010502, Jul 2009. 45

[70] Z. Kurucz, J. H. Wesenberg, and K. Mølmer. Spectroscopic properties of inhomogeneously broadened spin ensembles in a cavity. *Phys. Rev. A*, 83:053852, May 2011. 48, 108

[71] J. M. Fink, R. Bianchetti, M. Baur, M. Göppl, L. Steffen, S. Filipp, P. J. Leek, A. Blais, and A. Wallraff. Dressed collective qubit states and the tavis-cummings model in circuit qed. *Phys. Rev. Lett.*, 103:083601, Aug 2009. 48

[72] Tim Duty. Towards superconductor-spin ensemble hybrid quantum systems. *Physics*, 3:80, Sep 2010. 53

[73] Ph Tamarat, N B Manson, J P Harrison, R L McMurtrie, A Nizovtsev, C Santori, R G Beausoleil, P Neumann, T Gaebel, F Jelezko, P Hemmer, and J Wrachtrup. Spin-flip and spin-conserving optical transitions of the nitrogen-vacancy centre in diamond. *New Journal of Physics*, 10(4):045004, 2008. 54

[74] Gopalakrishnan Balasubramanian, Philipp Neumann, Daniel Twitchen, Matthew Markham, Roman Kolesov, Norikazu Mizuochi, Junichi Isoya, Jocelyn Achard, Johannes Beck, Julia Tissler, Vincent Jacques, Philip R. Hemmer, Fedor Jelezko, and Jorg Wrachtrup. Ultralong spin coherence time in isotopically engineered diamond. *Nat Mater*, 8(5):383–387, May 2009. 54

[75] L. Childress, M. V. Gurudev Dutt, J. M. Taylor, A. S. Zibrov, F. Jelezko, J. Wrachtrup, P. R. Hemmer, and M. D. Lukin. Coherent dynamics of coupled electron and nuclear spin qubits in diamond. *Science*, 314(5797):281–285, 2006. 54

[76] M.H. Devoret, Steven Girvin, and Robert Schoelkopf. Circuit-qed: How strong can the coupling between a josephson junction atom and a transmission line resonator be? *Annalen der Physik*, 16(10-11):767–779, 2007. 54

[77] Y. Kubo, I. Diniz, A. Dewes, V. Jacques, A. Dréau, J.-F. Roch, A. Auffeves, D. Vion, D. Esteve, and P. Bertet. Storage and retrieval of a microwave field in a spin ensemble. *Phys. Rev. A*, 85:012333, Jan 2012. 54, 56, 66, 72

[78] Y. Kubo, C. Grezes, A. Dewes, T. Umeda, J. Isoya, H. Sumiya, N. Morishita, H. Abe, S. Onoda, T. Ohshima, V. Jacques, A. Dréau, J.-F. Roch, I. Diniz, A. Auffeves, D. Vion, D. Esteve, and P. Bertet. Hybrid quantum circuit with a superconducting qubit coupled to a spin ensemble. *Phys. Rev. Lett.*, 107:220501, Nov 2011. 54, 56, 59, 61, 62

[79] Y. Kubo, I. Diniz, C. Grezes, T. Umeda, J. Isoya, H. Sumiya, T. Yamamoto, H. Abe, S. Onoda, T. Ohshima, V. Jacques, A. Dréau, J.-F. Roch, A. Auffeves, D. Vion, D. Esteve, and P. Bertet. Electron spin resonance detected by a superconducting qubit. *Phys. Rev. B*, 86:064514, Aug 2012. 55, 56

[80] L. Childress, J. M. Taylor, A. S. Sørensen, and M. D. Lukin. Fault-tolerant quantum communication based on solid-state photon emitters. *Phys. Rev. Lett.*, 96:070504, Feb 2006. 56

[81] J. M. Taylor, P. Cappellaro, L. Childress, L. Jiang, D. Budker, P. R. Hemmer, A. Yacoby, R. Walsworth, and M. D. Lukin. High-sensitivity diamond magnetometer with nanoscale resolution. *Nat Phys*, 4(10):810–816, October 2008. 56

[82] J. R. Maze, P. L. Stanwix, J. S. Hodges, S. Hong, J. M. Taylor, P. Cappellaro, L. Jiang, M. V. Gurudev Dutt, E. Togan, A. S. Zibrov, A. Yacoby, R. L. Walsworth, and M. D. Lukin. Nanoscale magnetic sensing with an individual electronic spin in diamond. *Nature*, 455(7213):644–647, October 2008. 56

[83] Thomas M. Babinec, HausmannBirgit J. M., Mughees Khan, Yinan Zhang, Jeronimo R. Maze, Philip R. Hemmer, and Marko Loncar. A diamond nanowire single-photon source. *Nat Nano*, 5(3):195–199, March 2010. 56

[84] Stefan Schietinger, Michael Barth, Thomas Aichele, and Oliver Benson. Plasmon-enhanced single photon emission from a nanoassembled metalâĹŠdiamond hybrid structure at room temperature. *Nano Letters*, 9(4):1694–1698, 2009. PMID: 19301860. 56

[85] Adam Gali. Theory of the neutral nitrogen-vacancy center in diamond and its application to the realization of a qubit. *Phys. Rev. B*, 79:235210, Jun 2009. 57

[86] J H N Loubser and J A van Wyk. Electron spin resonance in the study of diamond. *Reports on Progress in Physics*, 41(8):1201, 1978. 57

[87] M W Doherty, N B Manson, P Delaney, and L C L Hollenberg. The negatively charged nitrogen-vacancy centre in diamond: the electronic solution. *New Journal of Physics*, 13(2):025019, 2011. 57

[88] N.R.S. Reddy, N.B. Manson, and E.R. Krausz. Two-laser spectral hole burning in a colour centre in diamond. *Journal of Luminescence*, 38(1âĂŞ6):46 – 47, 1987. 57

[89] A. Lenef and S. C. Rand. Electronic structure of the n- V center in diamond: Theory. *Phys. Rev. B*, 53:13441–13455, May 1996. 57

[90] N. B. Manson, J. P. Harrison, and M. J. Sellars. Nitrogen-vacancy center in diamond: Model of the electronic structure and associated dynamics. *Phys. Rev. B*, 74:104303, Sep 2006. 57, 58

[91] Gopalakrishnan Balasubramanian, I. Y. Chan, Roman Kolesov, Mohannad Al-Hmoud, Julia Tisler, Chang Shin, Changdong Kim, Aleksander Wojcik, Philip R. Hemmer, Anke Krueger, Tobias Hanke, Alfred Leitenstorfer, Rudolf Bratschitsch, Fedor Jelezko, and Jorg Wrachtrup. Nanoscale imaging magnetometry with diamond spins under ambient conditions. *Nature*, 455(7213):648–651, October 2008. 58

[92] Benjamin Smeltzer, Jean McIntyre, and Lilian Childress. Robust control of individual nuclear spins in diamond. *Phys. Rev. A*, 80:050302, Nov 2009. 58

[93] S. Felton, A. M. Edmonds, M. E. Newton, P. M. Martineau, D. Fisher, D. J. Twitchen, and J. M. Baker. Hyperfine interaction in the ground state of the negatively charged nitrogen vacancy center in diamond. *Phys. Rev. B*, 79:075203, Feb 2009. 58, 85

[94] Xing-Fei He, Neil B. Manson, and Peter T. H. Fisk. Paramagnetic resonance of photoexcited n- V defects in diamond. ii. hyperfine interaction with the ^{14}N nucleus. *Phys. Rev. B*, 47:8816–8822, Apr 1993. 58

[95] R. Hanson, O. Gywat, and D. D. Awschalom. Room-temperature manipulation and decoherence of a single spin in diamond. *Phys. Rev. B*, 74:161203, Oct 2006. 58

[96] Susumu Takahashi, Ronald Hanson, Johan van Tol, Mark S. Sherwin, and David D. Awschalom. Quenching spin decoherence in diamond through spin bath polarization. *Phys. Rev. Lett.*, 101:047601, Jul 2008. 58

[97] I. Siddiqi, R. Vijay, M. Metcalfe, E. Boaknin, L. Frunzio, R. J. Schoelkopf, and M. H. Devoret. Dispersive measurements of superconducting qubit coherence with a fast latching readout. *Phys. Rev. B*, 73:054510, Feb 2006. 60, 87

[98] Francois Mallet, Florian R. Ong, Agustin Palacios-Laloy, Francois Nguyen, Patrice Bertet, Denis Vion, and Daniel Esteve. Single-shot qubit readout in circuit quantum electrodynamics. *Nat Phys*, 5(11):791–795, November 2009. 60, 87

[99] V. M. Acosta, E. Bauch, M. P. Ledbetter, C. Santori, K.-M. C. Fu, P. E. Barclay, R. G. Beausoleil, H. Linget, J. F. Roch, F. Treussart, S. Chemerisov, W. Gawlik, and D. Budker. Diamonds with a high density of nitrogen-vacancy centers for magnetometry applications. *Phys. Rev. B*, 80:115202, Sep 2009. 65

[100] Alexander I. Lvovsky, Barry C. Sanders, and Wolfgang Tittel. Optical quantum memory. *Nat Photon*, 3(12):706–714, December 2009. 76

[101] A. Lund, M. Shiotani, and S. Shimada. *Principles and Applications of ESR Spectroscopy*. Springer, 2011. 76

[102] H. Malissa, D. I. Schuster, A. M. Tyryshkin, A. A. Houck, and S. A. Lyon. Superconducting coplanar waveguide resonators for low temperature pulsed electron spin resonance spectroscopy, 2012. 77

[103] Claude Cohen-Tannoudji, Franck Laloe, and Bernard Diu. *Mecanique quantique. Tome 1.* Hermann [Paris], 1973. 84

[104] A. Dréau, J.-R. Maze, M. Lesik, J.-F. Roch, and V. Jacques. High-resolution spectroscopy of single nv defects coupled with nearby ^{13}c nuclear spins in diamond. *Phys. Rev. B*, 85:134107, Apr 2012. 84

[105] Benjamin Smeltzer, Lilian Childress, and Adam Gali. 13 c hyperfine interactions in the nitrogen-vacancy centre in diamond. *New Journal of Physics*, 13(2):025021, 2011. 85, 86

[106] F. Jelezko, T. Gaebel, I. Popa, M. Domhan, A. Gruber, and J. Wrachtrup. Observation of coherent oscillation of a single nuclear spin and realization of a two-qubit conditional quantum gate. *Phys. Rev. Lett.*, 93:130501, Sep 2004. 85

[107] Andrew M. Steane. How to build a 300 bit, 1 giga-operation quantum computer. *Quantum Information & Computation*, 7(3):171–183, 2007. 87

[108] E. Knill. Quantum computing with realistically noisy devices. *Nature*, 434(7029):39–44, March 2005. 87

[109] Erik Lucero, M. Hofheinz, M. Ansmann, Radoslaw C. Bialczak, N. Katz, Matthew Neeley, A. D. O'Connell, H. Wang, A. N. Cleland, and John M. Martinis. High-fidelity gates in a single josephson qubit. *Phys. Rev. Lett.*, 100:247001, Jun 2008. 87

[110] A. Wallraff, D. I. Schuster, A. Blais, L. Frunzio, J. Majer, M. H. Devoret, S. M. Girvin, and R. J. Schoelkopf. Approaching unit visibility for control of a superconducting qubit with dispersive readout. *Phys. Rev. Lett.*, 95:060501, Aug 2005. 88

[111] Maxime Boissonneault, J. M. Gambetta, and Alexandre Blais. Dispersive regime of circuit qed: Photon-dependent qubit dephasing and relaxation rates. *Phys. Rev. A*, 79:013819, Jan 2009. 88

[112] N. Bergeal, F. Schackert, M. Metcalfe, R. Vijay, V. E. Manucharyan, L. Frunzio, D. E. Prober, R. J. Schoelkopf, S. M. Girvin, and M. H. Devoret. Phase-preserving amplification near the quantum limit with a josephson ring modulator. *Nature*, 465(7294):64–68, May 2010. 88, 98

[113] N. Roch, E. Flurin, F. Nguyen, P. Morfin, P. Campagne-Ibarcq, M. H. Devoret, and B. Huard. Widely tunable, nondegenerate three-wave mixing microwave device operating near the quantum limit. *Phys. Rev. Lett.*, 108:147701, Apr 2012. 88, 98

[114] J. E. Johnson, C. Macklin, D. H. Slichter, R. Vijay, E. B. Weingarten, John Clarke, and I. Siddiqi. Heralded state preparation in a superconducting qubit, 2012. 88, 98, 99, 100

[115] D. Ristè, J. G. van Leeuwen, H. S. Ku, K. W. Lehnert, and L. DiCarlo. Initialization by measurement of a two-qubit superconducting circuit, 2012. 88, 97

[116] F. Lecocq, J. Claudon, O. Buisson, and P. Milman. Nonlinear coupling between the two oscillation modes of a dc squid. *Phys. Rev. Lett.*, 107:197002, Nov 2011. 90, 91

[117] J. Claudon, F. Balestro, F. W. J. Hekking, and O. Buisson. Coherent oscillations in a superconducting multilevel quantum system. *Phys. Rev. Lett.*, 93:187003, Oct 2004. 90

[118] S. K. Dutta, Frederick W. Strauch, R. M. Lewis, Kaushik Mitra, Hanhee Paik, T. A. Palomaki, Eite Tiesinga, J. R. Anderson, Alex J. Dragt, C. J. Lobb, and F. C. Wellstood. Multilevel effects in the rabi oscillations of a josephson phase qubit. *Phys. Rev. B*, 78:104510, Sep 2008. 90

[119] E. Hoskinson, F. Lecocq, N. Didier, A. Fay, F. W. J. Hekking, W. Guichard, O. Buisson, R. Dolata, B. Mackrodt, and A. B. Zorin. Quantum dynamics in a camelback potential of a dc squid. *Phys. Rev. Lett.*, 102:097004, Mar 2009. 90

[120] F. Lecocq, I. M. Pop, I. Matei, E. Dumur, A. K. Feofanov, C. Naud, W. Guichard, and O. Buisson. Coherent frequency conversion in a superconducting artificial atom with two internal degrees of freedom. *Phys. Rev. Lett.*, 108:107001, Mar 2012. 90, 91

[121] Alexia Auffèves-Garnier, Christoph Simon, Jean-Michel Gérard, and Jean-Philippe Poizat. Giant optical nonlinearity induced by a single two-level system interacting with a cavity in the purcell regime. *Phys. Rev. A*, 75:053823, May 2007. 95, 97

[122] R. Vijay, D. H. Slichter, and I. Siddiqi. Observation of quantum jumps in a superconducting artificial atom. *Phys. Rev. Lett.*, 106:110502, Mar 2011. 97

[123] Roy J. Glauber. Coherent and incoherent states of the radiation field. *Phys. Rev.*, 131:2766–2788, Sep 1963. 98

[124] Leonard Mandel and Emil Wolf. *Optical Coherence and Quantum Optics*. Cambridge University Press, 1995. 98

[125] R. Vijay, C. Macklin, D. H. Slichter, S. J. Weber, K. W. Murch, R. Naik, A. N. Korotkov, and I. Siddiqi. Quantum feedback control of a superconducting qubit: Persistent rabi oscillations, 2012. 100

[126] Mr. Bayes. An essay towards solving a problem in the doctrine of chances. *Phil. Trans. R. Soc. Lond.*, 53:370–418, 1763. 100

[127] H. Chernoff. A measure of asymptotic efficiency for tests of a hypothesis based on the sum of observations. *The Annals of Mathematical Statistics*, 23(4):493–507, 1952. 101

[128] X. Zhou, I. Dotsenko, B. Peaudecerf, T. Rybarczyk, C. Sayrin, S. Gleyzes, J. M. Raimond, M. Brune, and S. Haroche. Field locked to a fock state by quantum feedback with single photon corrections. *Phys. Rev. Lett.*, 108:243602, Jun 2012. 103